

## REVIEW

View Article Online  
View Journal | View IssueCite this: *Mater. Chem. Front.*,  
2024, 8, 732

# Recent advances in polyoxometalate-based materials and their derivatives for electrocatalysis and energy storage

Yao Zhang,<sup>a</sup> Yanyan Li,<sup>b</sup> Haoran Guo,<sup>b</sup> Yunqiao Guo<sup>b</sup> and Rui Song<sup>a,b</sup>

The development and implementation of sustainable clean energy have attracted more attention in response to the urgent requirements of environmental pollution and the energy crisis caused by fossil fuels. Consequently, there is a pressing demand for the advancement and implementation of diverse energy conversion and storage technologies to facilitate the generation and utilization of clean energy sources. With the characteristics of reversible redox properties, high thermodynamic and chemical stability, controllable size, and precise structure, polyoxometalates (POMs) have broad application prospects in electrocatalysis and energy storage. Herein, the significant roles of POMs in electrocatalysis and energy storage have been highlighted. Then, the recent advances of POM-based materials and their derivatives in water-splitting, CO<sub>2</sub> reduction reactions (CO<sub>2</sub>RR), the N<sub>2</sub> reduction reaction (NRR), supercapacitors (SCs), and rechargeable batteries are systematically summarized. Furthermore, this review discusses the relationship between the catalyst structure and catalytic reaction activity by comparing different electrocatalytic or energy storage systems. Finally, the conclusions and outlooks of POM-based materials and their derivatives in electrocatalysis and energy storage are discussed to promote new progress.

Received 11th September 2023,  
Accepted 6th November 2023

DOI: 10.1039/d3qm01000g

rsc.li/frontiers-materials

## 1. Introduction

The excessive consumption of fossil fuels has led to a series of problems such as environmental pollution, climate change, and the global energy crisis, making the exploration of environmentally renewable green energy and the development of clean new energy the main goals of the energy strategy.<sup>1</sup> While renewable energy sources such as solar, wind, nuclear, and hydrogen have been extensively explored, their geographical limitations and intermittent nature pose significant obstacles to their application and sustainable development.<sup>2,3</sup> If these intermittent renewable energy sources could be converted and stored, this would greatly facilitate their widespread use and enable sustainable energy utilization.

Within this context, researchers have proposed a strategy to achieve sustainable energy utilization through the mutual conversion of electrical energy and chemical energy. Electrical energy can be converted into chemical energy through energy conversion technologies, such as water-splitting to hydrogen,<sup>4</sup> CO<sub>2</sub> reduction reactions (CO<sub>2</sub>RRs) to chemical fuels,<sup>5</sup> N<sub>2</sub>

reduction reactions (NRR) to ammonia fuel,<sup>6</sup> and so on. However, energy storage systems can realize energy conversion from stored chemical energy to electrical energy, such as supercapacitors (SCs),<sup>7</sup> lithium-ion batteries (LIBs),<sup>8</sup> metal-air batteries,<sup>9</sup> other rechargeable batteries,<sup>10</sup> *etc.* In both energy conversion technologies and energy storage systems, a reliable means to improve the efficiency of energy conversion is to develop high-activity and low-cost electrocatalysts or electrode materials that reduce the energy barrier.<sup>11</sup>

Polyoxometalates (POMs) are a type of metal-oxygen cluster compound, which contain abundant metal sources (Mo, W, V, *etc.*).<sup>12</sup> The basic building unit of POMs is MO<sub>x</sub> ( $x = 4, 5, 6$ ), in which M is commonly a high-valent transition metal element such as W, Mo, V, Nb, Ta, *etc.*<sup>13</sup> These transition metal elements can be substituted by metal ions from almost all regions of the periodic table, including the d-, f-, ds-, and p-block. Additionally, the central atoms in POM anions can be substituted by various heteroatoms, including a wide range of metal and non-metal elements, such as Si, P, B, Ge, S, Se, Ga, *etc.* Therefore, the elemental composition, skeleton structure, valence state, and atomic number of POMs can be fine-tuned and designed,<sup>14</sup> which can be ideal candidates for non-precious metal-based electrocatalysts and electrode materials.

Recently, researchers have reviewed the prospects of POM-based materials and their derivatives in electrocatalytic and energy storage applications. Lan *et al.*<sup>15</sup> summarized advances

<sup>a</sup> School of Materials and Chemical Engineering, Xuzhou University of Technology, Xuzhou 221018, P. R. China<sup>b</sup> School of Chemical Sciences, University of Chinese Academy of Sciences, 19 Yuquan Road, Shijingshan District, Beijing, 100049, P. R. China.  
E-mail: rsong@ucas.ac.cn

in POM-based materials for water-splitting, CO<sub>2</sub> reduction, rechargeable batteries, supercapacitors, and dye-sensitized solar cells. Afterward, Lan *et al.*<sup>16</sup> outlined the progress of POM-based photo/electrocatalysts for application in the HER, OER, and CO<sub>2</sub>RR. Wei *et al.*<sup>17</sup> summarized a comprehensive overview of POM-contained and POM-derived electrocatalysts for the HER. Song *et al.*<sup>18</sup> reviewed the synthesis, structure modulation, and HER/OER performance of POM/MOF composites and their derivatives. Li *et al.*<sup>19</sup> reviewed POM-based electrocatalysts for electrocatalytic CO<sub>2</sub>RRs and highlighted the advantages of POMs in CO<sub>2</sub>RRs. Zang *et al.*<sup>20</sup> summarized POM-based catalysts in electro/photocatalytic CO<sub>2</sub>RRs and focused on the relationship between the structure and catalytic activity. Liu and Streb<sup>21</sup> highlighted the application of POM-SAC in energy-relevant applications, including water-splitting, CO<sub>x</sub>, and N<sub>2</sub> activation. Song *et al.*<sup>22</sup> discussed the prepared methods of POM/nanocarbon composite materials and applied them as electrocatalysts or electrodes for LIBs, SCs, and sensors. Pang *et al.*<sup>23</sup> highlighted progress on POM-based materials in fuel cells, Li- and Na-ion batteries, and redox flow batteries. Han *et al.*<sup>24</sup> summarized recent research on POM derivatives for various rechargeable batteries. Zhao *et al.*<sup>25</sup> reviewed the advances of POM composite and POM-based composite materials in the fields of electrochemical detection, electrocatalysis, and energy. Dubal *et al.*<sup>26</sup> provided a review of POM-generated materials for applications in energy devices (SCs, batteries, *etc.*) and energy catalysts. Fabre *et al.*<sup>27</sup> reviewed the application of POM-functionalized (photo)electrodes in the HER, OER, and CO<sub>2</sub>RR since the mid-2010s. It should be pointed out that POM-based materials have only been discussed in terms of electrocatalytic or energy storage. Some articles provide a comprehensive overview of POM-based materials, but a detailed overview has not received special attention in the above review. In recent years, POM-based materials and their derivatives have made significant advances in innovative preparation methods and applications. Therefore, it is essential to summarize the recent progress of POMs and their derivatives in electrocatalysis and energy storage.

In this review, the recent research progress on POM-based materials and their derivatives in electrocatalysis and energy storage applications are provided. The focus is primarily on the application of POMs in various electrocatalytic processes such as water splitting, the CO<sub>2</sub>RR, the NRR, and energy storage including SCs and rechargeable batteries. The advantages of POMs in factors affecting catalytic performance are discussed. Finally, the challenges and outlooks of POM-based materials in electrocatalysis and energy storage are briefly discussed, and we look forward to the development of efficient and controllable POM-based electrocatalytic and electrode materials.

## 2. Advantages of POMs in electrocatalytic and energy-related devices

In 1826, Berzelius' research group first discovered hetero-polyacid compound (NH<sub>4</sub>)<sub>3</sub>[PMo<sub>12</sub>O<sub>40</sub>]·*n*H<sub>2</sub>O.<sup>28</sup> However, the structure of

POMs could not be determined for a long time, leading to stagnation in the development of POM chemistry. It was not until 1934 that Keggin determined the crystallographic structure of H<sub>3</sub>[PW<sub>12</sub>O<sub>40</sub>]·29H<sub>2</sub>O using X-ray diffraction methods.<sup>29</sup> With the advancement of instrument technology, especially single-crystal X-ray crystallography, researchers have discovered hundreds of new POM structures.

POMs have excellent physical and chemical properties including solubility, thermal/chemical stability, acidity, reversible redox ability, high negative charges, electron/proton storage, transport capacities, *etc.*<sup>16,30</sup> Most importantly, these corresponding properties can be tuned by changing the structural dimensions, composition elements, and organic bridging components.<sup>16</sup> Thus, the unique properties of POMs lead them to be used in applications of catalysis,<sup>31,32</sup> energy,<sup>15,33</sup> material,<sup>34–36</sup> sensors,<sup>37,38</sup> electronic,<sup>39</sup> biomedicine,<sup>40</sup> radionuclide capture,<sup>41</sup> and so on. In addition, significant progress in the innovation of synthesis methods on POM-based materials and POM-derived materials has been achieved, such as an ion-exchanged method,<sup>31</sup> oxidative polymerization method,<sup>42</sup> supramolecule-confinement pyrolysis (SCP) strategy,<sup>43</sup> soft-template approach,<sup>44</sup> direct solid reaction,<sup>45</sup> encapsulation strategy,<sup>46</sup> sol-gel method,<sup>47</sup> magnesiothermic reduction approach,<sup>48</sup> electrochemical etching technology,<sup>49</sup> charge-directed self-assembly method,<sup>50</sup> solid-phase hot-pressing method,<sup>51</sup> inkjet printing technology,<sup>52</sup> interfacial engineering strategy,<sup>53</sup> single-molecule confinement strategy,<sup>54</sup> and so on.

### 2.1. Advantages of POM molecules in electrocatalytic and energy-related devices

The main characteristics of POMs are as follows (Scheme 1): (i) clear composition and diverse structures. The composition and structure of POMs are clear, which is helpful to identify the



Scheme 1 The main characteristics of POMs.



catalytic active sites and reveal the reaction mechanism.<sup>55</sup> A single POM molecule can contain 6 to 368 metal ions, and most elements from the periodic table can be assembled into polyoxoanion frameworks. More than 70 different elements can serve as heteroatoms, including many electrocatalytic active elements, which are conducive to regulating the electrocatalytic performance of POM-based electrocatalysts.<sup>56</sup> (ii) Adjustable molecular volume. The molecular volume of POMs ranges from a few nanometers to over ten nanometers, which is beneficial for combining POMs with other porous materials, such as MOFs, COFs, *etc.* The construction of POMOFs improves the stability of POMs in electrocatalytic and energy-related devices. Meanwhile, POMOFs can combine the advantages of POMs and MOFs, which is a promising platform for constructing electrode materials with high capacitance activity and multifunctional ion channels. (iii) Reversible redox properties. POMs can maintain high structural stability while rapidly gaining or losing electrons, which is conducive to improving the efficiency of multi-electron catalytic reactions.<sup>57,58</sup> (iv) Adjustable valence state. The same polyoxoanion can exist in both oxidized and reduced states, and undergo color changes during electron gain or loss, which is favorable to energy storage devices like lithium-ion batteries and pseudocapacitors where energy storage and release are based on chemical redox reactions.<sup>23,59</sup> (v) The modifiability of the active site. POMs can be applied as flexible scaffolds to assemble POM-based materials through host-guest, hydrogen bonding, electrostatic interaction, or organic modification. Thus, the active sites of POM materials can be regulated according to the characteristics of electrocatalytic and energy-related devices.<sup>16</sup> (vi) Easy derivatization. POMs have oxygen-rich surfaces that are easily activated and modified to construct organic-inorganic hybrid and organic derivative materials, making POMs a promising precursor for the development of non-noble metal-based electrocatalytic materials, supercapacitors, and rechargeable battery electrode materials. The infinite molecular structures of POMs give them unparalleled physical and chemical properties, which have been extensively explored for their potential applications in catalysis, water electrolysis for hydrogen production, the CO<sub>2</sub>RR, NRR, supercapacitors, rechargeable batteries, and other fields.

## 2.2. Advantages of POMs as precursors for preparing electrocatalysts

The synthesis of electrocatalysts using POMs molecules as precursors has the following advantages: (i) the composition of POMs contains a variety of electrocatalytic active metal elements (such as Mo, W, V, *etc.*), which can be used as a metal source to improve the redox properties of electrode materials;<sup>17,60</sup> (ii) heteroatoms in POMs can be doped as heterogeneous elements to improve catalytic performance;<sup>61</sup> (iii) POMs have a clear composition and crystal structure, which are easily regulated at the molecular or atomic level.<sup>62</sup>

## 3. The research process of POMs for electrocatalytic applications

### 3.1. Water splitting

As a “zero-carbon” green energy carrier, hydrogen energy has the advantages of high energy density, clean and pollution-free, which is considered to be one of the most promising energy sources to replace traditional fossil energy.<sup>63–65</sup> Electrolyzed water hydrogen production technology with the characteristics of being clean and efficient has become the most promising large-scale hydrogen production method.<sup>66</sup> Water splitting includes two half-reactions, *i.e.*, the cathodic hydrogen evolution reaction (HER) and anodic oxygen evolution reaction (OER).<sup>67</sup> At present, the high performance of HER and OER catalysts are commercial Pt/C and IrO<sub>2</sub>/RuO<sub>2</sub>, respectively, but their large-scale application is severely limited due to their low earth abundance, high cost, and poor stability.<sup>68</sup> While the efficiency of non-noble metal-based electrocatalysts is lower, which leads to the high cost of hydrogen production from electrolytic water. Therefore, the core task of developing water electrolysis technology is to develop efficient and low-cost electrocatalysts.

**3.1.1. POM-based materials for water splitting.** In the past few decades, POM molecular materials have attracted much attention as electrocatalysts for water splitting. Due to the superior redox ability of POMs, one or multiple electrons can be reversibly provided or accepted during the electrochemical process.<sup>69</sup> Besides, POMs have many advantages as catalysts for

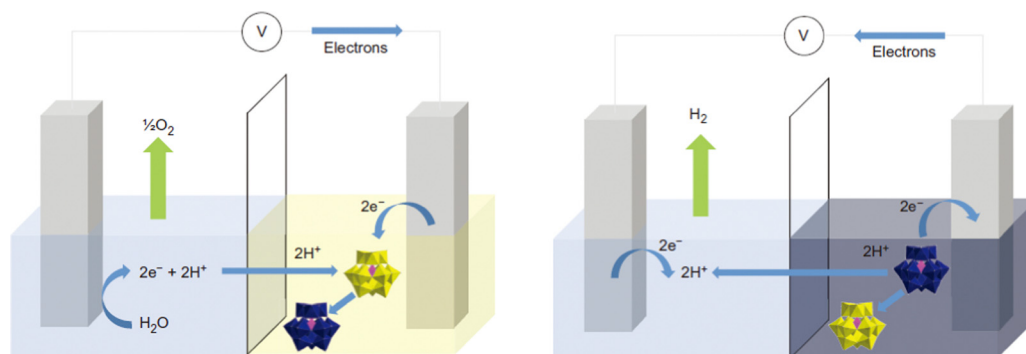


Fig. 1 Schematic of the ECPB-based approach to water splitting.<sup>71</sup> Copyright 2013, Springer Nature.





electrocatalysis, as shown in Section 2.1. Thus, POM-based materials are ideal candidates for non-noble metal-based HERs and OERs or bifunctional electrocatalysts.

**POM-based HER electrocatalysts.** Keita *et al.*<sup>70</sup> studied the HER activity of POM-modified electrodes in acidic electrolytes by using different POM molecular catalysts ( $[\text{H}_7\text{P}_8\text{W}_{48}\text{O}_{184}]^{33-}$ ,  $[\text{Co}_6(\text{H}_2\text{O})_{30}\{\text{Co}_9\text{Cl}_2(\text{OH})_3(\text{H}_2\text{O})_9(\beta\text{-SiW}_8\text{O}_{31})_3\}]^{5-}$  and  $[\{\text{Co}_3(\text{B}\beta\text{-SiW}_9\text{O}_{33}(\text{OH}))(\text{B}\beta\text{-SiW}_8\text{O}_{29}\text{OH})_2\}]^{22-}$ ). The storage behavior of POMs on protons and electrons can affect the microenvironment of POM-modified electrodes, which significantly affects its HER performance. Afterward, the Cronin group<sup>71</sup> made a significant breakthrough in the POM-based water electrolysis system. It can be observed from Fig. 1 that a water separation system was developed using the electron-coupled proton buffer (ECPB) concept. During the process of water oxidation, phosphomolybdic acid ( $\text{H}_3\text{PMo}_{12}\text{O}_{40}$ ) in this system acts as a redox mediator to absorb electrons and protons generated, which results in the production of  $\text{H}_2$  and  $\text{O}_2$  occurring in distinct times and spaces. This method effectively avoids the problems of traditional water electrolysis processes, such as product mixing and electrolytic cell degradation. Under the action of the reduction mediator silicotungstic acid ( $\text{H}_4[\text{SiW}_{12}\text{O}_{40}]$ ), the pure hydrogen produced by the platinum catalytic system at the equivalent platinum loading is more than 30 times faster than that of the proton exchange membrane electrolyzer.

Although reduced POMs have been proven to be good HER electrocatalysts, their catalytic performance will be limited due to their small specific surface area and poor conductivity.<sup>72</sup> To increase the specific surface area and conductivity of POMs,

researchers have combined POMs with larger specific surface area materials including metal-organic framework (MOFs),<sup>73</sup> graphene,<sup>74</sup> carbon nanotubes (CNTs),<sup>75</sup> covalent organic frameworks (COFs),<sup>76</sup> *etc.* Nohra *et al.*<sup>77</sup> first reported a POM-based MOF compound (POMOF) for the HER (Fig. 2a) with a turnover frequency (TOF) of  $6.7 \text{ s}^{-1}$  at an overpotential of 200 mV. Lan's group<sup>78</sup> synthesized NENU-500 and NENU-501, which showed excellent HER performance in acidic electrolytes, as plotted in Fig. 2b. Liu *et al.*<sup>79</sup> prepared a new type of  $\text{P}_8\text{W}_{48}/\text{rGO}$  nanocomposites by anchoring POM  $[\text{H}_7\text{P}_8\text{W}_{48}\text{O}_{184}]^{33-}$  ( $\text{P}_8\text{W}_{48}$ ) on the 3D structure of reduced graphene oxide (rGO) nanosheets using an electroreduction method (Fig. 2c), which showed excellent HER performance and nearly 100% Faraday efficiency (FE) under acidic conditions. Kortz's group<sup>80</sup> prepared nanocomposites of POMs ( $\text{P}_2\text{W}_{18}$ ,  $\text{P}_5\text{W}_{30}$ , and  $\text{P}_8\text{W}_{48}$ ) and rGO through one-step electroreduction synthesis, and studied the relationship between POMs size, shape, composition, charge, and HER activity. Wei's group<sup>81</sup> co-deposited Cu and Anderson-type POM ( $\text{NiMo}_6\text{O}_{24}$ ) on  $\text{TiO}_2$  arrays to prepare  $\text{NiMo}_6\text{O}_{24}@\text{Cu}/\text{TNA}$ , and investigated its structure and valence state. It was proven that the POM can regulate and modify the surface morphology of Cu dendrites. In acidic HER,  $\text{NiMo}_6\text{O}_{24}$  as a Brønsted acid, can improve  $\text{H}^+$  transfer, further adsorb H atoms, make up for the weak H atom adsorption capacity of Cu dendrites, and accelerate the HER rate by combining the strong electron transfer effect of POM molecules.

**POM-based OER electrocatalysts.** POM-based OER electrocatalysts also face the problem of poor stability and conductivity of POMs. Thus, the preparation of high-efficient and stable

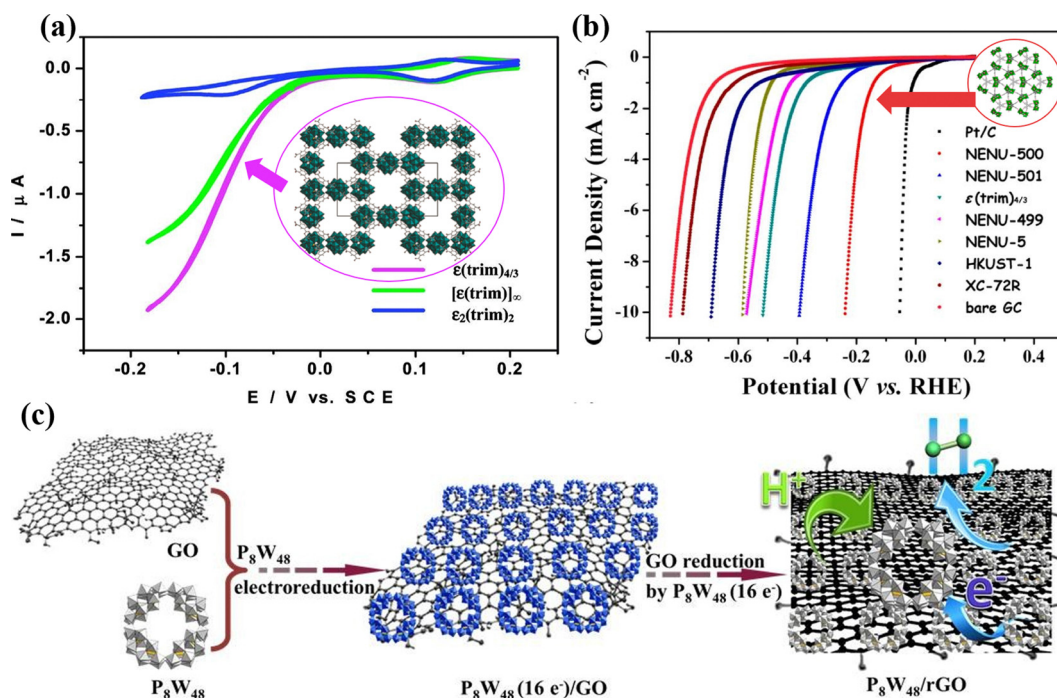


Fig. 2 (a) Comparison of the HER activity of  $\epsilon(\text{trim})_{4/3}$ ,  $\epsilon_2(\text{trim})_2$ , and  $[\epsilon(\text{trim})]_{\infty}$ .<sup>77</sup> Copyright 2011, American Chemical Society (ACS). (b) Comparison of the HER activity of the NENU-500, NENU-501, and other POMOF catalysts.<sup>78</sup> Copyright 2015, American Chemical Society (ACS). (c) Scheme of the synthesis of the  $\text{P}_8\text{W}_{48}/\text{rGO}$  nanocomposite.<sup>79</sup> Copyright 2016, Royal Society of Chemistry (RSC).





OER electrocatalysts by combining POMs with conductive substrates (such as graphene, CNT, nickel foam, conductive polymers, *etc.*) has been widely studied.<sup>82,83</sup> The effective electron transfer between POMs and conductive substrates is crucial for the OER process of multi-electron transfer. POMs modified by highly redox-active metals (Ru and Co) are the most promising catalysts for OER electrocatalysis.<sup>84</sup>

Howells *et al.*<sup>85</sup> reported the first POM molecular electrocatalyst  $\text{Na}_{14}[\text{Ru}^{\text{III}}_2\text{Zn}_2(\text{H}_2\text{O})_2(\text{ZnW}_9\text{O}_{34})_2]$  for the OER. Toma *et al.*<sup>86</sup> assembled Ru-containing POM clusters ( $\text{Ru}_4\text{POM}:\text{M}_{10}[\text{Ru}_4(\text{H}_2\text{O})_4(\mu\text{-O})_4(\mu\text{-OH})_2(\gamma\text{-SiW}_{10}\text{O}_{36})_2]$ ,  $\text{M} = \text{Cs}, \text{Li}$ ) and multi-walled carbon nanotubes (MWCNT) into an efficient and stable OER catalyst (POM/MWCNT). As shown in Fig. 3a, the interaction between the MWCNT carrier and POMs increased the specific surface area and accelerated the electron transfer rate to the electrode, which is beneficial for the improvement of OER performance. Song's group<sup>87</sup> deposited POM ( $[\text{Co}_{6.8}\text{Ni}_{1.2}\text{W}_{12}\text{O}_{42}(\text{OH})_4(\text{H}_2\text{O})_8]$ ) molecular catalyst microcrystalline on the nickel foam electrode to prepare a NiCo-POM/Ni electrode (Fig. 3b), which has high OER performance and near 100% FE. The NiCo-POM/Ni electrode can work for a long time under alkaline conditions, and the crystal structure of POM remains unchanged (Fig. 3b). Blasco-Ahicart *et al.*<sup>88</sup> reported two water-insoluble cobalt-based POM catalysts:

$\text{Ba}[\text{Co-POM}]/\text{CP}$  ( $\text{Ba}_8[\text{Co}_9(\text{H}_2\text{O})_6(\text{OH})_3(\text{HPO}_4)_2(\text{PW}_9\text{O}_{34})_3]\cdot 55\text{H}_2\text{O}$ ) and  $\text{Cs}[\text{Co-POM}]/\text{CP}$  ( $\text{Cs}_{15}\text{K}[\text{Co}_9(\text{H}_2\text{O})_6(\text{OH})_3(\text{HPO}_4)_2(\text{PW}_9\text{O}_{34})_3]\cdot 28\text{H}_2\text{O}$ ), which have better OER performance and good stability (Fig. 3c), indicating that this type of non-noble metal POMs is expected to replace precious metal catalysts. Cronin's group<sup>89</sup> synthesized  $\text{Co}_4\text{Mo}_x\text{W}_y$  with a sandwich structure *via* Mo-doped into  $[\text{Co}_4(\text{H}_2\text{O})_2(\text{PW}_9\text{O}_{34})_2]^{10-}$  ( $\text{Co}_4\text{W}_{18}$ ). As illustrated in Fig. 3c, water can be oxidized at a lower initial potential by adjusting the amount of Mo doping in POMs and controlling the doping sites of Mo.

*POM-based HER and OER bifunctional electrocatalysts.* Wei's group<sup>90</sup> anchored POM molecules ( $\text{PW}_{12}$ ) on NF-based zinc-cobalt sulfide nanowires to prepare a bifunctional self-supporting electrode (POM@ZnCoS/NF), which displayed high HER and OER activity (Fig. 4a and b). The anchored POM nanoparticles increased the number of electrochemically active sites and electrochemically active surface area. Their work showed that the incorporation of POMs has obvious advantages in the design of bifunctional catalysts with low cost and high performance. In addition, Talib *et al.*<sup>91</sup> investigated the effect of single transition metal ( $\text{M}_1$ ) loaded on phosphomolybdic acid (PMA) clusters on the HER and OER electrocatalytic performance by density functional theory (DFT) calculation.

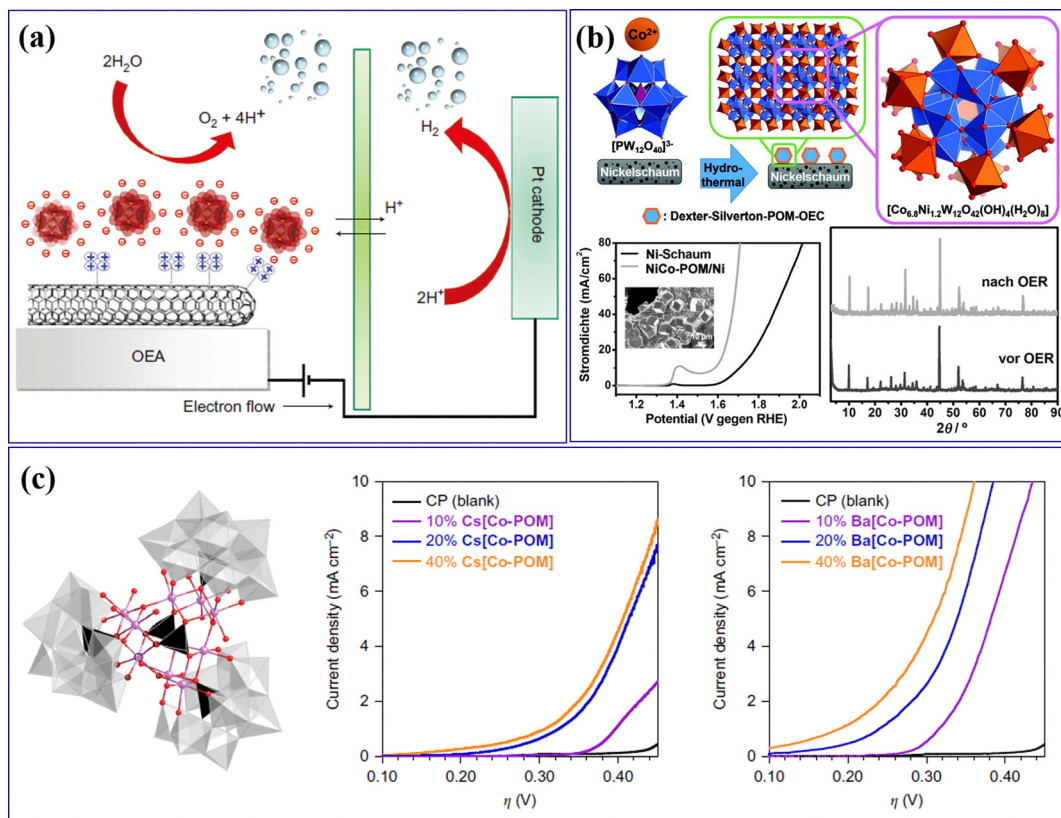


Fig. 3 (a) Scheme for a water-splitting electrocatalytic cell with the integrated nanostructured oxygen-evolving anode of POM/MWCNT.<sup>86</sup> Copyright 2010, Macmillan Publishers. (b) Deposition of Dexter-Silverton polyoxometalate microcrystals on nickel foam electrodes with their OER activity.<sup>87</sup> Copyright 2017, Wiley-VCH. (c) Molecular structure of the Co-POM cluster and electrochemical behavior of Co-POM/CP electrodes.<sup>88</sup> Copyright 2017, Springer Nature.



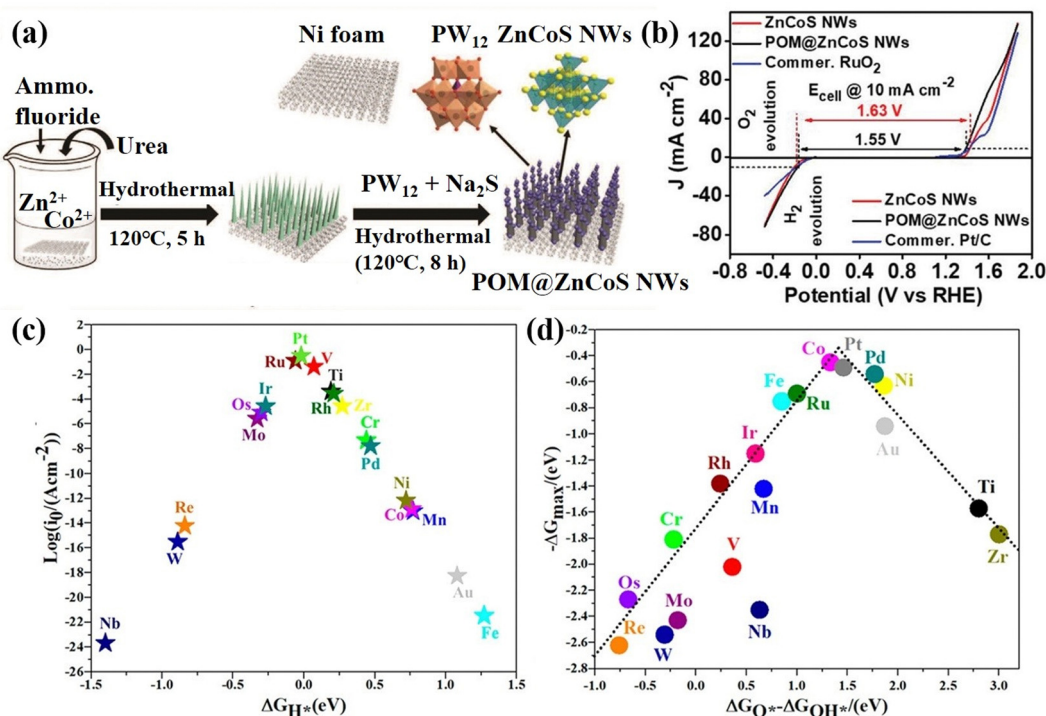


Fig. 4 (a) The synthesis diagram of POM@ZnCoS NWs. (b) Half-cell LSV curves for the OER and HER of the as-prepared electrodes at a scan rate 10 mV s<sup>-1</sup>.<sup>90</sup> Copyright 2021, Wiley-VCH. (c) HER volcano plot and (d) OER volcano plot of the M<sub>1</sub>/PMA cluster.<sup>91</sup> Copyright 2021, American Chemical Society (ACS).

The volcano diagram calculation showed that V<sub>1</sub>/PMA, Ti<sub>1</sub>/PMA, Ru<sub>1</sub>/PMA, and Pt<sub>1</sub>/PMA catalysts have good HER performance (Fig. 4c), while Co<sub>1</sub>/PMA and Pt<sub>1</sub>/PMA can be used as highly active OER catalysts (Fig. 4d). This study showed that PMA clusters are a promising single-atom support for the HER and OER, providing high-efficiency electrocatalytic activity and low cost.

**3.1.2. POM-derived materials for water splitting.** Although POMs molecular catalysts have made some progress in the field of HER and OER, the application of POMs electrocatalysis is still limited by the solubility and poor stability of POMs in the reaction medium.<sup>16</sup> In recent years, the preparation of POM-derived materials *via* thermal conversion technology using POM molecules as precursors has attracted wide attention. Pyrolysis of POMs (such as carbonization, nitridation and phosphating) in an inert atmosphere is an effective method to enhance the activity and stability of POM-based electrocatalysts.<sup>15</sup> Heteroatom-doped and carbon-coated composites can be prepared *via* annealing the mixture of heteroatom-doped POMs and carbon sources. During the pyrolysis treatment process, the carbon source is converted into a graphitized carbon layer wrapped on the surface of the catalyst, which can improve the surface area and conductivity of the catalyst. Carbon-coating can protect the metal species from corrosion in a harsh electrolyte environment.<sup>92</sup> Additionally, doping heteroatoms (such as N, P, S, *etc.*) can adjust the surface properties of the carbon layer and increase the electron density of the carbon layer.<sup>93</sup> Zou's group<sup>94</sup> used soluble small-sized

POMs (ammonium molybdate) as the Mo source and dicyandiamide (DCA) as the small-molecule organic carbon source. After mixing and calcining them under an Ar atmosphere, ultra-small molybdenum carbide nanoparticles (Mo<sub>2</sub>C@NC) with N-doped and C-coated were prepared. The nanoparticles have high HER activity in all-pH electrolytes. Similarly, Li's group prepared nano-sized HER electrocatalysts P-W<sub>2</sub>C@NC,<sup>95</sup> MoP/Mo<sub>2</sub>C@C,<sup>96</sup> CoMoP@C,<sup>97</sup> TM-Mo<sub>2</sub>C@C,<sup>98</sup> and Co<sub>2</sub>P/WC@NC<sup>99</sup> by mixing Mo-based or W-based POMs with DCA and carbonization, as well as preparing POM-derived HER electrocatalysts by pyrolysis of POMs with other carbon materials, such as MoC<sub>x</sub>@C,<sup>100</sup> Ni/WC@NC,<sup>101</sup> P-Mo<sub>2</sub>C@NC,<sup>102</sup> and MoPS/NC.<sup>103</sup>

In addition, Lan's group used phosphomolybdic acid and phosphotungstic acid as POM sources assembling with polypyrrole (PPy) and rGO into nanocomposites, namely PMo<sub>12</sub>-PPy/rGO and PW<sub>12</sub>-PPy/rGO. Then, further calcined PMo<sub>12</sub>-PPy/rGO and PW<sub>12</sub>-PPy/rGO under a N<sub>2</sub> atmosphere to synthesize N, P co-doped and C-coated carbide catalysts: Mo<sub>2</sub>C@NPC/NPRGO<sup>104</sup> (Fig. 5a) and NC@W<sub>x</sub>C/NRGO<sup>105</sup> (Fig. 5c). It can be seen from Fig. 5b and d that both of these materials exhibit a HER performance comparable to 20% Pt/C. Wei's group<sup>106</sup> designed and synthesized the N-doped molybdenum phosphide and molybdenum carbide composite catalyst N@MoPC<sub>x</sub> using benzene imine-derivatized POMs (Mo<sub>4</sub>O(ARPO<sub>3</sub>)<sub>2</sub>(NAR)<sub>4</sub>(μ<sub>2</sub>-NAR)<sub>5</sub>, Ar = phenyl, Mo<sub>4</sub>-CNP) as the precursor under the high-temperature pyrolysis in inert gas (Fig. 5e). Benzenimine and phenyl phosphonic acid ligands as N, C, and P sources can be doped, carbonized and phosphatized at the same time.



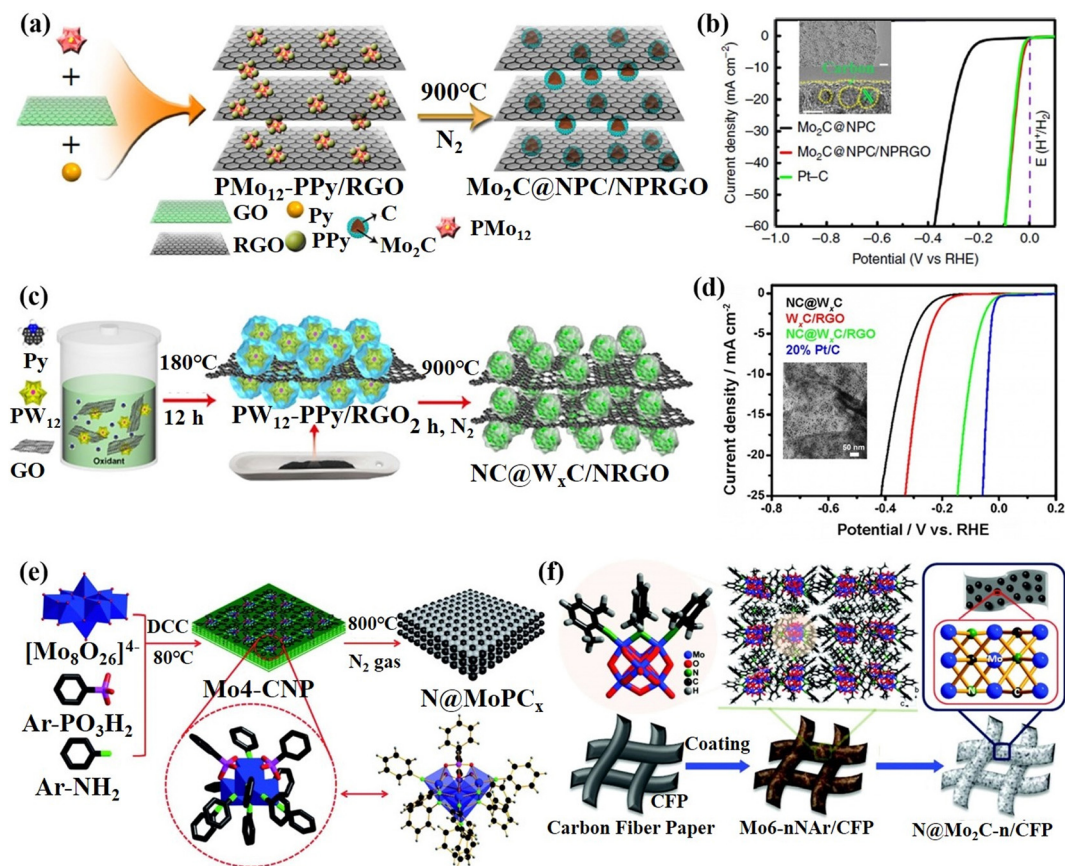


Fig. 5 (a) The synthetic process and (b) HER activity of  $\text{Mo}_2\text{C}@NPC/NPRGO$ .<sup>104</sup> Copyright 2016, Nature. (c) The preparation process and (d) HER activity of  $\text{NC}@W_x\text{C}/\text{NRGO}$ .<sup>105</sup> Copyright 2017, Wiley-VCH. (e) The synthetic procedure for the preparation of  $\text{N}@MoPC_x$ .<sup>106</sup> Copyright 2017, Wiley-VCH. (f) A schematic illustration of the synthesis of  $\text{N}@Mo_2\text{C}-n/\text{CFP}$ .<sup>107</sup> Copyright 2017, Wiley-VCH.

The organic ligand can *in situ* generate substrate carbon during the pyrolysis process, which was beneficial to enhance the conductivity and stability of the catalyst. The composite material exhibits excellent HER activity and stability. Afterward, the N-implanted  $\text{Mo}_2\text{C}$  ( $\text{N}@Mo_2\text{C}-n/\text{CFP}$ ) was prepared by pyrolysis organoimido-derivatized POM that can directly adjust the amounts of N atoms in  $\text{N}@Mo_2\text{C}-n/\text{CFP}$ <sup>107</sup> (Fig. 5f). This design of the molecular structure of POMs to achieve *in situ* doping is another effective method for preparing high-efficiency POM-based composite catalysts. Wang's group<sup>108</sup> through a high-temperature calcination process synthesized the  $\text{Co}/\text{WC}@NC$  electrocatalyst using bimetallic POMs ( $[\text{Co}_9(\text{OH})_3(\text{H}_2\text{O})_6(\text{HPO}_4)_2(\text{PW}_9\text{O}_{34})_3]^{16-}$ ) as soft templates and polyethyleneimine (PEI) as a carbon source. The  $\text{Co}/\text{WC}@NC$  displayed high HER activity and stability in both acidic and alkaline electrolytes mainly attributed to the synergistic effect of Co nanoparticles with WC, and the protective effect of the graphitized carbon layer.

Furthermore, POM-derived catalysts can also be prepared by pyrolysis of POM precursors in a reducing atmosphere. Fu's group<sup>109</sup> prepared a P-doped  $\text{WN}/\text{rGO}$  composite catalyst by further phosphating the composite of phosphotungstic acid and graphene after annealing in an  $\text{NH}_3$  atmosphere (Fig. 6a and b). Owing to the P doping and the interaction between rGO and WN, the catalyst has high HER performance, as plotted in

Fig. 6c and d. In addition, Tan's group<sup>110</sup> adopted a molecular-to-cluster strategy to calcine the mixture of POM molecules ( $[\{\text{Co}_4(\text{OH})_3\text{PO}_{4/4}(\text{SiW}_9\text{O}_{34})\}_4]^{32-}$ ,  $[\{\text{Fe}_2\text{Co}_2(\text{OH})_3\text{PO}_{4/4}(\text{SiW}_9\text{O}_{34})\}_4]^{24-}$ , and  $[\{\text{FeCo}_3(\text{OH})_3\text{PO}_{4/4}(\text{SiW}_9\text{O}_{34})\}_4]^{28-}$ ) and EDA-C60 under a  $\text{H}_2/\text{Ar}$  atmosphere to prepare ultra-small transition metal clusters (TMC: 1-CoW, 2-CoFeW, and 3-CoFeW) with controllable chemical composition (Fig. 6e–g). The catalytic performance of TMC was fine-tuned by surface doping, which can solve the adsorption performance of the reaction intermediate on the surface of the transition metal clusters (Fig. 6h). As shown in Fig. 6i, the prepared 3-CoFeW exhibited high OER performance and stability in alkaline media.

Although the above methods can effectively improve the activity of POM-derived electrocatalysts, there still exist some problems. For example, POM molecules, especially transition metal-substituted POMs molecules, tend to form multiphase mixed structures after annealing treatment, which may lead to unclear active sites. In addition, high-temperature pyrolysis treatment requires large energy consumption, which is contrary to the concept of green sustainability. At present, the preparation of POM-derived materials using a mild hydrothermal synthesis method can take advantage of the solubility of most POMs and meanwhile can save energy. In addition, researchers have further improved the performance of POM-derived materials through various regulation methods, such as a surface





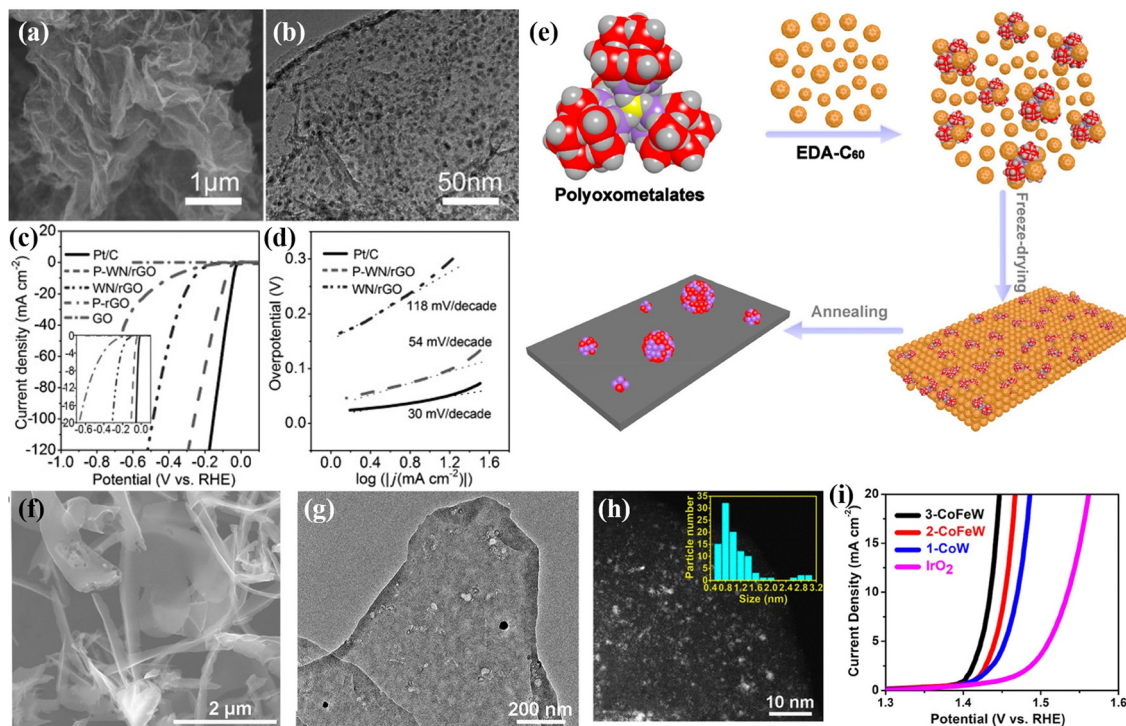


Fig. 6 (a) SEM image and (b) TEM image of P-WN/rGO; (c) LSV curves and (d) Tafel plots for the as-prepared electrodes.<sup>109</sup> Copyright 2015, Wiley-VCH. (e) Schematic illustration of synthesizing the TMCs; (f) SEM image, (g) TEM image, and (h) HAADF-STEM image of 1-CoW; (i) OER curves of catalysts loaded on carbon cloth.<sup>110</sup> Copyright 2018, American Chemical Society (ACS).

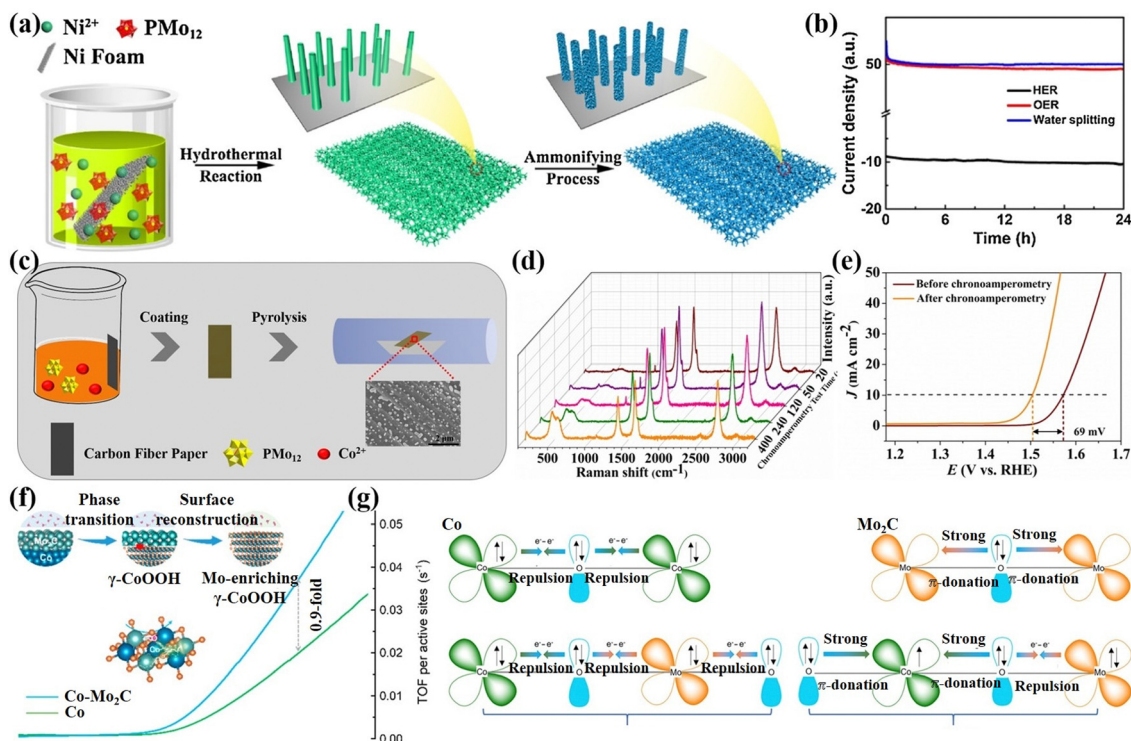


Fig. 7 (a) The synthetic process of P-NiMo<sub>4</sub>N<sub>5</sub>@Ni composite. (b) Chronoamperometric curves of P-NiMo<sub>4</sub>N<sub>5</sub>@Ni-1 for the HER, OER, and water splitting.<sup>112</sup> Copyright 2018, Elsevier B.V. (c) The synthetic process of CoMo<sub>4</sub>O<sub>4</sub>@CP ( $x = 0.3, 1$  or  $3$ ). (d) *In situ* Raman spectra with the increase of the chronoamperometry test time. (e) LSV measured before and after chronoamperometry test.<sup>49</sup> Copyright 2019, Elsevier B.V. (f) The process of phase transition of Co-Mo<sub>2</sub>C to Mo-enriching  $\gamma$ -CoOOH. (g) Schematic representation of the electronic coupling between Co and Mo in the post-OER products of Co, Mo<sub>2</sub>C, and Co-Mo<sub>2</sub>C heterostructure.<sup>113</sup> Copyright 2020, American Chemical Society (ACS).



reconstruction strategy, interface engineering strategy, defect construction strategy, and atom doping strategy, single-atom catalysts (SACs) strategy, etc.

**Surface reconstruction strategy.** During the alkaline electrocatalytic process, the oxides, sulfides, nitrides, and phosphides of the later transition metal (Fe, Co, Ni, etc.) are prone to surface reconstruction, and the corresponding hydroxides or hydroxyl oxides are derived and participate in the catalytic reaction as true active species.<sup>111</sup> While the existence of high valence states former transition metals (Mo, W, etc.) can accelerate the occurrence of surface reconstruction. Hence, exploring the surface reconstruction of electrocatalysts has important significance for understanding the structure–activity relationship of catalysts and developing high-performance catalysts. Lan's group<sup>112</sup> reported a P-NiMo<sub>4</sub>N<sub>5</sub>@Ni self-supporting electrode with controllable morphology through hydrothermal and phosphating treatment (Fig. 7a). It is worth noting that PMo<sub>12</sub> with water solubility and acidity can moderately dissolve a small amount of Ni on the NF surface, which was conducive to the uniform growth of a nano-array structure on NF.

Meanwhile, heteroatom P in PMo<sub>12</sub> was introduced into the electrode material. After the OER stability test, the surface of the P-NiMo<sub>4</sub>N<sub>5</sub>@Ni electrode oxidized to OER active species such as metal hydroxides or hydroxyl oxides. As displayed in Fig. 7b, the P-NiMo<sub>4</sub>N<sub>5</sub>@Ni showed high HER, OER, and water-splitting performance. Zhang *et al.*<sup>49</sup> prepared a CoMo<sub>x</sub>O<sub>4</sub>@CP self-supporting electrode by depositing PMo<sub>12</sub> and Co salt on carbon paper (CP). During the electrochemical activation process (Fig. 7c), the electrode surface undergoes continuous structural evolution due to the etching effect of MoO<sub>4</sub><sup>2-</sup>, resulting in a significant increase in OER activity (Fig. 7a and e). Kou *et al.*<sup>113</sup> synthesized a Co–Mo<sub>2</sub>C material as an OER pre-catalyst by anion exchange reaction of Co in Co-MOF with MoO<sub>4</sub><sup>2-</sup> in POMs. During the OER process, the metal Co phase rapidly reconstructed into  $\gamma$ -CoOOH enriched with Mo, which significantly improved the catalytic activity (Fig. 7f). Through various *in situ* characterization analyses, the process of electron interaction was summarized as shown in Fig. 7g.

**Interface engineering strategy.** Interface engineering has important significance for improving the performance of heterostructure

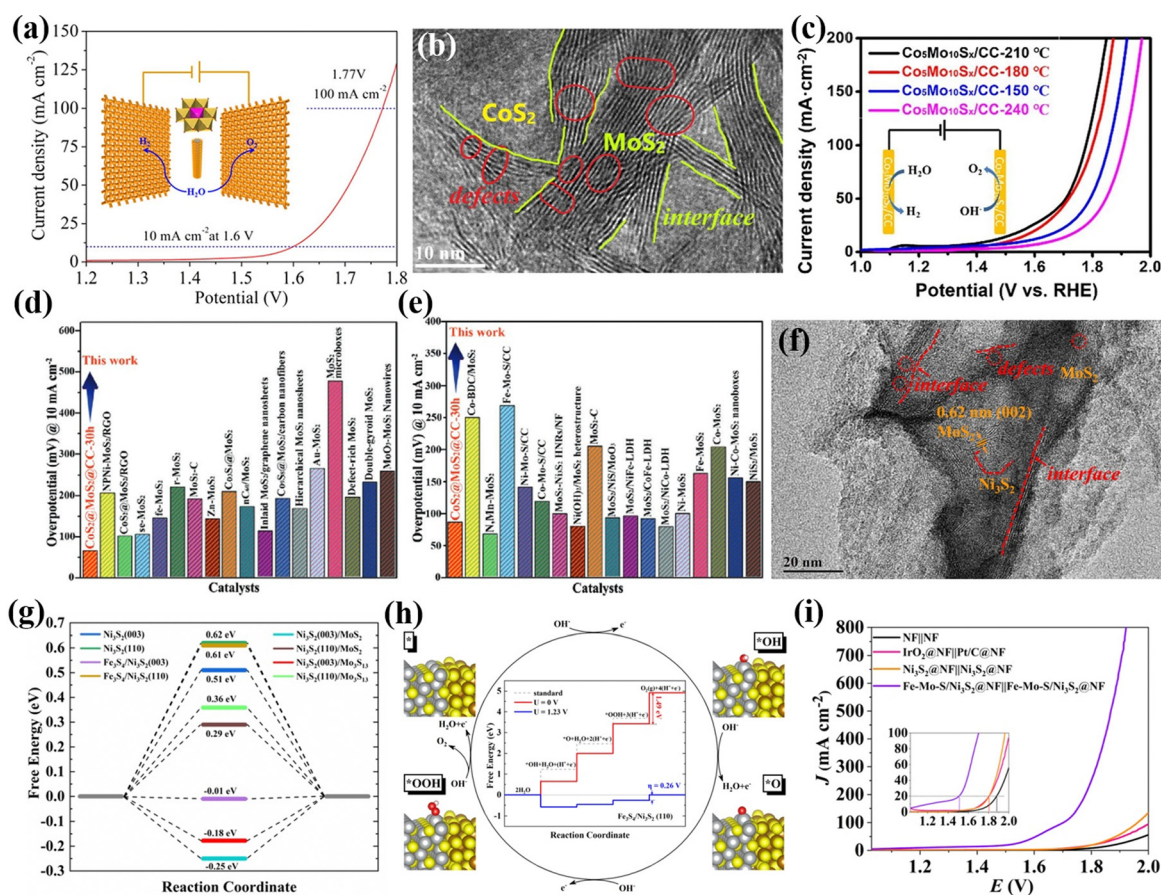


**Fig. 8** (a) Overall water splitting performance through the use of O–CoMoS array as a perspective anode and cathode.<sup>121</sup> Copyright 2018, American Chemical Society (ACS). (b) HRTEM images of Co<sub>5</sub>Mo<sub>10</sub>S<sub>x</sub>@CC. (c) Overall water-splitting performance of Co<sub>5</sub>Mo<sub>10</sub>S<sub>x</sub>@CC.<sup>122</sup> Copyright 2020, Elsevier B.V. A comparison of overpotentials in CoS<sub>2</sub>@MoS<sub>2</sub>@CC-30 h and the reported MoS<sub>2</sub>-based electrocatalysts at 10 mA cm<sup>-2</sup> in (d) 0.5 M H<sub>2</sub>SO<sub>4</sub> and (e) 1.0 M KOH electrolyte.<sup>123</sup> Copyright 2020, Wiley-VCH. (f) HRTEM images with different magnifications of Fe–Mo–S/NiS<sub>2</sub>@NF. (g) HER free energy changes on reaction surfaces. (h) Free energy diagrams for the OER process at the Fe<sub>3</sub>S<sub>4</sub>/Ni<sub>3</sub>S<sub>2</sub>(110) interface. (i) Overall water-splitting performance of Fe–Mo–S/Ni<sub>3</sub>S<sub>2</sub>@NF.<sup>53</sup> Copyright 2020, Elsevier B.V.





electrocatalysts, especially for electrocatalytic reactions involving various reaction intermediates such as the alkaline HER and OER.<sup>114</sup> Heterostructure electrocatalysts with rich interfaces exhibit obvious kinetic acceleration behavior for alkaline HER or OER owing to the synergistic effect of different components, then balance the adsorption or desorption behavior of intermediates at the interface.<sup>115,116</sup> Interface engineering can effectively adjust the electronic structure of active sites by means of electronic interaction,<sup>117</sup> interface bonding,<sup>118</sup> and lattice strain,<sup>119</sup> thus optimizing the binding energy of target intermediates. Furthermore, the confinement effect of the composite interface to maintain the high density of active sites of the catalyst is essential for improving stability.<sup>120</sup>

Heteropolyoxometalates are composed of fixed-proportion heteroatoms and coordination atoms. Thus, applying POMs as precursors is beneficial to the construction of multi-interface catalysts. Sun's group<sup>121</sup> successively prepared bimetallic sulfide and carbon cloth composite electrocatalysts (oxygenated-CoS<sub>2</sub>-MoS<sub>2</sub>) using the hydrothermal method to sulfurize

Anderson-type POMs ((NH<sub>4</sub>)<sub>4</sub>[Co<sup>II</sup>Mo<sub>6</sub>O<sub>24</sub>H<sub>6</sub>]-6H<sub>2</sub>O). Owing to the exposure of active heterointerfaces, and the facilitated charge transport, the overall water-splitting performance of oxygenated-CoS<sub>2</sub>-MoS<sub>2</sub> arrays delivered 10 mA cm<sup>-2</sup> at 1.6 V (Fig. 8a). Lu *et al.*<sup>122</sup> constructed multiple interface-regulated CoS<sub>2</sub>-MoS<sub>2</sub> heterojunction catalysts (Co<sub>2</sub>Mo<sub>10</sub>S<sub>x</sub>/CC) at the atomic level using Evans-Showell-type POM (Co<sub>3</sub>[Co<sub>2</sub>Mo<sub>10</sub>O<sub>38</sub>H<sub>4</sub>]) as a molecular pre-assembly platform using a hydrothermal method. Due to the electronic interaction between the active component CoS<sub>2</sub> and MoS<sub>2</sub>, the active center reconstructed into the CoMoS site through the interface effect (Fig. 8b). Compared with the single synthesized Co<sub>2</sub>Mo<sub>10</sub>S<sub>x</sub>/CC, the Co<sub>2</sub>Mo<sub>10</sub>S<sub>x</sub>/CC electrode derived from POMs showed higher over water-splitting activity (Fig. 8c). Experiments combined with theoretical calculations showed that its excellent electrocatalytic activity was attributed to the improved intrinsic catalytic activity of CoMoS sites, the synergistic effect of heterostructures, and the heterogeneous interface with defect-rich sites. Hou *et al.*<sup>123</sup> used a POM-based functional material

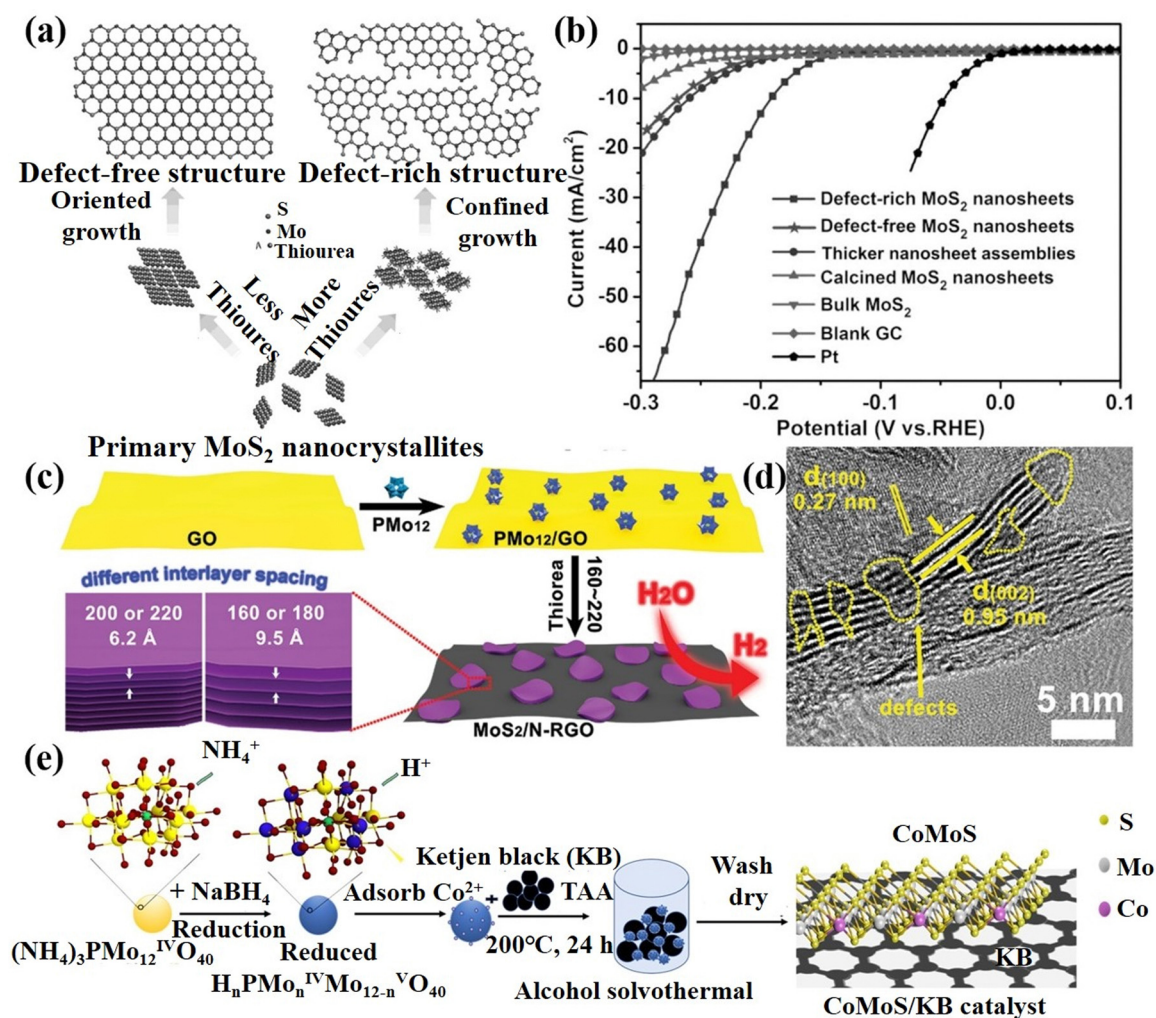


Fig. 9 (a) Structural models and synthetic path diagrams of defect-free and defect-rich structures; (b) LSV curves of various samples as indicated.<sup>126</sup> Copyright 2013, Wiley-VCH. (c) The schematic preparation process of MoS<sub>2</sub>/N-RGO-T nanocomposite; (d) HRTEM of MoS<sub>2</sub>/N-RGO-180.<sup>127</sup> Copyright 2016, Wiley-VCH. (e) Schematic illustration of the synthesis of the CoMoS/KB catalyst.<sup>128</sup> Copyright 2021, American Chemical Society (ACS).





$(((1,2,4\text{-triazole})_3\text{Co}_2\cdot 6\text{H}_2\text{O})[\text{H}_3\text{GeMo}_{12}\text{O}_{40}]\cdot 9\text{H}_2\text{O})$  as a bimetallic precursor for hydrothermal sulfidation, and finally generated a  $\text{CoS}_2@\text{MoS}_2$  nanoarray catalyst with a multiple interface structure. Due to the high crystallinity of POMs and the fixed-proportion of bimetallic sources, the synthesized  $\text{CoS}_2@\text{MoS}_2@\text{CC-30 h}$  electrode material displayed high electrocatalytic HER activity in a wide pH range (Fig. 8d and e). Based on the advantages of POMs and multi-interface component catalysts, Zhang *et al.*<sup>53</sup> used an Anderson-type POM  $(\text{NH}_4)_4[\text{FeMo}_6\text{O}_{24}\text{H}_6]\cdot 6\text{H}_2\text{O}$  ( $\text{FeMo}_6$ ) as a bimetallic precursor to prepare the  $\text{Fe-Mo-S/Ni}_3\text{S}_2@\text{NF}$  electrode with a multi-interface using a one-step hydrothermal method (Fig. 8f). DFT calculations showed that HER activity was mainly provided by the  $\text{Fe}_3\text{S}_4/\text{Ni}_3\text{S}_2(003)$  and  $\text{Ni}_3\text{S}_2(003)/\text{Mo}_3\text{S}_{13}$  interfaces (Fig. 8g), while the  $\text{Fe}_3\text{S}_4/\text{Ni}_3\text{S}_2(110)$  interface provided a high OER performance (Fig. 8h). Thereby, the  $\text{Fe-Mo-S/Ni}_3\text{S}_2@\text{NF}$  electrode showed high HER, OER, and overall water-splitting performance, as shown in Fig. 8i.

**Defect construction strategy.** Defects can affect the electronic structure, surface and interface properties, thereby changing the original distribution to adjust the adsorption energy of the intermediate.<sup>124</sup> In addition, some defects can act as electrocatalytic active sites, such as vacancies, unsaturated coordination sites, and lattice defects to enhance the catalytic activity of the materials.<sup>125</sup> Thus, the reasonable construction of defects is helpful to adjust and optimize the electrocatalytic performance of POM-based materials. Xie's group<sup>126</sup> synthesized  $\text{MoS}_2$  ultrathin nanosheets with defect-rich structures by using ammonium molybdate as a Mo source with excessive thiourea under hydrothermal conditions (Fig. 9a). The  $\text{MoS}_2$  nanosheets with a rich defect structure could expose more edge active sites, which exhibited excellent HER performance, as plotted in Fig. 9b. Lan's group<sup>127</sup> combined  $\text{PMo}_{12}$  that has good water solubility and strong redox properties with GO to prepare  $\text{MoS}_2/\text{N-RGO}$

composite with defects after the sulfurization process (Fig. 9c and d). Due to electrostatic repulsion,  $\text{PMo}_{12}$  particles can be uniformly dispersed between GO layers. Meanwhile, GO can be reduced to RGO owing to the strong reducibility of  $\text{PMo}_{12}$ . The  $\text{MoS}_2/\text{N-RGO}$  composite displayed excellent HER performance under acidic conditions. Tang *et al.*<sup>128</sup> *in situ* prepared a defective  $\text{CoMoS}/\text{KB}$  nanocluster catalyst (Fig. 9e) by using small and uniform sizes of reduced POMs  $(\text{NH}_4)_3\text{PMo}_{12}\text{O}_{40}$  as the template and anchor sites of metal salts, which was beneficial to expose more edge active sites. Therefore, the  $\text{CoMoS}/\text{KB}$  catalyst has excellent activity and stability for the HER. In summary, the construction of surface defects provides a solution to further improve the catalytic activity.

**Doping control strategy.** Heteroatom doping can evidently increase the intrinsic conductivity of the catalyst, regulate the electronic structure, and optimize the adsorption and desorption of intermediates on the catalyst surface, which play a key role in improving the electrocatalytic performance.<sup>129</sup> Heteroatom doping can be roughly divided into non-metal atom doping (such as N, P, S, O, *etc.*) and metal atom doping (such as Fe, Co, Ni, Zn, *etc.*). Among them, non-metallic atom doping can enhance the electronic structure at the catalytic active sites to effectively adjust the work function and increase the adsorption of the reactants at a specific position, thereby improving their electrocatalytic activity.<sup>130</sup> Metal doping can accelerate the electron transfer in different sites through the synergistic effect between metal atoms and other atoms, then reduce the energy barrier of the reaction intermediate.<sup>131</sup>

Heteropolyoxometalates have inherent heteroatoms, which can provide various doped heteroatoms (such as P, W, Mo, Ni, Co, Fe, *etc.*) for the final electrocatalyst. These heteroatoms can enhance the electrochemical performance through empty orbitals or lone pair electrons.<sup>132</sup> Cronin's group<sup>89</sup> synthesized

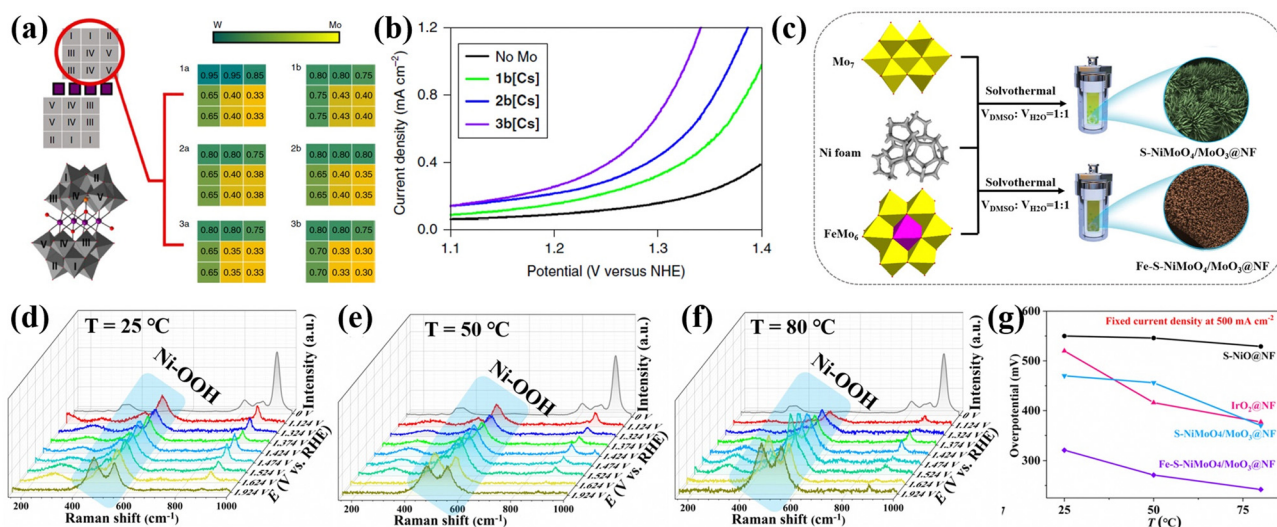


Fig. 10 (a) Crystallographic data for the six compounds of  $\text{Co}_4\text{Mo}_4\text{W}_y$ ; (b) water oxidation activity of 1b[Cs]–3b[Cs] compounds.<sup>89</sup> Copyright 2018, Springer Nature. (c) Schematic map of the synthesis of  $\text{Fe-S-NiMoO}_4/\text{MoO}_3@\text{NF}$ ; *In situ* Raman spectra of  $\text{Fe-S-NiMoO}_4/\text{MoO}_3@\text{NF}$  during the OER process at different electrolysis temperatures: (d) 25 °C, (e) 50 °C, and (f) 80 °C; (g) Comparison of the requirement overpotential of the prepared electrodes at 25–80 °C at  $500 \text{ mA cm}^{-2}$ .<sup>61</sup> Copyright 2021, Elsevier B.V.



$\text{Co}_4\text{Mo}_x\text{W}_y$ , containing a Mo and W mixed sandwich structure through doping Mo into  $\text{Co}_4\text{W}_{18}$ , as shown in Fig. 10a. Adjusting the amount of Mo doping in POMs could control the doping sites of Mo, which oxidized water at a lower onset potential without degradation of the catalyst. The OER overpotential of 3b[Cs] was 188 mV lower than that of the pure tungsten skeleton (Fig. 10b). Their work provided a strategy for preparing molecular heterogeneous catalysts by using Mo-doped POM clusters to improve water oxidation performance, and also opens up new ideas for the development of POM-based electrolyzed water catalysts *via* similar design principles. Zhang *et al.*<sup>61</sup> synthesized a Fe-S-NiMoO<sub>4</sub>/MoO<sub>3</sub>@NF self-supporting electrode using FeMo<sub>6</sub> as a precursor through a one-step solvothermal method, as illustrated in Fig. 10c. The FeMo<sub>6</sub> precursor could accurately control the doping ratio of Fe in Fe-S-NiMoO<sub>4</sub>/MoO<sub>3</sub>@NF. The *in situ* Raman experiments (Fig. 10d-f) on the optimal Fe-S-NiMoO<sub>4</sub>/MoO<sub>3</sub>@NF sample in the electrolyte

temperature range of 25–80 °C showed that the improvement of OER activity was due to the formation of more OER active phases, and finally achieved a quasi-industrial OER performance (Fig. 10g).

In addition to single-atom doping, multi-atom doping is also an effective way to enhance catalytic performance. Wei's group<sup>133</sup> prepared 1T-MoS<sub>2</sub> co-doped with different TMs and O atoms, namely NiO@1T-MoS<sub>2</sub>, CoO@1T-MoS<sub>2</sub>, and FeO@1T-MoS<sub>2</sub> using Anderson-type POMs that contain different heteroatoms as precursors for electrochemical HERs, as shown in Fig. 11a. It can be observed from the HAADF-STEM image in Fig. 11b that NiO@1T-MoS<sub>2</sub> showed a hexagonal intensity change, which was consistent with the single-layer of 1T-MoS<sub>2</sub> reported by Eda, G. *et al.*<sup>134</sup> While the strength of Ni centers and Mo atoms in all regions of the sample have changed (Fig. 11c), indicating that the hexagonal units of NiMo<sub>6</sub> were well retained in the final NiO@1T-MoS<sub>2</sub> nanosheets, which avoided the

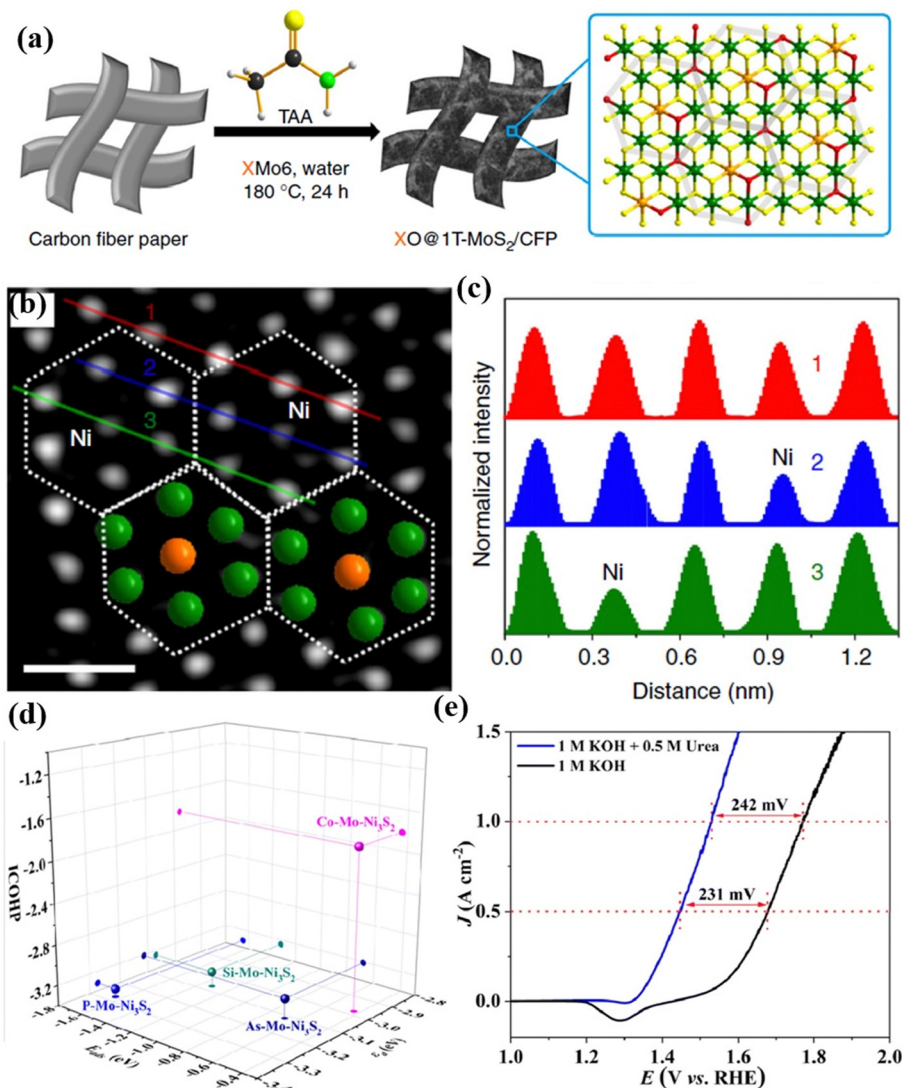


Fig. 11 (a) The preparation process of XO@1T-MoS<sub>2</sub>/CFP; (b) aberration-corrected atomic resolution HAADF-STEM image (scale bar: 0.5 nm); (c) intensity profiles along the lines indicated in (b).<sup>133</sup> Copyright 2019, Springer Nature. (d) A comparison of  $E_{\text{ads}}(\text{urea})$ ,  $\epsilon_{\text{d}}$ , and ICOHP values. (e) A comparison of the UOR and OER activity of P-Mo-Ni<sub>3</sub>S<sub>2</sub>@NF.<sup>135</sup> Copyright 2023, Royal Society of Chemistry (RSC).



agglomeration problem that may be caused by direct doping of metal atoms. Experimental and theoretical studies have shown that Ni and O atoms were simultaneously doped into ultrathin 1T-MoS<sub>2</sub> nanosheets, which could effectively regulate the electronic structure, and also provided more catalytic active sites, reducing the energy barrier required for hydrolysis. Zhang *et al.*<sup>135</sup> prepared P and Mo co-doped Ni<sub>3</sub>S<sub>2</sub> (P-Mo-Ni<sub>3</sub>S<sub>2</sub>@NF) using PMo<sub>12</sub> as the dopants through a theory-guided strategy (Fig. 11d). As presented in Fig. 11e, the P-Mo-Ni<sub>3</sub>S<sub>2</sub>@NF electrode showed a decent performance of urea assisted electrolytic water.

**Single-atom catalyst (SAC) strategy.** A single-atom catalyst can be used to stabilize a single independent atom on the carrier, which has the advantage of clear active sites of homogeneous catalysts and recyclable heterogeneous catalysts.<sup>136</sup> POMs are ideal molecular systems for exploring SAC anchoring,<sup>21</sup> which can greatly help to avoid the agglomeration of metal parts during the synthesis process.<sup>17</sup> Li's group<sup>137</sup> used POMs (PtW<sub>6</sub>, PtMo<sub>6</sub>, PtV<sub>9</sub> and PtSiW<sub>11</sub>) as Pt-based SAC models, and the prepared {PtW<sub>6</sub>}/C has excellent electrocatalytic HER activity. This work clearly explains the structure-activity relationship of the electrocatalytic HER of SAC Pt for the first-time using

POMs as a model. Specifically, the catalytic activity of Pt SACs electrocatalysts is affected by both the metal-oxide support and the coordination environment of Pt single atom active sites (Fig. 12a). The coordination environments of Pt single atoms were similar in the models of {PtW<sub>6</sub>}, {PtMo<sub>6</sub>} and {PtV<sub>9</sub>}, and the electron acquisition of the Pt single atom was affected due to the different electron affinity of the metal-oxide support carrier, which led to the different effective potential and catalytic activity of the Pt center. Whereas in the POM molecular models of {PtSiW<sub>11</sub>} and {PtW<sub>6</sub>}, the Pt single atoms exhibited similar metal-oxide supports, the different coordination environment of single atom Pt in the two POM models resulted in different catalytic reaction pathways, thus affecting the final HER activity (Fig. 12b). Zhang's group<sup>138</sup> fabricated Pt<sub>1</sub>-Mo<sub>2</sub>C-C catalyst derived Pt-POMs (Fig. 12c), which exhibited high activity and stability in the HER. Talib *et al.*<sup>139</sup> investigated the HER, OER, and ORR performance of M<sub>1</sub>/PW<sub>12</sub>O<sub>40</sub> single-atom electrocatalysts *via* DFT calculation. The above studies demonstrated that POM-based SACs display the advantages of performance improvement in electrocatalysis. The following points can be summarised. (i) Due to the high stability and electron-rich properties of POM clusters, the POM-based SACs can effectively adjust the electronic properties

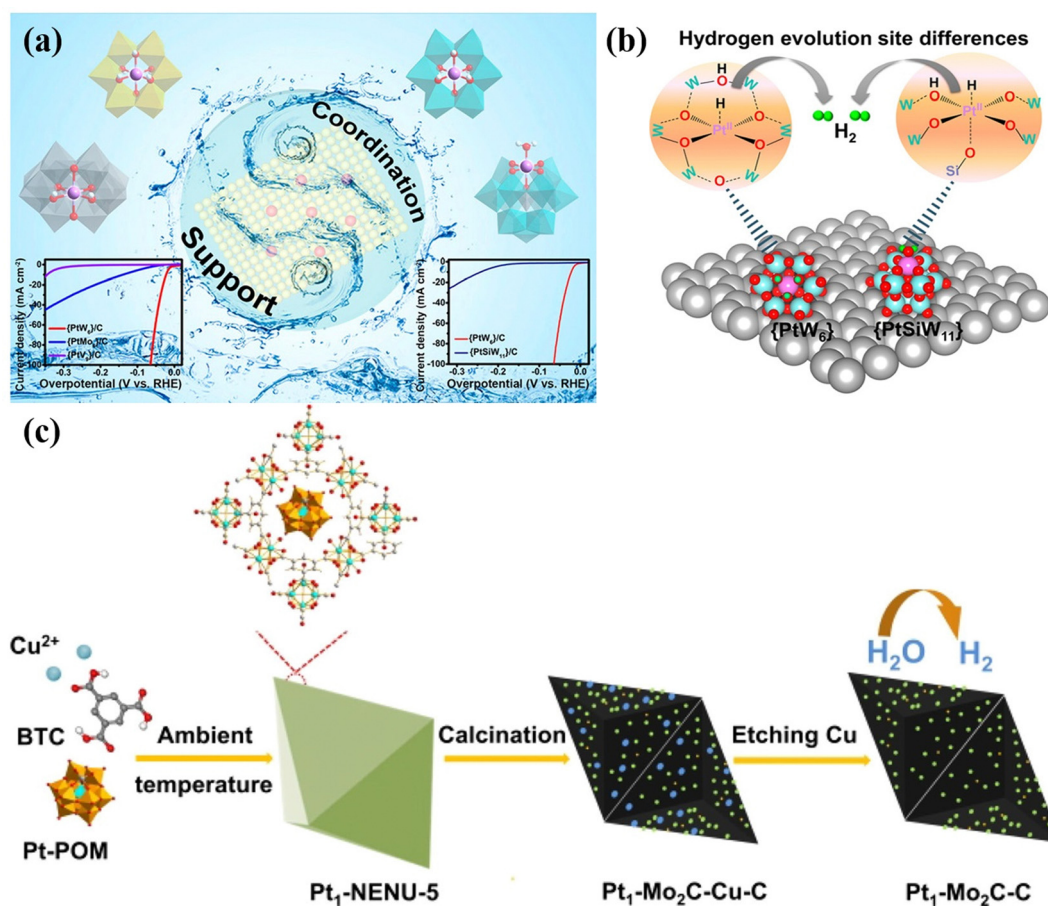


Fig. 12 (a) Schematic illustration of Pt-based SAC models and HER performance. (b) Different hydrogen evolution sites responsible for the {PtW<sub>6</sub>} and {PtSiW<sub>11</sub>}.<sup>137</sup> Copyright 2021, American Chemical Society (ACS). (c) Schematic illustration of the formation of Pt<sub>1</sub>-Mo<sub>2</sub>C-C.<sup>138</sup> Copyright 2021, ELSEVIER B.V.





of SAC active sites, promote electron transfer between SAC active sites and existing support, which can be the key factor in improving the catalytic efficiency. (ii) The overall catalytic activity of the POM-based SACs can be attributed to the synergy between all the metal sites in the framework. (iii) The interaction between SACs sites and POM clusters is usually stabilized by coordination bonds or covalent coordination bonds, which will prevent the aggregation and leaching of SAC active sites in the catalytic reaction process, thus enhancing the stability. The HER and OER performances of the POM-based materials and POM-derived materials in this review are shown in Table 1 and Table 2, respectively.

### 3.2 CO<sub>2</sub> reduction reaction

Recently, the excessive consumption of fossil fuels has led to a large release of CO<sub>2</sub> into the atmosphere, exacerbating the greenhouse effect and disrupting the natural carbon balance.<sup>140</sup> In this context, there is an urgent demand to explore effective technologies for reducing the concentration of CO<sub>2</sub> in the atmosphere. Considering that CO<sub>2</sub> is an essential C1 resource for various industrial processes and plant growth, the rational conversion of CO<sub>2</sub> into high-value chemicals has emerged as a clean carbon-neutral strategy.<sup>141</sup> This approach

**Table 1** Comparison of the POM-based and POM-derived materials in this review for HER performance

| Electrocatalysts                            | Electrolyte                          | <i>j</i><br>(mA cm <sup>-2</sup> ) | $\eta$<br>(mV) | Tafel slope<br>(mV dec <sup>-1</sup> ) | Ref. |
|---|--------------------------------------|------------------------------------|----------------|--|------|
| NENU-500                                    | 0.5 M H <sub>2</sub> SO <sub>4</sub> | 10                                 | 237            | 96                                     | 78   |
| NENU-501                                    | 0.5 M H <sub>2</sub> SO <sub>4</sub> | 10                                 | 392            | 137                                    | 78   |
| P <sub>2</sub> W <sub>48</sub> /rGO         | 0.5 M H <sub>2</sub> SO <sub>4</sub> | 10                                 | 28             | 38                                     | 79   |
| P <sub>2</sub> W <sub>18</sub> @rGF_ox      | 0.5 M H <sub>2</sub> SO <sub>4</sub> | 10                                 | 35             | 37                                     | 80   |
| P <sub>2</sub> W <sub>30</sub> @rGF_ox      | 0.5 M H <sub>2</sub> SO <sub>4</sub> | 10                                 | 33             | 33                                     | 80   |
| P <sub>8</sub> W <sub>48</sub> @rGF_ox      | 0.5 M H <sub>2</sub> SO <sub>4</sub> | 10                                 | 44             | 41                                     | 80   |
| NiMo <sub>6</sub> O <sub>24</sub> @Cu/TNA   | 0.5 M H <sub>2</sub> SO <sub>4</sub> | 10                                 | 215            | 89.2                                   | 81   |
| POM@ZnCoS/NF                                | 1 M KOH                              | 10                                 | 170            | 53.5                                   | 90   |
| Mo <sub>2</sub> C@NC                        | 0.5 M H <sub>2</sub> SO <sub>4</sub> | 10                                 | 124            | 60                                     | 94   |
| P-W <sub>2</sub> C@NC                       | 0.5 M H <sub>2</sub> SO <sub>4</sub> | 10                                 | 89             | 53                                     | 95   |
| MoP/Mo <sub>2</sub> C@C                     | 0.5 M H <sub>2</sub> SO <sub>4</sub> | 10                                 | 89             | 45                                     | 96   |
| CoMoP@C                                     | 0.5 M H <sub>2</sub> SO <sub>4</sub> | 10                                 | 41             | 50                                     | 97   |
| Ni-Mo <sub>2</sub> C@C                      | 0.5 M H <sub>2</sub> SO <sub>4</sub> | 10                                 | 72             | 65.8                                   | 98   |
| Co <sub>2</sub> P/WC@NC                     | 0.5 M H <sub>2</sub> SO <sub>4</sub> | 10                                 | 91             | 40                                     | 99   |
| MoC <sub>x</sub> @C                         | 0.5 M H <sub>2</sub> SO <sub>4</sub> | 10                                 | 79             | 56                                     | 100  |
| Ni/WC@NC                                    | 0.5 M H <sub>2</sub> SO <sub>4</sub> | 10                                 | 53             | 43.5                                   | 101  |
| P-Mo <sub>2</sub> C@NC                      | 0.5 M H <sub>2</sub> SO <sub>4</sub> | 10                                 | 109            | 76                                     | 102  |
| MoPS/NC                                     | 0.5 M H <sub>2</sub> SO <sub>4</sub> | 10                                 | 120            | 52                                     | 103  |
| Mo <sub>2</sub> C@NPC/NPRGO                 | 0.5 M H <sub>2</sub> SO <sub>4</sub> | 10                                 | 34             | 33.6                                   | 104  |
| W <sub>x</sub> C@NC/NRGO                    | 0.5 M H <sub>2</sub> SO <sub>4</sub> | 10                                 | 100            | 58.4                                   | 105  |
| N@MoPC <sub>x</sub> -800                    | 0.5 M H <sub>2</sub> SO <sub>4</sub> | 10                                 | 108            | 69.4                                   | 106  |
| N@Mo <sub>2</sub> C-3/CFP                   | 0.5 M H <sub>2</sub> SO <sub>4</sub> | 10                                 | 56             | 51                                     | 107  |
| Co/WC@NC                                    | 0.5 M H <sub>2</sub> SO <sub>4</sub> | 10                                 | 129            | 93                                     | 108  |
| Co/WC@NC                                    | 1 M KOH                              | 10                                 | 142            | 91                                     | 108  |
| P-WN/rGO                                    | 0.5 M H <sub>2</sub> SO <sub>4</sub> | 10                                 | 85             | 54                                     | 109  |
| O-CoMoS                                     | 1 M KOH                              | 10                                 | 97             | 70                                     | 121  |
| CoS <sub>2</sub> @MoS <sub>2</sub> @CC-30 h | 0.5 M H <sub>2</sub> SO <sub>4</sub> | 10                                 | 65             | 122                                    | 123  |
| Fe-Mo-S/Ni <sub>3</sub> S <sub>2</sub> @NF  | 1 M KOH                              | 10                                 | 141            | 123                                    | 53   |
| defect-rich MoS <sub>2</sub>                | 0.5 M H <sub>2</sub> SO <sub>4</sub> | 13                                 | 200            | 50                                     | 126  |
| MoS <sub>2</sub> /N-RGO-180                 | 0.5 M H <sub>2</sub> SO <sub>4</sub> | 10                                 | 56             | 41.3                                   | 127  |
| CoMoS/KB                                    | 1 M KOH                              | 10                                 | 81             | 64                                     | 128  |
| NiO@1T-MoS <sub>2</sub>                     | 1 M KOH                              | 10                                 | 46             | 52                                     | 133  |
| {PtW <sub>6</sub> }/C                       | 0.5 M H <sub>2</sub> SO <sub>4</sub> | 10                                 | 22             | 29.8                                   | 137  |
| Pt <sub>1</sub> -Mo <sub>2</sub> C-C        | 1 M KOH                              | 10                                 | 155            | 64                                     | 138  |

**Table 2** Comparison of the POM-based and POM-derived materials in this review for OER performance

| Electrocatalysts                                    | Electrolyte                          | <i>j</i><br>(mA cm <sup>-2</sup> ) | $\eta$<br>(mV) | Tafel slope<br>(mV dec <sup>-1</sup> ) | Ref. |
|---|--------------------------------------|------------------------------------|----------------|--|------|
| NiCo-POM/Ni   | 0.1 M KOH                            | 10                                 | 360            | 126                                    | 87   |
| Cs[Co-POM]  | 1 M H <sub>2</sub> SO <sub>4</sub>   | 10                                 | 466            | 98                                     | 88   |
| Ba[Co-POM]  | 1 M H <sub>2</sub> SO <sub>4</sub>   | 10                                 | 361            | 97                                     | 88   |
| POM@ZnCoS/NF  | 0.5 M H <sub>2</sub> SO <sub>4</sub> | 10                                 | 200            | 67.7                                   | 90   |
| 3-CoFeW   | 1 M KOH                              | 10                                 | 192            | 36                                     | 110  |
| P-NiMo <sub>4</sub> N <sub>5</sub> @Ni-1            | 1 M KOH                              | 100                                | 297            | 33.6                                   | 112  |
| Mo <sub>1</sub> -CoOOH@CP                           | 1 M KOH                              | 10                                 | 274            | 66                                     | 49   |
| Co-Mo <sub>2</sub> C                                | 1 M KOH                              | 10                                 | 190            | 94.3                                   | 113  |
| O-CoMoS   | 1 M KOH                              | 10                                 | 272            | 45                                     | 121  |
| Co <sub>5</sub> Mo <sub>10</sub> S <sub>x</sub> /CC | 1 M KOH                              | 10                                 | 153            | 57.8                                   | 122  |
| Fe-Mo-S/Ni <sub>3</sub> S <sub>2</sub> @NF          | 1 M KOH                              | 100                                | 300            | 98                                     | 53   |
| Fe-S-NiMoO <sub>4</sub> /MoO <sub>3</sub> @NF       | 1 M KOH                              | 10                                 | 212            | 41                                     | 61   |

not only addresses environmental issues caused by CO<sub>2</sub> but also offers a prospective means to meet future sustainable energy development. Structurally, CO<sub>2</sub> molecules are linear and centrally symmetric, characterized by high stability, a large energy gap, and low electron affinity,<sup>142,143</sup> making the activation of CO<sub>2</sub> a challenging process that requires significant energy input and stringent reaction conditions. Due to the environmental compatibility and mild reaction conditions, CO<sub>2</sub> reduction reactions (CO<sub>2</sub>RRs) have gained widespread attention, demonstrating the enormous potential for future industrial applications.<sup>5,144</sup> Nevertheless, the unregulated interaction between electrons and protons during the CO<sub>2</sub>RR has resulted in the emergence of multiple coupling processes, leading to a diverse range of reaction pathways. Consequently, the CO<sub>2</sub>RR often yields numerous distinct products, ultimately resulting in low FE and selectivity.<sup>145</sup> To date, various types of catalyst materials have been developed and applied in the CO<sub>2</sub>RR.<sup>146-148</sup> Although these catalysts have shown good CO<sub>2</sub>RR activity and selectivity, the sources of catalyst activity and the mechanisms for controlling selectivity are still unclear. A deeper understanding of the reaction mechanism and process of the CO<sub>2</sub>RR requires further research. Therefore, constructing well-defined heterogeneous CO<sub>2</sub>RR model catalysts is an important approach to elucidating the reaction mechanism of the CO<sub>2</sub>RR and designing efficient heterogeneous catalysts for the CO<sub>2</sub>RR.

#### 3.2.1. POM-based molecular materials for the CO<sub>2</sub>RR.

POMs have unique redox properties, excellent electron/proton storage and transport capabilities, and show significant potential in the photocatalytic and electrocatalytic reduction of CO<sub>2</sub>.<sup>19</sup> In addition, POMs possess abundant surface oxygen atoms, which exhibit Lewis basicity and can serve as potential active centers for CO<sub>2</sub> molecule activation and coupling.<sup>149</sup> Xu's group<sup>150</sup> demonstrated that metal atom-substituted heteropolyanions ((C<sub>3</sub>H<sub>5</sub>N<sub>2</sub>)<sub>3</sub>(C<sub>3</sub>H<sub>4</sub>N<sub>2</sub>)[PMo<sub>11</sub>CoO<sub>38</sub>(CO<sub>2</sub>)]·4H<sub>2</sub>O and (C<sub>3</sub>H<sub>5</sub>N<sub>2</sub>)<sub>4</sub>[SiMo<sub>11</sub>CoO<sub>38</sub>(CO<sub>2</sub>)]·4H<sub>2</sub>O) can undergo covalent interactions with CO<sub>2</sub> molecules through X-ray single-crystal diffraction. The bond angle of the covalently bonded CO<sub>2</sub> molecule showed a slight deviation, bending from 180° to 158.7°.



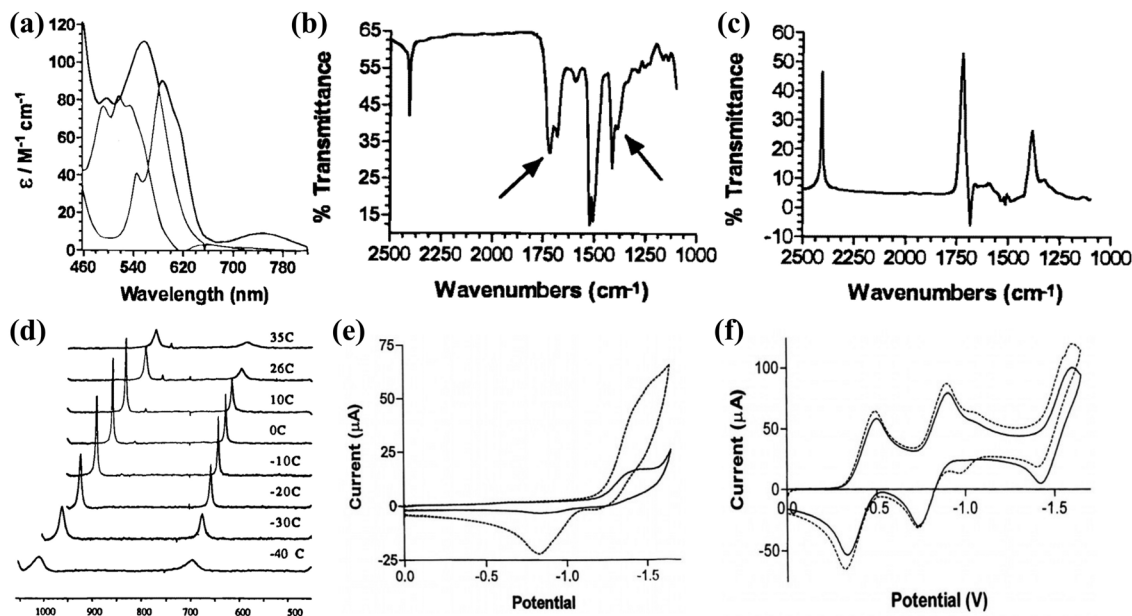


**Fig. 13** (a) Visible spectra of  $\alpha$ -[SiW<sub>11</sub>O<sub>39</sub>Co(OH<sub>2</sub>)]<sup>6-</sup>,  $\alpha$ -[SiW<sub>11</sub>O<sub>39</sub>Co(L)]<sup>6-</sup>, and  $\alpha$ -[SiW<sub>11</sub>O<sub>39</sub>Co(CO<sub>2</sub>)]<sup>6-</sup> in toluene. (b) Infrared spectrum of  $\alpha$ -[SiW<sub>11</sub>O<sub>39</sub>Co(CO<sub>2</sub>)]<sup>6-</sup> in CCl<sub>4</sub>. (c) Difference spectrum between  $\alpha$ -[SiW<sub>11</sub>O<sub>39</sub>Co(CO<sub>2</sub>)]<sup>6-</sup> and  $\alpha$ -[SiW<sub>11</sub>O<sub>39</sub>Co(L)]<sup>6-</sup>. (d) <sup>13</sup>C NMR spectra of  $\alpha$ -[SiW<sub>11</sub>O<sub>39</sub>Co(CO<sub>2</sub>)]<sup>6-</sup> in toluene at different temperatures.<sup>151</sup> Copyright 1998, American Chemical Society (ACS). (e) CV curves of SiW<sub>11</sub>Co in CH<sub>2</sub>Cl<sub>2</sub> before and after bubbling with CO<sub>2</sub> gas. (f) CV curves of P<sub>2</sub>W<sub>18</sub> in CH<sub>2</sub>Cl<sub>2</sub> before and after bubbling with CO<sub>2</sub> gas.<sup>152</sup> Copyright 2002, Springer.

This indicates that the metal atoms in the POMs clusters can immobilize and activate CO<sub>2</sub> molecules. Accordingly, POMs possess a well-defined structure and the potential to adsorb and activate CO<sub>2</sub>, making them suitable as a structural model for comprehending the crucial stages involved in the molecular-scale CO<sub>2</sub>RR reaction process.

The initial investigation into the catalytic activity of POMs in the CO<sub>2</sub>RR was studied by Kozik *et al.*<sup>151</sup> As illustrated in Fig. 13a–d, a series of spectroscopic experiments were applied to demonstrate the formation of POM–CO<sub>2</sub> complexes. Kozik *et al.*<sup>152</sup> prepared the first POMs catalyst,  $\alpha$ -[SiW<sub>11</sub>O<sub>39</sub>Co]<sup>6-</sup> (SiW<sub>11</sub>Co), capable of electrochemically catalyzing the CO<sub>2</sub>RR. Compared to the CV curve of SiW<sub>11</sub>Co in dichloromethane (CH<sub>2</sub>Cl<sub>2</sub>) electrolyte bubbled without CO<sub>2</sub>, the CV curve of SiW<sub>11</sub>Co in CH<sub>2</sub>Cl<sub>2</sub> electrolyte with CO<sub>2</sub> exhibited a higher reduction in current signal, suggesting that SiW<sub>11</sub>Co possesses high CO<sub>2</sub>RR activity. The CV curve of  $\alpha$ -[P<sub>2</sub>W<sub>18</sub>O<sub>62</sub>]<sup>6-</sup> (P<sub>2</sub>W<sub>18</sub>) without TM substitution remained largely unchanged in the CH<sub>2</sub>Cl<sub>2</sub> electrolyte before and after CO<sub>2</sub> bubbling, indicating that TM-substituted POMs play a key role in the CO<sub>2</sub>RR (Fig. 13f). Therefore, the future direction for constructing efficient and highly selective CO<sub>2</sub>RR catalysts based on POMs in aqueous electrolytes lies in the creation of stable, multiphase CO<sub>2</sub>RR active sites. This work provides design principles and guidance for the development of novel heterogeneous CO<sub>2</sub>RR electrocatalysts.

**3.2.2. POM-involved materials for the CO<sub>2</sub>RR.** Designing POM-based heterogeneous electrocatalysts has emerged as a challenging approach for designing CO<sub>2</sub>RR catalysts owing to the solubility of various POMs in aqueous solutions. Constructing POM-involved inorganic–organic hybrid materials can significantly

reduce the solubility of POMs, and integrate organic molecular catalysts with CO<sub>2</sub>RR activity into POMs. Therefore, designing POM-involved inorganic–organic hybrid materials becomes an ideal strategy for constructing novel CO<sub>2</sub>RR electrocatalysts.<sup>16</sup> Du *et al.*<sup>145</sup> prepared a series of POM-carbonyl manganese compounds (abbreviated as POM–MnL) and used them as heterogeneous electrocatalysts for the CO<sub>2</sub>RR (Fig. 14a). Among them, SiW<sub>12</sub>–MnL displayed the most significant electrocatalytic activity, selectively reducing CO<sub>2</sub> to CO. Various characterizations combined with DFT results indicated that the electron transfer process between the POMs and MnL units can suppress the competing HER, enabling efficient CO<sub>2</sub> reduction to CO (Fig. 14b). Furthermore, by changing the type of POMs in the POM–MnL composite catalyst, the electron transfer pathway can be regulated (Fig. 14c), allowing for control of the FE in the CO<sub>2</sub>RR. Wang's group<sup>153</sup> developed a method to incorporate PMO<sub>12</sub> into Zn–CoTAPc double molecular layer sandwich nanosheets (MLSS). Various characterizations confirmed that the nanosheet had a thickness of ~1.2 nm and consisted of two reticular layers of Zn–CoTAPc with interlayered PMO<sub>12</sub> anions (Fig. 14d). This unique structure provided highly exposed Co active sites and structural stability against stacking and deactivation. The MLSSs showed exceptional catalytic performance in the CO<sub>2</sub>RR, and the performance of MLSSs was further enhanced with external light irradiation (Fig. 14e and f).

Furthermore, Lan's group has previously reported various series of POMOF materials as heterogeneous catalysts for electrocatalytic CO<sub>2</sub>RRs.<sup>154–156</sup> They conducted a hydrothermal method to prepare a series of stable POM-metalloporphyrin organic framework (POMOF) materials for electrocatalytic CO<sub>2</sub>RRs (Fig. 15a).<sup>154</sup> The research findings revealed that the



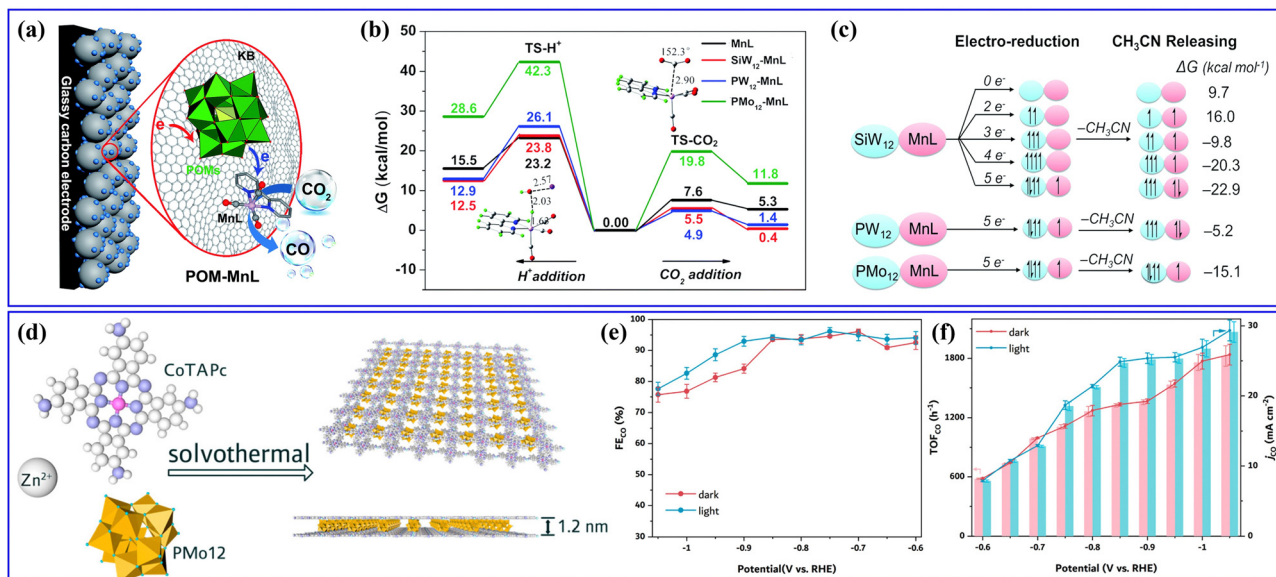


**Fig. 14** (a) The  $\text{CO}_2\text{RR}$  reaction mechanism of POM-MnL. (b) Potential energy surfaces for  $\text{H}^+$  and  $\text{CO}_2$  addition to the respective active  $\text{CO}_2$  and  $\text{H}$  adducts. (c) The electronic configurations for the different reduction degree states.<sup>145</sup> Copyright 2020, Royal Society of Chemistry (RSC). (d) The synthetic procedure toward Zn-CoTAPc/PMo<sub>12</sub> MLs. (e)  $\text{FE}_{\text{CO}}$ -potential plots and (f)  $j_{\text{CO}}$  and  $\text{TOF}_{\text{CO}}$  plots of Zn-CoTAPc/PMo<sub>12</sub> MLs.<sup>153</sup> Copyright 2021, American Chemical Society (ACS).

TM in PMOFs plays a crucial role in the electrocatalytic  $\text{CO}_2\text{RR}$ . Among them, Co-modified PMOFs exhibited the highest  $\text{CO}_2\text{RR}$  activity (Fig. 15b). Although Co-PMOF exhibited higher  $\text{CO}_2\text{RR}$  activity than Co-TCPP, the electrocatalytic  $\text{CO}_2\text{RR}$  activity of PMOFs was still derived from the M-TCPP component, and the regulation of different types of POMs in this composite system needs to be further studied. Afterward, they synthesized a series of mixed-valence POM-based MOF composite catalysts (POM@PCN-222(Co), POM =  $[\text{Co}^{\text{III}}\text{Co}^{\text{II}}(\text{H}_2\text{O})\text{W}_{11}\text{O}_{39}]^{7-}$ , M = Co, Fe, Mn, and Ni) using a post-modification method<sup>155</sup> (Fig. 15c). The POM@PCN-222(Co) electrocatalyst combines the advantages of POMs and metalloporphyrin single metal sites, exhibiting highly efficient activity for electrocatalytic  $\text{CO}_2$  reduction to CO. DFT calculations indicated that POMs could facilitate the directed transfer of electrons from the electrode to the single metal sites, enriching the electron density of the Co center (Fig. 15d), which reduced the reaction energy barrier for the key rate-determining steps in the  $\text{CO}_2\text{RR}$  and enhanced the activity of electrocatalytic  $\text{CO}_2\text{RR}$ . In addition, metalloporphyrins (M-TCPPs) were used to construct a series of POM-based MOF (M-POMOFs:  $[\text{PMo}^{\text{V}}_8\text{Mo}^{\text{VI}}_4\text{O}_{35}(\text{OH})_5\text{Zn}^{\text{II}}_4]_2[\text{Fe}^{\text{III}}\text{-TCPP-Cl}]$  Guest;  $[\text{PMo}^{\text{V}}_8\text{Mo}^{\text{VI}}_4\text{O}_{35}(\text{OH})_5\text{Zn}^{\text{II}}_4]_2[\text{M}^{\text{II}}\text{-TCPP}][\text{H}_2\text{O}]$  Guest; M = Zn, Ni, Cu, Co, and Mn) for photo- and electrocatalytic  $\text{CO}_2\text{RR}$  (PCR and ECR) by Lan's group<sup>156</sup> (Fig. 15e). This study aimed to uncover the role of single metal sites and clusters in catalysis. In the ECR (Fig. 15f), the Fe-POMOF catalyst exhibited a superior FE in converting  $\text{CO}_2$  to CO. Their research contributed to understanding the relationships between single metal sites and cluster catalysis.

In addition, POMs can also be used as reducing agents and stabilizers, which are widely applied in the synthesis of nanomaterials. Guo *et al.* synthesized a series of silver nanocluster

catalysts reduced by electrodeposition with PMo<sub>12</sub> (Ag-PMO)<sup>157</sup> or bovine serum albumin (BSA), subsequently modified by SiW<sub>12</sub> (AgNC@BSA-SiW).<sup>158</sup> The incorporation of POMs as electron transfer mediators resulted in significantly improved efficiency of the silver nanocluster catalysts in the reduction of  $\text{CO}_2$  to CO, surpassing the performance of bulk Ag. Wei's group<sup>159</sup> utilized Mo<sub>8</sub>-type POM-modified copper nanocubes for electrocatalytic  $\text{CO}_2$  reduction to produce acetic acid. The Mo<sub>8</sub>-modified Cu nano-catalyst can efficiently convert  $\text{CO}_2$  to acetic acid with a high FE. DFT calculations revealed that the POMs modification facilitates the formation of abundant Cu-O-Mo active sites, promoting the generation of  $^*\text{CH}_3$  intermediates and facilitating their coupling with  $\text{CO}_2$  molecules, ultimately leading to the production of acetic acid. This work demonstrated the control of the Cu nano-catalyst interface *via* POM modification, enabling deep reduction of  $\text{CO}_2$  and providing guidance for the regulation of  $\text{CO}_2$  reduction depth using POMs. The summary of POM-involved materials for electrocatalytic  $\text{CO}_2\text{RR}$  in this review is shown in Table 3.

The above research demonstrates the application of a series of POM-involved catalysts in electrocatalytic  $\text{CO}_2\text{RR}$ s. These results indicate that when POMs are combined with organic molecular catalysts possessing  $\text{CO}_2\text{RR}$  activity through electrostatic, covalent, or coordination interactions, the solubility of POM catalysts in the electrolyte can be significantly reduced, enabling the construction of heterogeneous POMs catalysts. These findings provide an explanation for the origin of activity in multi-component, multi-center composite electrocatalysts, thereby offering a deeper understanding of the design of heterogeneous  $\text{CO}_2\text{RR}$  electrocatalysts.





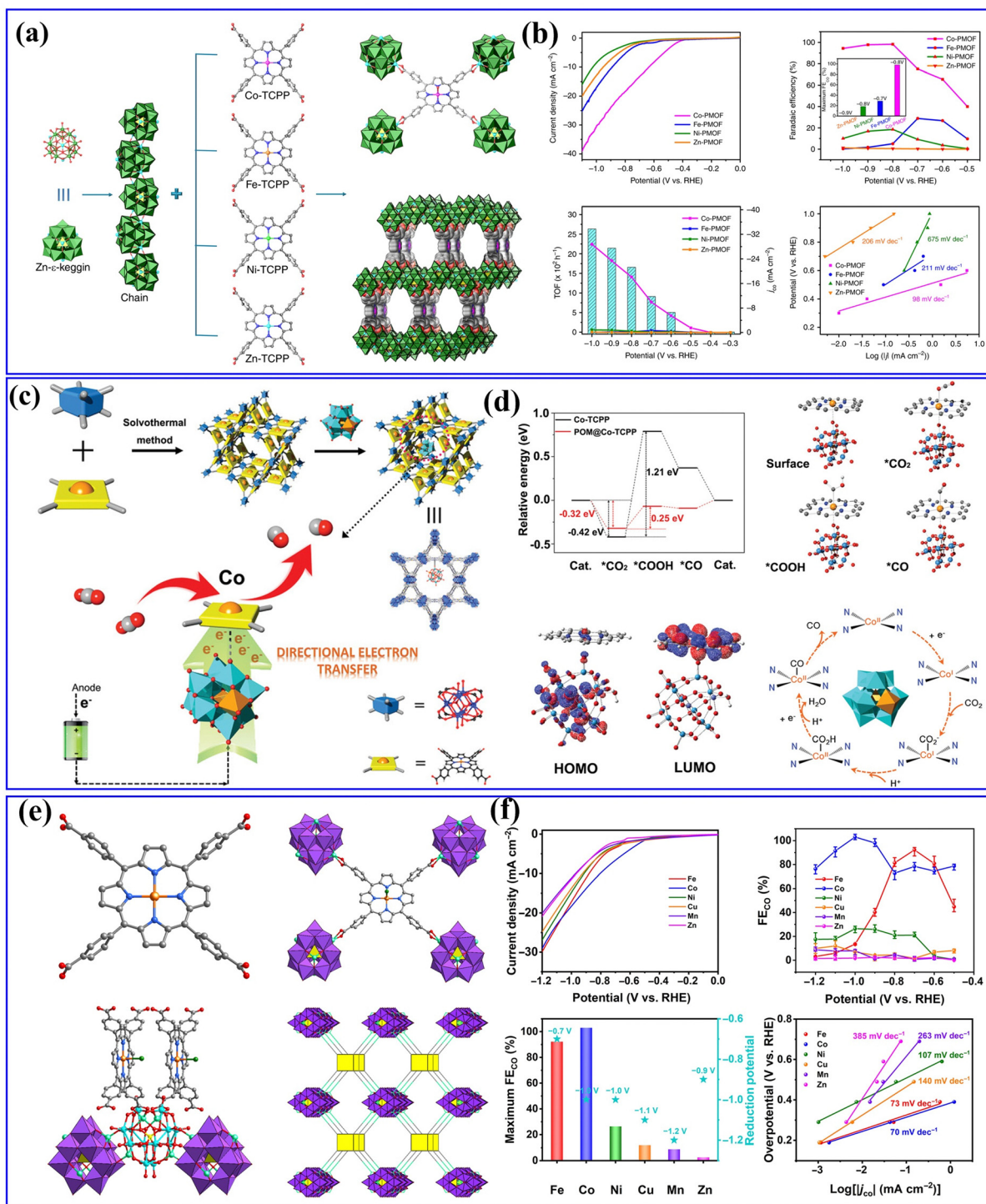


Fig. 15 (a) Schematic illustration of the structures of M-PMOFs. (b) Electrocatalytic performances of M-PMOFs.<sup>154</sup> Copyright 2018, Springer Nature. (c) A schematic diagram of the synthesis steps and reaction pathways of POM@PCN-222(Co). (d) DFT calculations of the CO<sub>2</sub>RR in H-POM@PCN-222(Co).<sup>155</sup> Copyright 2021, Wiley-VCH. (e) The crystal structures of M-POMOFs. (f) Electrocatalytic performances of M-POMOFs.<sup>156</sup> Copyright 2022, Science Publishing Group.

### 3.3. N<sub>2</sub> reduction reaction

Ammonia (NH<sub>3</sub>), as a hydrogen-rich carrier with great potential, is an important next-generation green energy source for fuel cells.<sup>160</sup> However, industrial ammonia synthesis still relies on the traditional Haber-Bosch method, which requires high temperature

(400–600 °C) and high pressure (20–40 MPa), accounting for 1–2% of global energy consumption, as well as large CO<sub>2</sub> emissions.<sup>161,162</sup> Therefore, exploring the green environmental protection ammonia synthesis technology with normal temperature and pressure is essential for converting intermittent energy sources



Table 3 The summary of the POM-involved materials for electrocatalytic CO<sub>2</sub>RR in this review

| Electrocatalyst                          | Electrolyte             | Potential       | Principal product    | FE (%) | Ref. |
|--|-------------------------|-----------------|----------------------|--------|------|
| SiW <sub>12</sub> -MnL/KB                | 0.5 M KHCO <sub>3</sub> | -0.72 V vs. RHE | CO                   | 95     | 145  |
| PW <sub>12</sub> -MnL/KB                 | 0.5 M KHCO <sub>3</sub> | -0.72 V vs. RHE | CO                   | 80     | 145  |
| PMo <sub>12</sub> -MnL/KB                | 0.5 M KHCO <sub>3</sub> | -0.52 V vs. RHE | CO                   | 65     | 145  |
| MnL/KB                                   | 0.5 M KHCO <sub>3</sub> | -0.72 V vs. RHE | CO                   | 65     | 145  |
| Zn-CoTAPc/PMo <sub>12</sub> MLSS (dark)  | 0.5 M KHCO <sub>3</sub> | -0.7 V vs. RHE  | CO                   | 96.1   | 153  |
| Zn-CoTAPc/PMo <sub>12</sub> MLSS (light) | 0.5 M KHCO <sub>3</sub> | -0.75 V vs. RHE | CO                   | 96.2   | 153  |
| Co-PMOF                                  | 0.5 M KHCO <sub>3</sub> | -0.8 V vs. RHE  | CO                   | 98.7   | 154  |
| Fe-PMOF                                  | 0.5 M KHCO <sub>3</sub> | -0.7 V vs. RHE  | CO                   | 28.8   | 154  |
| Ni-PMOF                                  | 0.5 M KHCO <sub>3</sub> | -0.8 V vs. RHE  | CO                   | 18.5   | 154  |
| Zn-PMOF                                  | 0.5 M KHCO <sub>3</sub> | -0.9 V vs. RHE  | CO                   | 0.95   | 154  |
| H-POM@PCN-222(Co)                        | 0.5 M KHCO <sub>3</sub> | -0.8 V vs. RHE  | CO                   | 96.2   | 155  |
| M-POM@PCN-222(Co)                        | 0.5 M KHCO <sub>3</sub> | -0.8 V vs. RHE  | CO                   | 91.2   | 155  |
| L-POM@PCN-222(Co)                        | 0.5 M KHCO <sub>3</sub> | -0.8 V vs. RHE  | CO                   | 71.2   | 155  |
| Fe-PMOF                                  | 0.5 M KHCO <sub>3</sub> | -0.7 V vs. RHE  | CO                   | 92.1   | 156  |
| Mo <sub>8</sub> @Cu/TNA                  | NaHCO <sub>3</sub>      | -1.13 V vs. RHE | CH <sub>3</sub> COOH | 48.68  | 159  |

(such as solar energy and electricity) into continuous ammonia fuel that can be stored and transported anytime and anywhere.

Electrocatalytic nitrogen reduction reaction (NRR) has low energy consumption that can be carried out at room temperature and pressure, which is the most likely method to replace the traditional Hubble method for the production of NH<sub>3</sub>.<sup>163–165</sup> However, the Faraday efficiency of the NRR is still relatively low due to the limitation of thermodynamics and kinetics.<sup>166</sup> In terms of thermodynamics, N<sub>2</sub> molecules are extremely chemically stable under natural conditions and are difficult to activate.<sup>167</sup> From a kinetic point of view, the main challenge of the NRR is the high dissociation energy of nitrogen and the serious side reaction of hydrogen evolution.<sup>163,168</sup> Thus, it is necessary to demand the development of highly active electrocatalysts that can effectively reduce the activation energy of N<sub>2</sub> reduction and inhibit the side reaction of hydrogen evolution.

**3.3.1. POM-based materials for the NRR.** In the NRR process, POMs can be defined as an electron reservoir to provide electrons directly to N<sub>2</sub> molecules, which is beneficial to the activation of N<sub>2</sub> molecules.<sup>57,58</sup> Besides, POMs have been proved by DFT calculations to be an electron source pointing to the active site in the NRR process.<sup>57</sup> Hence, POM-based materials can be used as an ideal candidate catalyst for the NRR in both experimental and theoretical studies.

Recently, Liao *et al.*<sup>169</sup> synthesized Mo-PTA@CNT catalyst by immobilizing Mo-PTA (PTA = H<sub>3</sub>PW<sub>12</sub>O<sub>40</sub>) on multi-walled CNT (Fig. 16a), in which Mo-PTA could efficiently adsorb and activate N<sub>2</sub> molecules, and CNT could enrich the N<sub>2</sub> concentration and accelerate NRR electron transfer. Thus, the as-prepared Mo-PTA@CNT exhibited high NRR activity with an NH<sub>3</sub> yield rate and FE value (Fig. 16b). Yang *et al.*<sup>57</sup> integrated POMs into stable MOFs to construct POMOFs (Fe<sub>x</sub>Co<sub>y</sub>MOF-P<sub>2</sub>W<sub>18</sub>) for the NRR (Fig. 16c). In the Fe<sub>x</sub>Co<sub>y</sub>MOF-P<sub>2</sub>W<sub>18</sub> catalyst, P<sub>2</sub>W<sub>18</sub> provided electron-rich centers and increased the electron transfer capacity, whereas the Fe<sub>x</sub>Co<sub>y</sub>MOF skeletons increased the stability of the reduced electron-rich POMs. Benefiting from the synergistic effect between POMs and MOFs, the Fe<sub>x</sub>Co<sub>y</sub>MOF-P<sub>2</sub>W<sub>18</sub> catalyst showed excellent electrocatalytic NRR activity. It can be observed from Fig. 16d that the FeCoMOF-P<sub>2</sub>W<sub>18</sub> catalyst exhibited the highest NH<sub>3</sub> yield rate (47.04 μg h<sup>-1</sup>) and FE

(31.76%) as compared to other Fe<sub>x</sub>Co<sub>y</sub>MOF-P<sub>2</sub>W<sub>18</sub>. Feng *et al.*<sup>170</sup> fabricated an Ag/PW<sub>12</sub>/Zr-mTiO<sub>2</sub> composite with a mesoporous structure through one-pot synthesis (Fig. 16e), which showed superior activity in photo- and electro-driven NRR. In the Ag/PW<sub>12</sub>/Zr-mTiO<sub>2</sub> composite, Ag NPs and PW<sub>12</sub> facilitated charge transfer efficiency due to interface engineering, whereas doping Zr in mTiO<sub>2</sub> significantly promoted chemisorption of N<sub>2</sub>, together with enhanced active sites and the production rate of NH<sub>3</sub>/NH<sub>4</sub><sup>+</sup>. As a result, the Ag/PW<sub>12</sub>/Zr-mTiO<sub>2</sub> composite could reach an NH<sub>3</sub>/NH<sub>4</sub><sup>+</sup> production rate of 324.2 μmol g<sub>cat</sub><sup>-1</sup> h<sup>-1</sup> in a photo-driven NRR process and 55 μg g<sub>cat</sub><sup>-1</sup> h<sup>-1</sup> in an electro-driven NRR process.

In addition, some researchers also proved the superiority of POM-based materials as NRR catalysts by DFT calculations. Gao *et al.*<sup>171</sup> calculated phosphotungstic acid (PTA)-supported single metal and proved that the M-PTA showed high NRR activity (Fig. 17a and b). Lin *et al.*<sup>172</sup> developed a series of POM (SiMA, SiTA, PMA, and PTA) supported Ru single atoms as NRR electrocatalysts (Fig. 17c). Among them, Ru-PMA and Ru-PTA displayed excellent NRR activity in the entire reactions. Talib *et al.*<sup>173</sup> proved that the NRR mechanisms of Mo<sub>1</sub>/PMA SAC as an NRR catalyst for activating N<sub>2</sub> to convert NH<sub>3</sub> were the enzymatic pathway *via* DFT calculations. The Mo<sub>1</sub>/PMA catalyst could impede the competitive HER process, thus enhancing the selectivity of NRR (Fig. 17d). Wang *et al.*<sup>174</sup> anchored Ta atoms on a Ta-substituted POM support to form dual-atom catalysts (DACs) for the NRR. The DFT calculations suggested that the interaction between Ta and Ta-POM was the bonding interaction, and the POM carrier surface structure was sensitive to the Ta substituted effects (Fig. 17e). Lin *et al.*<sup>175</sup> manifested that the central heteroatoms (X = Fe, Co, Ni, Cu, Zn, Ga, Ge, As) of POMs could adjust the coordination environment of a single Mo atom (Fig. 17f), and Mo atoms supported the POM catalyst with the central heteroatoms of Co and As has higher NRR activity and a lower limiting potential.

**3.3.2 POM-derived materials for the NRR.** According to previous studies, Mo-based and W-based electrocatalysts exhibit highly active NRR catalysts.<sup>176,177</sup> POMs contain the highest oxidation state of early transition metals (Mo, W, V, *etc.*), which are considered as excellent platforms to construct Mo- and W-derived electrocatalysts.<sup>12,61</sup> Wang *et al.*<sup>178</sup> fabricated





Fig. 16 (a) Schematic diagrams of Mo-PTA and Mo-PTA@CNT. (b) NH<sub>3</sub> yield rates and faradaic efficiencies of Mo-PTA@CNT samples with different Mo loadings.<sup>169</sup> Copyright 2021, Wiley-VCH. (c) Proposed electron-transfer channel of Fe<sub>x</sub>Co<sub>y</sub>MOF and Fe<sub>x</sub>Co<sub>y</sub>MOF-P<sub>2</sub>W<sub>18</sub> for e-NRR. (d) *j*-*t* curve for 12 h of a continuous e-NRR process (inset: the NH<sub>3</sub> yields and FEs of before and after electrolysis for 12 h).<sup>57</sup> Copyright 2023, Wiley-VCH. (e) Schematic representation of synthesizing Ag/PW<sub>12</sub>/Zr-mTiO<sub>2</sub>.<sup>170</sup> Copyright 2021, Wiley-VCH.

Fe<sub>1.89</sub>Mo<sub>4.11</sub>O<sub>7</sub>/FeS<sub>2</sub>@C and FeMoO<sub>4</sub>/FeS<sub>2</sub>@C using PMo<sub>12</sub>@MIL-100(Fe)@PVP as the precursor (Fig. 18a). As presented in Fig. 18b, the Fe<sub>1.89</sub>Mo<sub>4.11</sub>O<sub>7</sub>/FeS<sub>2</sub>@C showed a high NH<sub>3</sub> yield rate and FE in acidic solution, higher than most reported NRR catalysts. Wang *et al.*<sup>179</sup> prepared a POM-derived CoS<sub>2</sub>/MoS<sub>2</sub> electrocatalyst with POMs (H<sub>3</sub>PMo<sub>12</sub>O<sub>40</sub>) as the precursor for the NRR, as shown in Fig. 18c. Compared with individual CoS<sub>2</sub> or MoS<sub>2</sub>, the CoS<sub>2</sub>/MoS<sub>2</sub> catalyst displayed an enhanced NRR activity (Fig. 18d), which was due to the bimetal synergistic effect improving the activation of nitrogen molecules and speeding up the charge transfer at the interface. Yang *et al.*<sup>180</sup> synthesized ternary oxide materials (MoFeO@X, X = 650, 750, 850) utilizing POMs (FeMo<sub>6</sub>) as the precursor. The FeMo<sub>6</sub> precursor was conducive to the formation of controllable multi-interfaces, and could also control the uniform dispersion of ternary oxide composite at the molecular level. The NH<sub>3</sub> yield rate and FE of the synthesized MoFeO@750 reached 16.57 μg h<sup>-1</sup> mg<sub>cat.</sub><sup>-1</sup> and 12.33% at -0.4 V vs. RHE in

0.1 mol L<sup>-1</sup> Na<sub>2</sub>SO<sub>4</sub> solution. Yin *et al.*<sup>177</sup> fabricated Pt-W/Mo@rGO-6 with PW<sub>6</sub>Mo<sub>6</sub> as the W/Mo platform (Fig. 18e), in which the Mo and W species exhibited a synergistic effect playing a critical role in the activation and dissociation of N<sub>2</sub>. As a result, the NH<sub>3</sub> yield of the Pt-W/Mo@rGO-6 electrocatalyst was reaching 79.2 μg h<sup>-1</sup> mg<sub>cat.</sub><sup>-1</sup> at -0.3 V vs. RHE. A summary of the POM-based materials and POM-derived materials for electrocatalytic NRR in this review is shown in Table 4.

## 4. The research process of POM-based materials for energy storage devices

### 4.1. Supercapacitors

Supercapacitors (SCs) have the advantages of large power, long cycles, and simple operation, which have become an ideal choice for electrochemical energy storage.<sup>181-183</sup> SCs contain





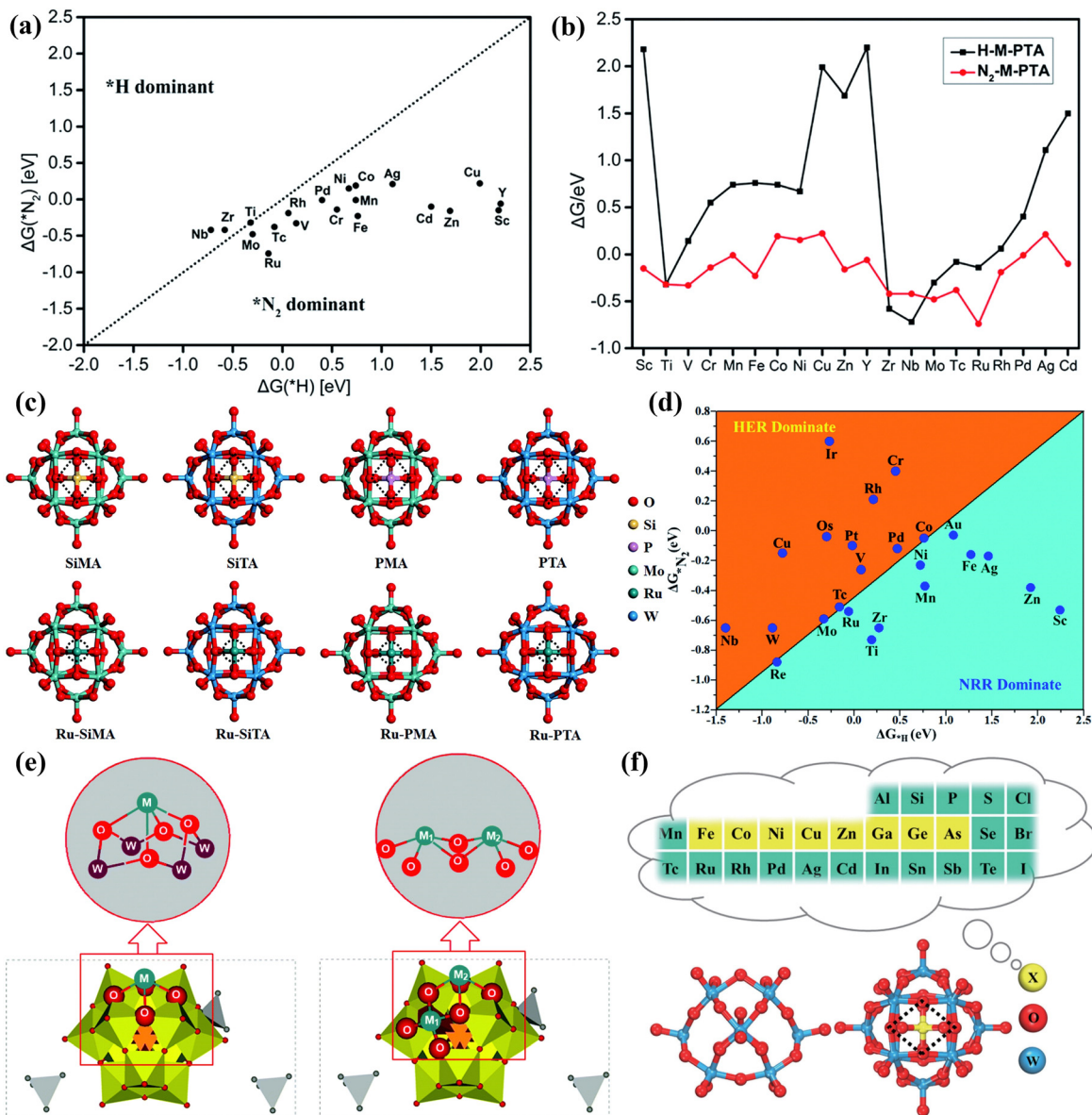


Fig. 17 (a) The calculated  $\Delta G(*\text{N}_2)$  and  $\Delta G(*\text{H})$  on M-PTA. (b) The Gibbs free energy of  $*\text{N}_2$  and  $*\text{H}$  adsorbed on M-PTA.<sup>171</sup> Copyright 2019, Royal Society of Chemistry (RSC). (c) Optimized structures of POM and Ru-POM.<sup>172</sup> Copyright 2020, Royal Society of Chemistry (RSC). (d) Calculated Gibbs free energies of  $\text{N}_2$  and  $\text{H}_2$  adsorbed on the  $\text{M}_1/\text{PMA}$  cluster.<sup>173</sup> Copyright 2022, Royal Society of Chemistry (RSC). (e) The structure of  $[\text{N}(\text{CH}_3)_4]^+[\text{Ta}^{II}/\text{POM}]$  (POM =  $[\text{PW}_{11}\text{O}_{39}]^{7-}$ ).<sup>174</sup> Copyright 2022, Royal Society of Chemistry (RSC). (f) Optimized structures of POM.<sup>175</sup> Copyright 2023, Springer, Tsinghua University Press 2022.

two main types, *i.e.*, an electrochemical double-layer capacitor that stores charge by reversibly adsorbing ions in the electrolyte and pseudocapacitors that work by relying on Faraday reactions.<sup>184</sup> POMs can achieve fast and reversible electron transfer, making them very suitable for use as pseudocapacitors.<sup>185</sup> However, the inherent low conductivity and high solubility of POMs in many solvents hinder their direct application as electrode materials of SCs.<sup>186</sup> Therefore, researchers immobilized POMs on chemically stable, high-surface-area carbon carriers to form mixed or nanocomposite electrochemical supercapacitor electrodes.<sup>22</sup> The carbon carrier can improve the conductivity, and simultaneously provide an electrochemical

double-layer capacitor to achieve a complementary effect with the Faraday charge storage of POM molecules.<sup>187–189</sup>

At present, researchers have prepared a variety of POM-based electrode materials, such as POM-CNT, POM-activated carbon (POM-AC), POM-porous carbon (POM-PC), POM-graphene (POM-GO), and POM-conductive polymer (POM-COP), *etc.* for SCs. Chen *et al.*<sup>190</sup> reported a novel nanocomposite material of SWCNT-TBA-PV<sub>2</sub>Mo<sub>10</sub> for the first time, which exhibited improved power density and energy density due to the redox activity of TBA-PV<sub>2</sub>Mo<sub>10</sub> in the material and the high conductivity and double-layer capacitance of SWCNTs. Nevertheless, the electrostatic bonding approach, while effective in introducing



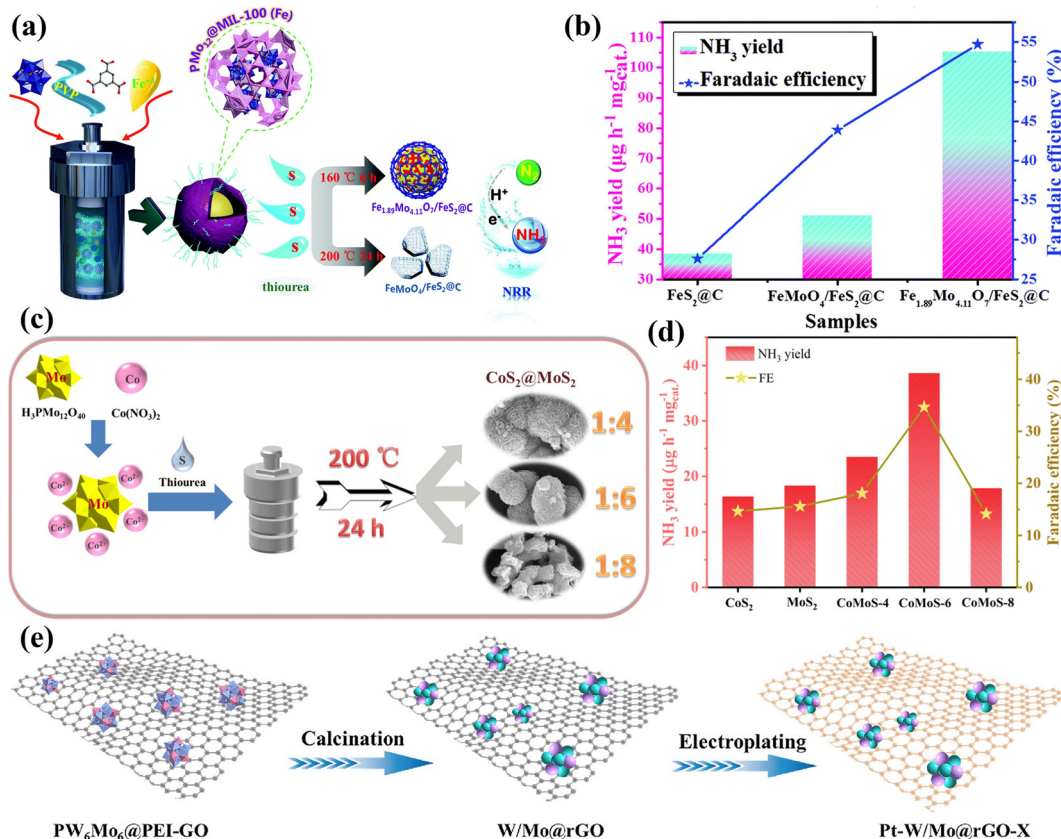


**Fig. 18** (a) An illustration of the preparation of Fe<sub>1.89</sub>Mo<sub>4.11</sub>O<sub>7</sub>/FeS<sub>2</sub>@C and FeMoO<sub>4</sub>/FeS<sub>2</sub>@C composites. (b) Comparison of the NH<sub>3</sub> yield rate and FE of the prepared electrodes.<sup>178</sup> Copyright 2020, Royal Society of Chemistry (RSC). (c) Schematic illustration for the one-step hydrothermal synthesis of CoS<sub>2</sub>/MoS<sub>2</sub> catalyst. (d) Comparison of NH<sub>3</sub> yield rate and FE of CoS<sub>2</sub>, MoS<sub>2</sub>, CoMoS-4, CoMoS-6, and CoMoS-8.<sup>179</sup> Copyright 2021, Elsevier Inc. (e) Schematic synthesis of Pt-W/Mo@rGO-X (*X* means the electroplating time).<sup>177</sup> Copyright 2023, Elsevier B.V.

**Table 4** A summary of POM-based and POM-derived materials for electrocatalytic NRR in this review

| Electrocatalyst   | Electrolyte                           | Potential       | NH <sub>3</sub> yield rate (μg h <sup>-1</sup> mgcat. <sup>-1</sup> ) | FE (%) | Ref. |
|---|---------------------------------------|-----------------|---|--------|------|
| Mo-PTA@CNT  | 0.1 M K <sub>2</sub> SO <sub>4</sub>  | -0.1 V vs. RHE  | 51 ± 1  | 81 ± 1 | 169  |
| FeCoMOF-P <sub>2</sub> W <sub>18</sub>                                    | 0.1 M HCl                             | -0.4 V vs. RHE  | 47.04   | 31.56  | 57   |
| Ag/PW <sub>12</sub> /Zr-mTiO <sub>2</sub>                                 | 0.05 M H <sub>2</sub> SO <sub>4</sub> | -0.6 V vs. RHE  | 55  | 2.2    | 170  |
| Fe <sub>1.89</sub> Mo <sub>4.11</sub> O <sub>7</sub> /FeS <sub>2</sub> @C | 0.5 M H <sub>2</sub> SO <sub>4</sub>  | -0.4 V vs. RHE  | 105.3   | 54.7   | 178  |
| Fe <sub>1.89</sub> Mo <sub>4.11</sub> O <sub>7</sub> /FeS <sub>2</sub> @C | 0.1 M KOH                             | -0.4 V vs. RHE  | 86.3  | 53.6   | 178  |
| CoS <sub>2</sub> /MoS <sub>2</sub>  | 1 M K <sub>2</sub> SO <sub>4</sub>    | -0.25 V vs. RHE | 38.61   | 34.66  | 179  |
| MoFeO@750   | 0.1 M Na <sub>2</sub> SO <sub>4</sub> | -0.4 V vs. RHE  | 16.57   | 12.33  | 180  |
| Pt-W/Mo@rGO-6   | 0.05 M H <sub>2</sub> SO <sub>4</sub> | -0.3 V vs. RHE  | 79.2  | 20     | 177  |

non-conductive molecules, often leads to undesired electron transfer and compromises the structural stability of POMs, thereby hindering their practical use in electrochemistry. To address the issue of leaching, Wang *et al.*<sup>191</sup> fabricated a 3D hybrid hydrogel (PMo<sub>12</sub>/PPy/CNT) employing an electrostatic co-assembly strategy. As illustrated in Fig. 19a, the PMo<sub>12</sub>/PPy/CNT consisted of a highly uniform and tightly distributed arrangement of individual PMo<sub>12</sub> molecules on PPy hydrogel-functionalized CNT. Compared with conventional composite systems, the PPy hydrogel linker, resembling a “fishnet” serving as the dual purpose of precisely confining the PMo<sub>12</sub> clusters in a supramolecular manner and ensuring efficient electrical contact between PMo<sub>12</sub> and CNTs (Fig. 19b and c).

As a result, the PMo<sub>12</sub>/PPy/CNT hybrid hydrogel exhibited enhanced supercapacitor performance compared to PMo<sub>12</sub>/PPy/CNT composite systems. Furthermore, the specific capacitance of the solid device remained stable even when subjected to various bending or twisting conditions (Fig. 19d). Yang *et al.*<sup>192</sup> developed a coaxial cable-like hybrid material (CNT/PMo/PANI) composed of CNTs, polyoxometalate (PMo), and polyaniline (PANI) (Fig. 19e and f). The PMo clusters and PANI played crucial roles as active centers for rapid and reversible redox reactions, contributing to pseudocapacitance.

The term “carbon material” specifically pertains to well-defined nano-structures of sp<sup>2</sup>-hybridized carbon. It has been observed that there exists a significant chemisorption interaction





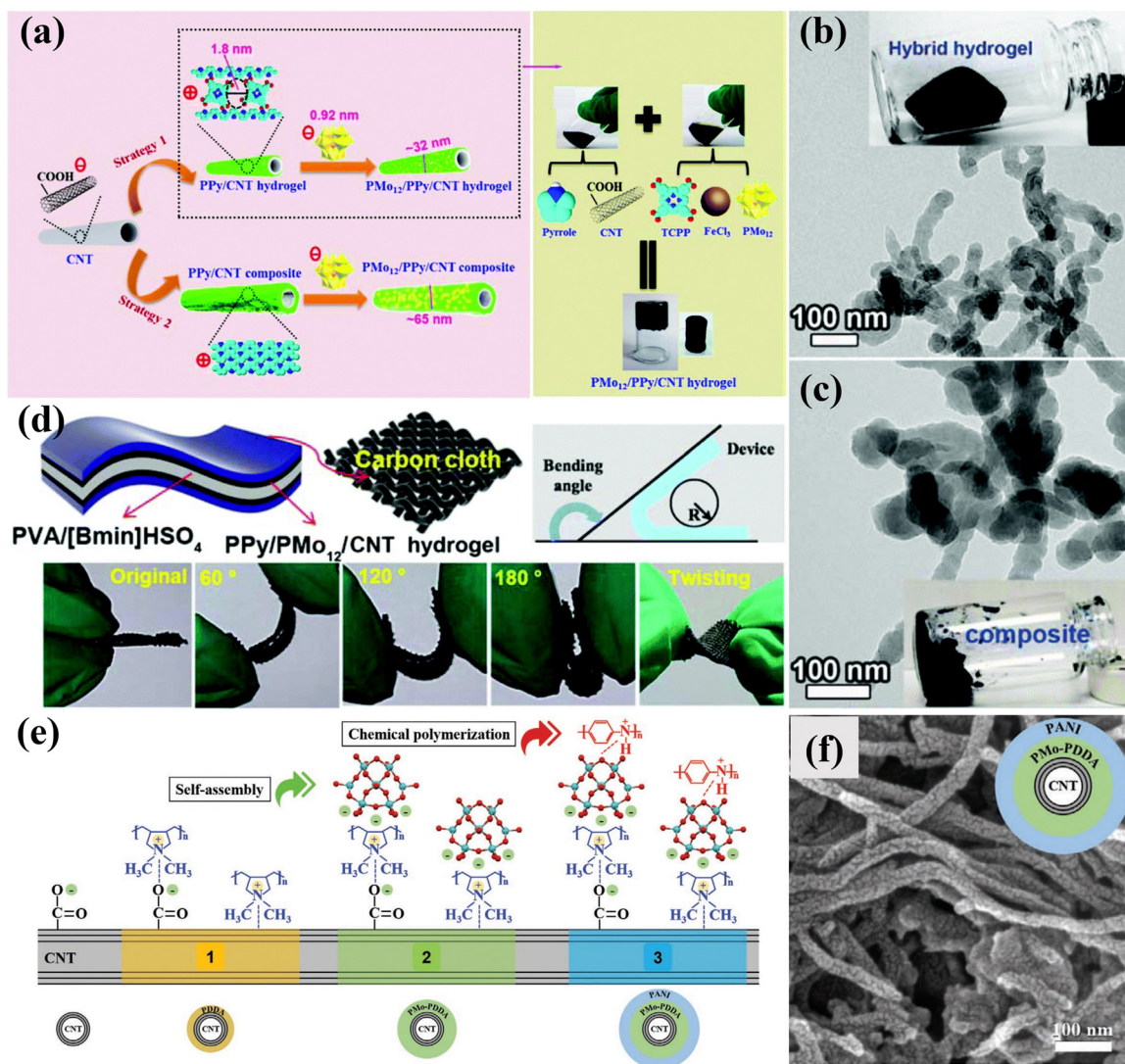


Fig. 19 (a) Fabrication process of  $\text{PMo}_{12}/\text{PPy}/\text{CNT}$ ; TEM images of (b)  $\text{PMo}_{12}/\text{PPy}/\text{CNT}$  hybrid hydrogel and (c)  $\text{PMo}_{12}/\text{PPy}/\text{CNT}$  composite. (d) Schematic drawing of the bent SSC and photographs of the flexible SSC under various flexible conditions.<sup>191</sup> Copyright 2020, Royal Society of Chemistry (RSC). (e) Schematic diagram of the synthesis mechanism for 1D coaxial cable-like  $\text{CNT}/\text{PMo}/\text{PANI}$ . (f) SEM image of  $\text{CNT}/\text{PMo}/\text{PANI}$ .<sup>192</sup> Copyright 2020, Wiley-VCH.

between POMs and carbon materials,<sup>22,193</sup> which is beneficial to the stability of the composite SCs electrode. Guevara *et al.*<sup>194</sup> applied  $\text{PW}_{12}$  adsorbed onto AC as electrode materials ( $\text{AC}-\text{PW}_{12}$ ) (Fig. 20a), resulting in an expanded voltage window of 1.6 V in acidic liquid electrolyte and a high capacitance of  $254 \text{ F g}^{-1}$  (Fig. 20b). However, the full potential of the pore structure in commercial AC has not been utilized, and the distribution of supported POMs remains uneven. Subsequently, Palomino *et al.*<sup>195</sup> made efforts to modify the pore size of AC to enhance the capacitance of  $\text{PMo}_{12}\text{-AC}$  (Fig. 20c). While this study successfully adjusted the pore size to enhance  $\text{PMo}_{12}$  dispersion, a significant issue remains with the occurrence of leaching or aggregation of  $\text{PMo}_{12}$  due to the presence of numerous mesopores (Fig. 20d). Consequently, precise control over the substrate hole size is crucial in addressing this challenge. Hu *et al.*<sup>196</sup> reported an  $\text{AC}@\text{PMo}_{12}$  composite material in which  $\text{PMo}_{12}$  was grown in

microporous carbon for SCs. As shown in Fig. 20e, the  $\text{AC}@\text{PMo}_{12}$  composite material exhibited a uniform distribution of  $\text{PMo}_{12}$  within the carbon pores. When  $\text{AC}@\text{PMo}_{12}$  was assembled into an asymmetric supercapacitor and subjected to constant current charging/discharging cycles in the P-IL electrolyte for 10 000 cycles, the capacitance of the device showed almost no decrease (Fig. 20f).

Researchers have discovered that POMs are more prone to adsorb within the pore size range of 1–2 nm in carbon-based substrates, enabling the achievement of exceptionally high POM loading.<sup>197</sup> Genovese *et al.*<sup>185</sup> used pine cones as a biotemplate for synthesizing a  $\text{PC}-\text{PMo}_{12}$  hybrid with a high specific surface area. Yang *et al.*<sup>54</sup> designed a unique type of porous carbon (referred to as micro-PC) with a monodisperse super-micropore size of  $\sim 1.09 \text{ nm}$ . Yang *et al.*<sup>198</sup> designed  $\text{PMo}_{12}$ -coupled RGO through a simple anion exchange process





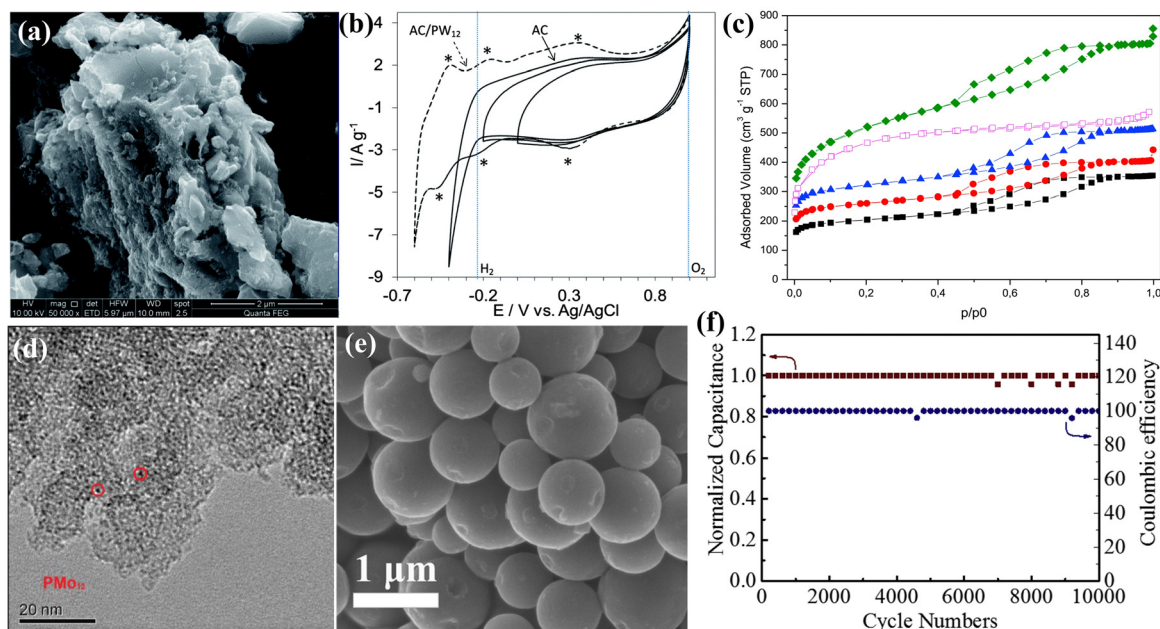


Fig. 20 (a) SEM image of the AC-PW<sub>12</sub> hybrid material. (b) CV curves for AC and AC-PW<sub>12</sub> at 10 mV s<sup>-1</sup>.<sup>194</sup> Copyright 2014, Royal Society of Chemistry (RSC). (c) Adsorption-desorption isotherms of the carbon support with different activation levels. (d) TEM image of C250-1-PMO<sub>12</sub>-5.<sup>195</sup> Copyright 2016, Elsevier Ltd. (e) SEM image of AC@PMO<sub>12</sub>. (f) Long-term cycling performance of the asymmetric supercapacitor (AC@PMO<sub>12</sub>//AC1) over 10 000 cycles at a current density of 10 A g<sup>-1</sup>.<sup>196</sup> Copyright 2016, Elsevier B.V.

(Fig. 21a), which showed a high density of POMs distributed individually on the surface of PIL-functionalized RGOs. As shown in Fig. 21b, PMO<sub>12</sub>-RGO displayed a high SCs performance. Hou *et al.*<sup>199</sup> reported two cases of POMs ([SiMo<sub>12</sub>O<sub>40</sub>]<sup>4-</sup>/[SiW<sub>12</sub>O<sub>40</sub>]<sup>4-</sup>) combined with metal cup aromatic compounds ([Ag<sub>5</sub>(C<sub>2</sub>H<sub>2</sub>N<sub>3</sub>)<sub>6</sub>]-[H<sub>5</sub>-c-SiMo<sub>12</sub>O<sub>40</sub>] and [Ag<sub>5</sub>(C<sub>2</sub>H<sub>2</sub>N<sub>3</sub>)<sub>6</sub>]-[H<sub>5</sub>-c-SiW<sub>12</sub>O<sub>40</sub>], [C<sub>2</sub>H<sub>2</sub>N<sub>3</sub> = 1H-1,2,4-triazole]) (Fig. 21c). They proposed that the oxidation ability of Keggin ions was the main influencing factor on the electrochemical performance of these POMs combined with metal cup aromatic compounds. Due to the synergistic effect of GO and POMs, the composite electrode achieved a maximum specific capacitance of 230.2 F g<sup>-1</sup> (Fig. 21d), which is higher than most reported POM electrode materials. Pakulski *et al.*<sup>200</sup> prepared a novel hybrid material of Mo<sub>132</sub>-DTAB-EEG with a porous 3D superstructure (Fig. 21e). Combining the redox activity of Mo<sub>132</sub> and the high conductivity of EEG, the Mo<sub>132</sub>-DTAB-EEG enabled a specific capacitance as high as 65 F g<sup>-1</sup>, as presented in Fig. 21f.

The polymer exhibits electrical conductivity primarily *via* the delocalized electrons in the main chain and utilizes the abundant functional groups or positive properties to support POMs by physical cross-linking and electrostatic interaction.<sup>201,202</sup> Liu *et al.*<sup>203</sup> prepared PMO<sub>12</sub>/PPy composite *via* anchored PMO<sub>12</sub> onto a highly interconnected 3D conductive polypyrrole (PPy) hydrogel scaffold (Fig. 22a). In a three-electrode system, the specific capacitance of the PMO<sub>12</sub>/PPy composite hydrogel was measured to be 776 F g<sup>-1</sup>, nearly 2.5 times higher than that of traditional PMO<sub>12</sub>/PPy composite materials (Fig. 22b). The solid-state supercapacitor achieved a maximum specific capacitance of 162.1 F g<sup>-1</sup> and an energy density of 50.66 Wh kg<sup>-1</sup> at a power density of 750 W kg<sup>-1</sup>, surpassing the electrochemical performance of other POMs or

metal oxides (Fig. 22c). The summary of POM-based electrode materials for SCs in this review is displayed in Table 5.

#### 4.2. Rechargeable batteries

Rechargeable batteries drive the global energy transition to renewable energy but are faced with resource constraints.<sup>204</sup> At present, the common rechargeable batteries include lithium-ion batteries (LIBs), lithium-sulfur batteries (LSBs), metal-ion batteries, metal-air batteries, *etc.*<sup>205</sup> The development of rechargeable batteries with high energy and power density, safety, long cycle life, fast response, and low cost is the goal of researchers.<sup>206</sup> Therefore, the design of high-performance electrode materials has important significance for improving the performance of rechargeable batteries.

**POM-based electrode materials for LIBs.** The high energy density of LIBs has always been a forefront topic in battery research. The performance of LIBs mainly depends on the active materials used for Li<sup>+</sup> storage electrodes.<sup>207</sup> The basic requirements for electrode materials include high reversible capacity, good cycling stability, high safety performance, low cost, and environmental friendliness.<sup>208,209</sup> It is necessary to use negative electrode materials with larger capacities and a faster Li<sup>+</sup> diffusion rate to enhance the energy and power density of LIBs.<sup>210</sup> Although different microscale materials such as metal oxides,<sup>211</sup> alloys,<sup>212</sup> and pyrolytic carbon<sup>213</sup> have been developed as negative electrode materials for LIBs, the morphological and structural changes associated with these microscale materials during battery operation pose limitations such as high electronic resistance, slow solid-state Li<sup>+</sup> diffusion rate, small surface area, and poor shape flexibility. Therefore,



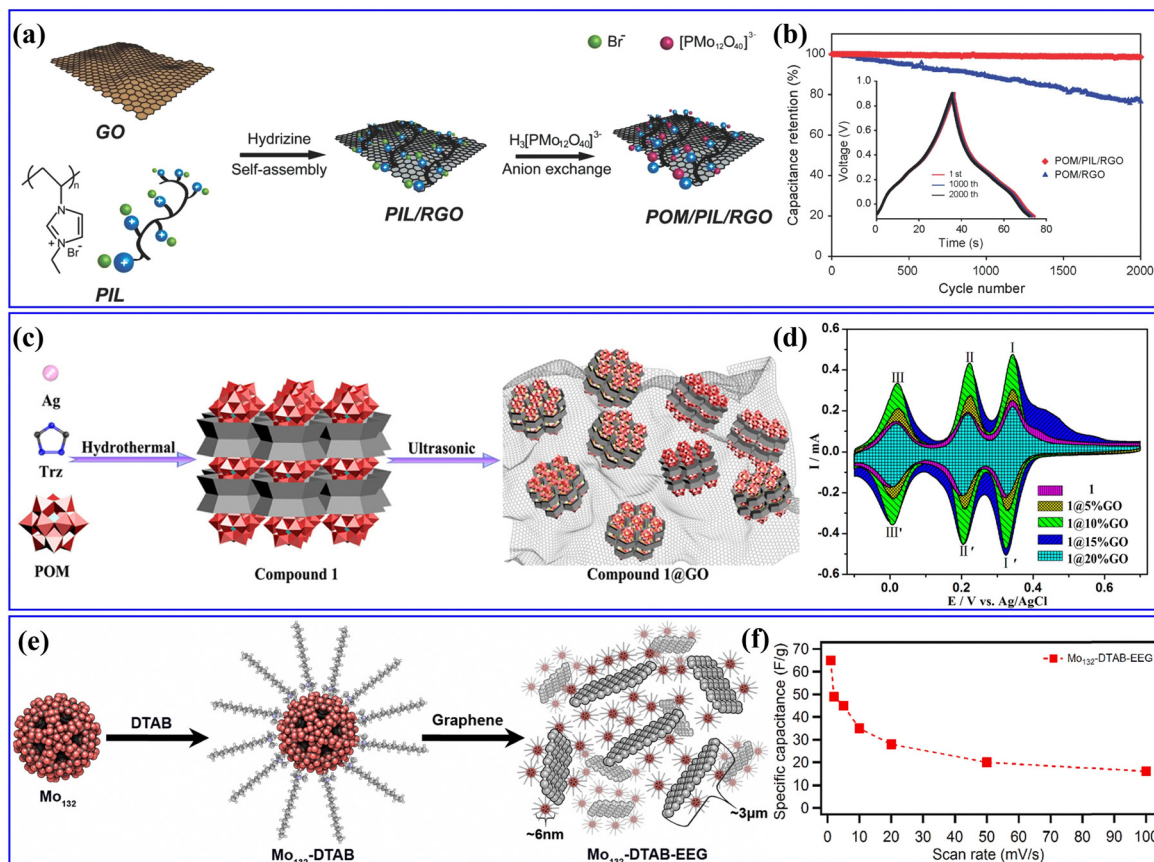


Fig. 21 (a) The synthetic process for the POM/PIL/RGO nanohybrids. (b) Capacitance retention of the POM/PIL/RGO and POM/RGO electrodes evaluated.<sup>198</sup> Copyright 2014, Wiley-VCH. (c) The synthetic route of compound 1@GO composite materials. (d) Comparison of CVs for 1- and 1@nGO-based electrodes.<sup>199</sup> Copyright 2019, American Chemical Society (ACS). (e) The formation process of Mo<sub>132</sub>-DTAB-EEG hybrid material. (f) Comparison of specific capacitance vs. scan rate for Mo<sub>132</sub>-DTAB-EEG.<sup>200</sup> Copyright 2018, Elsevier B.V.

current microscale structured negative electrode materials for LIBs, especially under high current density, still face issues such as poor cycling stability and insufficient charge/discharge capacity, which hinder the further development of current LIBs.

POMs, known for the high stability of thermodynamic and chemical, controllable size, precise structure, and the ability of high-valent metal ions in POMs to undergo multi-electron redox reactions during battery cycling, are considered potential electrode materials for LIBs.<sup>23,59</sup> Wang *et al.*<sup>214</sup> conducted a study using X-ray absorption fine structure analysis to study the structure and electronic states of PMo<sub>12</sub>, which indicated that when PMo<sub>12</sub> was applied as a positive electrode material for LIBs, the Mo<sup>6+</sup> ions in PMo<sub>12</sub> were reduced to Mo<sup>4+</sup> during the discharge process, accompanied by the transfer of 24 electrons (Fig. 23a). Their study revealed the behavior characteristics of PMo<sub>12</sub> as an “electron sponge” and demonstrated its significant potential as a high-performance electrode material for LIBs. Sonoyama *et al.*<sup>215</sup> utilized Anderson-type POMs Na<sub>3</sub>[AlMo<sub>6</sub>O<sub>24</sub>H<sub>6</sub>] (NAM) as a novel cathode material for high capacity and excellent stability in LIBs (Fig. 23b). The stability of the [AlMo<sub>6</sub>O<sub>24</sub>H<sub>6</sub>]<sup>3-</sup> during the charge–discharge process was investigated by *in situ* polycrystalline X-ray diffraction and Raman spectroscopy. This significant finding provided experimental

and theoretical evidence for the application of POMs and POM-based composite materials as electrode materials in LIBs.

V (50.96 g mol<sup>-1</sup>) has a lower relative molecular mass and higher redox capability as compared to Mo (95.96 g mol<sup>-1</sup>) and W (183.84 g mol<sup>-1</sup>). Thus, V-based POMs may exhibit a higher mass-energy density and specific capacity when used as battery electrodes. Subsequently, researchers have extensively explored the application of polyoxovanadates (POVs) as electrode materials in LIBs. Cronin's group<sup>216</sup> discovered that Li<sub>7</sub>[V<sub>15</sub>O<sub>36</sub>(CO<sub>3</sub>)] showed promising potential as a positive electrode material for LIBs (Fig. 23c). The V<sup>IV</sup> and V<sup>V</sup> in Li<sub>7</sub>[V<sub>15</sub>O<sub>36</sub>(CO<sub>3</sub>)] could reversibly gain and lose electrons during the charge–discharge process. Therefore, the pouch cell using Li<sub>7</sub>[V<sub>15</sub>O<sub>36</sub>(CO<sub>3</sub>)] as a positive electrode material exhibited excellent rate performance and cycling stability. Wang *et al.*<sup>217</sup> introduced a novel V-POM ([Ni(Phen)<sub>3</sub>][ClV<sub>14</sub>O<sub>34</sub>]Cl, NiV<sub>14</sub>) with a large-sized polycation containing multiple charges for studying its application as a negative electrode material in LIBs. The presence of the multi-charged large-sized polycation [Ni(Phen)<sub>3</sub>]<sup>2+</sup> in NiV<sub>14</sub> provided more stable open channels (Fig. 23d). The LIBs assembled with NiV<sub>14</sub> exhibited a high reversible capacity, high Coulombic efficiency and good stability (Fig. 23e). Electrochemical analysis indicated that capacitance-controlled charge storage processes



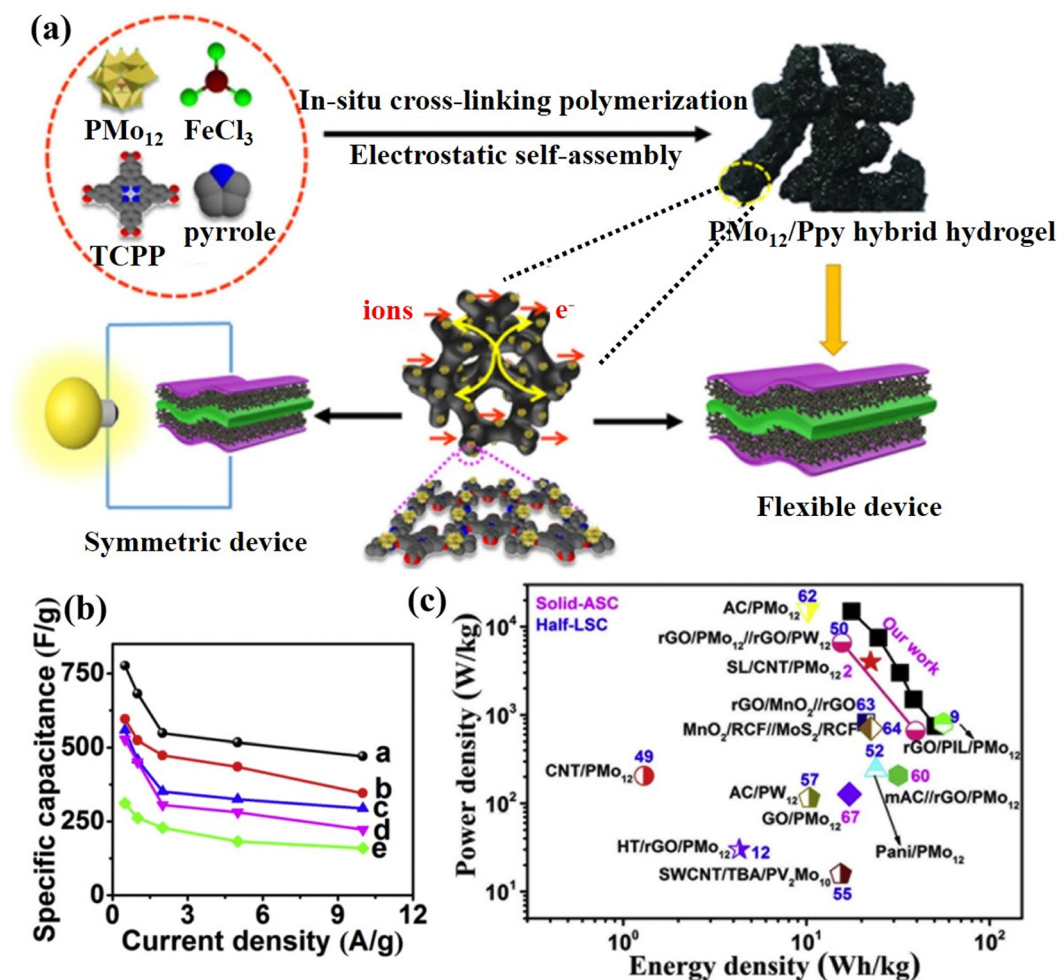


Fig. 22 (a) The preparation process for the  $\text{PMo}_{12}$ /PPy hybrid hydrogel for SCs. (b) Specific capacitances of the prepared samples at various current densities. (c) Ragone plots of the  $\text{P}_2$ -PPy gel// $\text{P}_2$ -PPy gel device compared with the values reported for other devices.<sup>203</sup> Copyright 2019, Elsevier Ltd.

Table 5 The summary of POM-based electrode materials for SCs in this review

| Electrode materials                           | Electrolyte                          | Specific capacitance                           | Energy density             | Capacitance retention | Ref. |
|---|--------------------------------------|--|----------------------------|-----------------------|------|
| SWCNT-TBA-PV <sub>2</sub> Mo <sub>10</sub>    | 1 M H <sub>2</sub> SO <sub>4</sub>   | 444 F g <sup>-1</sup> @2 A g <sup>-1</sup>     | 15.4 W h kg <sup>-1</sup>  | 95%@6500 cycles       | 190  |
| PMo <sub>12</sub> /PPy/CNT                    | 0.5 M H <sub>2</sub> SO <sub>4</sub> | 1170 F g <sup>-1</sup> @1 A g <sup>-1</sup>    | 67.5 μW h cm <sup>-2</sup> | 86%@3000 cycles       | 191  |
| CNT/PMo/PANI                                  | 1 M H <sub>2</sub> SO <sub>4</sub>   | 825 F g <sup>-1</sup> @5 A g <sup>-1</sup>     | 18.7 W h kg <sup>-1</sup>  | 85%@6000 cycles       | 192  |
| AC-PW <sub>12</sub>                           | 1 M H <sub>2</sub> SO <sub>4</sub>   | 254 F g <sup>-1</sup>                          | 2.32 W h cm <sup>-3</sup>  | 98%@30000 cycles      | 194  |
| C250-3-PMo <sub>12</sub> -2                   | 1 M H <sub>2</sub> SO <sub>4</sub>   | 285 F g <sup>-1</sup> @6 mA cm <sup>-2</sup>   | 10.2 W h kg <sup>-1</sup>  | —                     | 195  |
| AC@PMo <sub>12</sub>                          | acidic P-IL                          | 223 F g <sup>-1</sup> @1 mV s <sup>-1</sup>    | —                          | ~100%@10 000 cycles   | 196  |
| Pinecone AC/PMo <sub>12</sub> O <sub>40</sub> | 1 M H <sub>2</sub> SO <sub>4</sub>   | 361 F g <sup>-1</sup> @10 mV s <sup>-1</sup>   | —                          | 70%@5000 cycles       | 185  |
| PMo <sub>12</sub> @micro-PC                   | 0.5 M H <sub>2</sub> SO <sub>4</sub> | 443 mF cm <sup>-2</sup> @3 mA cm <sup>-2</sup> | 0.12 mW h cm <sup>-2</sup> | 81%@7500 cycles       | 54   |
| POM/PIL/RGO                                   | 0.5 M H <sub>2</sub> SO <sub>4</sub> | 408 F g <sup>-1</sup> @0.5 A g <sup>-1</sup>   | 56 W h kg <sup>-1</sup>    | 98%@2000 cycles       | 198  |
| Compound 1@15% GO                             | 0.5 M H <sub>2</sub> SO <sub>4</sub> | 230.2 F g <sup>-1</sup> @0.5 A g <sup>-1</sup> | —                          | 93%@1000 cycles       | 199  |
| Mo <sub>132</sub> -DTAB-EEG                   | 1 M H <sub>2</sub> SO <sub>4</sub>   | 65 F g <sup>-1</sup> @1 mV s <sup>-1</sup>     | —                          | 99%@5000 cycles       | 200  |
| PMo <sub>12</sub> /PPy                        | 1 M H <sub>2</sub> SO <sub>4</sub>   | 300 F g <sup>-1</sup> @5 A g <sup>-1</sup>     | 50.66 W h kg <sup>-1</sup> | 80%@1000 cycles       | 203  |

and fast Li<sup>+</sup> ion diffusion kinetics were the main factors contributing to the improved rate performance of the NiV<sub>14</sub> electrode.

Although POMs possess precise structures, tunable sizes, and excellent redox performance, their dissolvable nature in the electrolyte and low specific surface area of POMs lead to low capacity, poor stability, and shorter lifespan.<sup>218</sup> Additionally,

the uneven dispersion and aggregation of POM clusters hinder electron transfer between the material and the electrode, further impacting its cycling and rate performance. These drawbacks still limit the advance of POMs as electrode materials for LIBs. To address these issues, researchers have proposed combining POMs with other materials that have high specific surface areas or porous structures, such as conductive matrices,





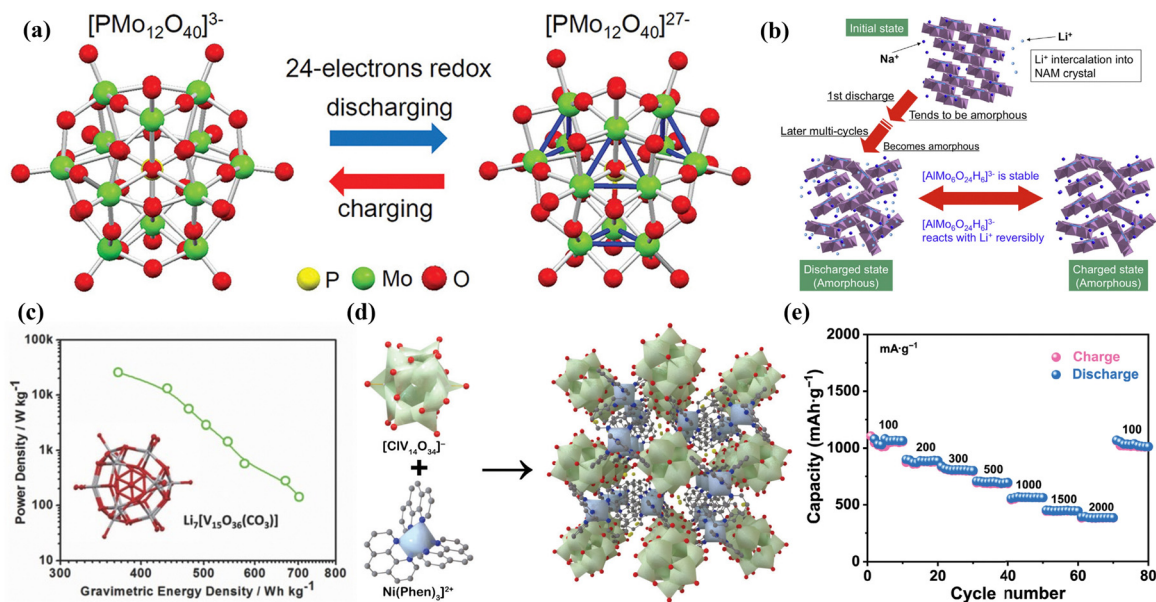


Fig. 23 (a) A schematic diagram of electron gain and loss during charge and discharge of  $\text{PMo}_{12}\text{O}_{40}$  cathode materials.<sup>214</sup> Copyright 2012, American Chemical Society (ACS). (b) A schematic image of the reaction mechanism for NAM.<sup>215</sup> Copyright 2014, Elsevier B.V. (c) Crystal structure of  $\text{Li}_7[\text{V}_{15}\text{O}_{36}(\text{CO}_3)]$  and its ratio of power to mass-energy density as the cathode material for LIBs.<sup>216</sup> Copyright 2015, Wiley-VCH. (d) View of polyanion, macrocation, and crystal structure of  $\text{NiV}_{14}$  along the [001] axis in polyhedron mode. (e) Rate performance at various current densities.<sup>217</sup> Copyright 2023, Tsinghua University Press.

Table 6 A summary of the POM-based electrode materials for LIBs reported in recent years

| Electrode materials                      | Electrode | Discharge capacities                                  | Rate performance   | Ref. |
|--|-----------|---|--|------|
| POM/CNT                                  | Anode     | $850 \text{ mA h g}^{-1}$ @ $0.5 \text{ mA cm}^{-2}$  | $1532 \text{ mA h g}^{-1}$ @ $0.05 \text{ mA cm}^{-2}$<br>$565 \text{ mA h g}^{-1}$ @ $1 \text{ mA cm}^{-2}$ | 219  |
| Py-Anderson-CNT                          | Anode     | $1899 \text{ mA h g}^{-1}$ @ $0.5 \text{ mA cm}^{-2}$ | $1072 \text{ mA h g}^{-1}$ @ $0.05 \text{ mA cm}^{-2}$<br>$480 \text{ mA h g}^{-1}$ @ $1 \text{ mA cm}^{-2}$ | 220  |
| CNTs-SiW <sub>11</sub>                   | Anode     | $1189 \text{ mA h g}^{-1}$ @ $0.5 \text{ mA cm}^{-2}$ | $802 \text{ mA h g}^{-1}$ @ $0.05 \text{ mA cm}^{-2}$<br>$584 \text{ mA h g}^{-1}$ @ $1 \text{ mA cm}^{-2}$  | 221  |
| POM/RGO-MCB                              | Cathode   | $67 \text{ A h kg}^{-1}$ @ $1.5 \text{ V}$            | —  | 222  |
| NAM-EDAG                                 | Anode     | $1835 \text{ mA h g}^{-1}$ @ $100 \text{ mA g}^{-1}$  | $1100 \text{ mA h g}^{-1}$ @ $100 \text{ mA g}^{-1}$<br>$400 \text{ mA h g}^{-1}$ @ $10 \text{ A g}^{-1}$    | 223  |
| Mn <sub>3</sub> V <sub>19</sub> -HIL/RGO | Cathode   | $214 \text{ mA h g}^{-1}$ @ $100 \text{ mA g}^{-1}$   | $121 \text{ mA h g}^{-1}$ @ $5 \text{ A g}^{-1}$<br>$73 \text{ mA h g}^{-1}$ @ $2 \text{ A g}^{-1}$          | 224  |
| Co-SiW@GO                                | Anode     | $452 \text{ mA h g}^{-1}$ @ $2 \text{ A g}^{-1}$      | $373 \text{ mA h g}^{-1}$ @ $0.1 \text{ A g}^{-1}$<br>$242 \text{ mA h g}^{-1}$ @ $5 \text{ A g}^{-1}$       | 225  |
| MF POMs/MXenes                           | Anode     | $297 \text{ mA h g}^{-1}$ @ $1.0 \text{ A g}^{-1}$    | $301 \text{ mA h g}^{-1}$ @ $0.1 \text{ A g}^{-1}$<br>$115 \text{ mA h g}^{-1}$ @ $4 \text{ A g}^{-1}$       | 226  |
| VM POMs/MXenes                           | Anode     | $196 \text{ W h kg}^{-1}$                             | $627 \text{ mA h g}^{-1}$ @ $0.1 \text{ A g}^{-1}$<br>$244 \text{ mA h g}^{-1}$ @ $4 \text{ A g}^{-1}$       | 227  |
| POMOF                                    | Anode     | $1525 \text{ mA h g}^{-1}$ @ $0.25 \text{ C}$         | $1525 \text{ mA h g}^{-1}$ @ $0.25 \text{ C}$<br>$1421 \text{ mA h g}^{-1}$ @ $1.25 \text{ C}$               | 228  |
| NNU-11                                   | Anode     | $1322 \text{ mA h g}^{-1}$ @ $50 \text{ mA g}^{-1}$   | —  | 229  |
| NAU3                                     | Anode     | $1406 \text{ mA h g}^{-1}$ @ $100 \text{ mA g}^{-1}$  | $488 \text{ mA h g}^{-1}$ @ $0.1 \text{ A g}^{-1}$<br>$283 \text{ mA h g}^{-1}$ @ $1 \text{ A g}^{-1}$       | 230  |
| POMOFs/RGO                               | Anode     | $2368 \text{ mA h g}^{-1}$ @ $50 \text{ mA g}^{-1}$   | $409 \text{ mA h g}^{-1}$ @ $2 \text{ A g}^{-1}$<br>$365 \text{ mA h g}^{-1}$ @ $3 \text{ A g}^{-1}$         | 231  |
| $\text{PMo}_{10}\text{V}_2$ -ILs@MIL-100 | Anode     | $1666 \text{ mA h g}^{-1}$ @ $100 \text{ mA g}^{-1}$  | $1033 \text{ mA h g}^{-1}$ @ $0.1 \text{ A g}^{-1}$<br>$348 \text{ mA h g}^{-1}$ @ $3 \text{ A g}^{-1}$      | 232  |

MOFs, composite materials, etc. By forming composites with these materials, it is possible to achieve uniform loading of POMs while maintaining a high specific surface area and porosity, thereby enhancing the functionality in conjunction with the conductive matrix or MOFs. The POM-based electrode materials for LIBs reported in recent years are summarized in Table 6.

*POM-based electrode materials for other rechargeable batteries.* POM-based materials are also applied as the electrode material for studies in lithium-sulfur batteries, metal-ion batteries and metal-air batteries. Wei's group<sup>233</sup> synthesized rGO-CNT/PW<sub>12</sub> as the cathodes in LSBs (Fig. 24a), which displayed  $1425 \text{ mA h g}^{-1}$  of specific capacities, and  $573 \text{ mA h g}^{-1}$  of rate capability. Their work confirmed the POM catalyst as a key structural element in the



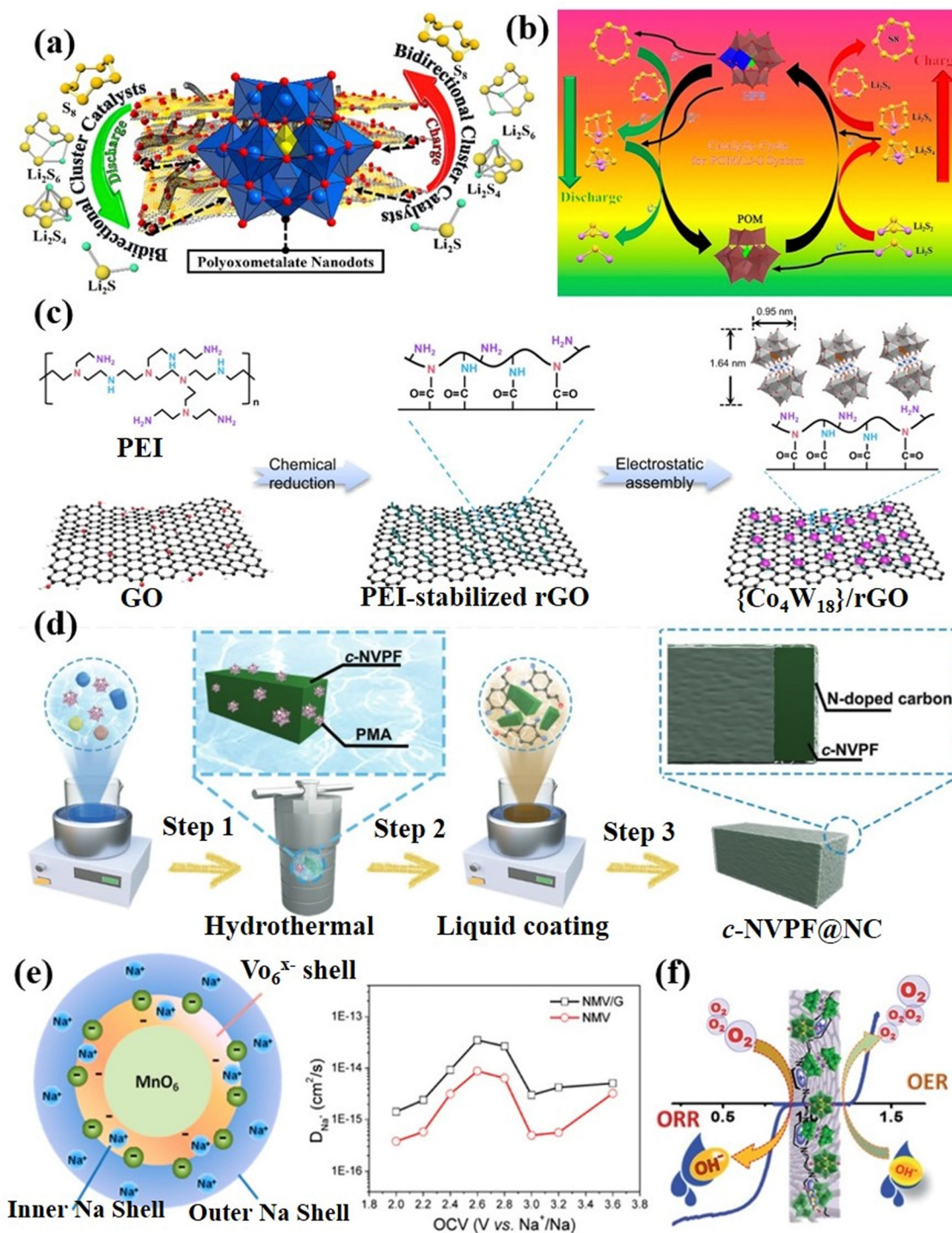


Fig. 24 (a) A schematic diagram of rGO-CNT/PW<sub>12</sub> as the cathode in LSBs. (b) The proposed catalytic scheme mediated by a Keggin-type (PW<sub>12</sub>) catalyst in a LSB system.<sup>233</sup> Copyright 2021, American Chemical Society (ACS). (c) A schematic diagram of the synthesis of {Co<sub>4</sub>W<sub>18</sub>}/rGO materials.<sup>234</sup> Copyright 2022, Springer Nature. (d) NVPF synthesis process.<sup>235</sup> Copyright 2023, Wiley-VCH GmbH. (e) Schematic illustration of Na ion storage in a notion of electron/ion sponge and the calculated Na-ion chemical diffusion coefficients.<sup>236</sup> Copyright 2017, American Chemical Society (ACS). (f) Scheme representing the bifunctional activity of the PVIM-CoPOM/NCNT composite towards both the OER and ORR.<sup>237</sup> Copyright 2021, Royal Society of Chemistry (RSC).

charging/discharging process of LSBs (Fig. 24b). In view of the shuttle effect of lithium polysulfides in LSBs, Chen's group<sup>234</sup> prepared {Co<sub>4</sub>W<sub>18</sub>}/rGO materials (Fig. 24c), which can not only

adsorb lithium polysulfides but also improve battery capacity and cycle performance. By using PMO<sub>12</sub> as a crystal growth regulator, Ren *et al.*<sup>235</sup> induced the oriented growth of Na<sub>3</sub>V<sub>2</sub>(PO<sub>4</sub>)<sub>2</sub>F<sub>3</sub> crystals



along the [110] crystal axis, and constructed a  $\text{Na}_3\text{V}_2(\text{PO}_4)_2\text{F}_3$  cathode material with continuous sodium ion diffusion channels for sodium ion batteries (Fig. 24d). Shen *et al.*<sup>236</sup> used an electron/ion sponge POM ( $\text{Na}_2\text{H}_8[\text{MnV}_{13}\text{O}_{38}]$ , NMV) as the cathode material for sodium-ion batteries (Fig. 24e). In NMV, it can accommodate 11 electron/ion pairs per mole content, which has a great contribution to the high capacitance of the material. Mandal *et al.*<sup>237</sup> fabricated a PVIM-CoPOM/NCNT composite with a high ORR and OER performance, as shown in Fig. 24f. As a result, the Zn-air battery performance using PVIM-CoPOM/NCNT as the air cathode exhibited a low charge-discharge potential gap and high energy density.

## 5 Conclusions and outlooks

In this review, recently developed POM-based and POM-derived materials in the field of water-splitting,  $\text{CO}_2$ RR, NRR, SCs, and LIBs are systematically summarized. The fundamental roles of POMs in clean energy conversion and storage systems are introduced. The material design principles have been emphasized, ranging from single clusters, assemblies, organic-inorganic hybrids to derivatives. The relationship of the structure and performance of POM-based nanostructures in electrocatalytic applications is also discussed. There still exist challenges and opportunities to meet the requirements of electrocatalytic and energy applications, including but not limited to the following items.

(1) In the context of catalysis and energy-related applications of POMs, one of the key challenges to continue research is anchoring POMs to suitable substrates or constructing POM-based composites. Stability is a crucial factor in the application of POMs as electrode materials. Most POMs are water-soluble and have relatively large molecular sizes. How to control the conditions to make POM particles well dispersed and fixed on the support bracket, or coated POMs with other materials, will effectively improve the stability, which deserves further study.

(2) The unique physical and chemical properties of POMs make them show significant advantages in electrocatalytic applications. To fully understand the changes in fine dynamic structure, the evolution of active sites, and key reaction intermediates during the reaction of POM-based materials, the challenge is developing more accurate *in situ* electrochemical characterization techniques.

(3) Due to the complexity of POM-based catalysts, exploring the combination of multivariate analysis and machine learning for data analysis to achieve the redesign and optimization of catalysts can accelerate the development of POMs in the field of electrocatalytic and energy.

(4) Although many POM-based materials and their derivatives have been reported as catalysts for electrocatalytic and energy fields, most of the synthesis methods are limited to the laboratory scale due to the complex synthesis process. Therefore, it is very important to develop simple and scalable synthetic routes. At the same time, to achieve industrial applications, it is also necessary to rationally design POM-based materials with high mechanical strength and stability.

## Conflicts of interest

The authors declare no conflict of interest in this manuscript.

## Acknowledgements

The authors greatly acknowledge the financial support from the National Natural Science Foundation of China (22301257, 21072221, 21875247, 21172252).

## References

- 1 T. Muneer, M. Asif and S. Munawwar, Sustainable production of solar electricity with particular reference to the Indian economy, *Renewable Sustainable Energy Rev.*, 2005, **9**, 444–473.
- 2 N. Armaroli and V. Balzani, The hydrogen issue, *ChemSusChem*, 2011, **4**, 21–36.
- 3 X. Tian, C. An and Z. Chen, The role of clean energy in achieving decarbonization of electricity generation, transportation, and heating sectors by 2050: A meta-analysis review, *Renewable Sustainable Energy Rev.*, 2023, **182**, 113404.
- 4 S. E. Hosseini and M. A. Wahid, Hydrogen production from renewable and sustainable energy resources: Promising green energy carrier for clean development, *Renewable Sustainable Energy Rev.*, 2016, **57**, 850–866.
- 5 W. Zhang, Z. Jin and Z. Chen, Rational-Designed Principles for Electrochemical and Photoelectrochemical Upgrading of  $\text{CO}_2$  to Value-Added Chemicals, *Adv. Sci.*, 2022, **9**, 2105204.
- 6 R. Shi, X. Zhang, G. I. Waterhouse, Y. Zhao and T. Zhang, The journey toward low temperature, low pressure catalytic nitrogen fixation, *Adv. Energy Mater.*, 2020, **10**, 2000659.
- 7 Y. Yang, Y. Han, W. Jiang, Y. Zhang, Y. Xu and A. M. Ahmed, Application of the supercapacitor for energy storage in China: role and strategy, *Appl. Sci.*, 2021, **12**, 354.
- 8 K. Turcheniuk, D. Bondarev, G. G. Amatucci and G. Yushin, Battery materials for low-cost electric transportation, *Mater. Today*, 2021, **42**, 57–72.
- 9 A. Kraysberg and Y. Ein-Eli, The impact of nano-scaled materials on advanced metal-air battery systems, *Nano Energy*, 2013, **2**, 468–480.
- 10 K. Jiao, J. Xuan, Q. Du, Z. Bao, B. Xie, B. Wang, Y. Zhao, L. Fan, H. Wang and Z. Hou, Designing the next generation of proton-exchange membrane fuel cells, *Nature*, 2021, **595**, 361–369.
- 11 S. Yuan, X. Duan, J. Liu, Y. Ye, F. Lv, T. Liu, Q. Wang and X. Zhang, Recent progress on transition metal oxides as advanced materials for energy conversion and storage, *Energy Storage Mater.*, 2021, **42**, 317–369.
- 12 Y. Zhang, M. X. Li, Q. Hao, F. Su, Z. M. Zhu, J. S. Li, X. J. Sang, C. S. Wang and L. C. Zhang, Two new estertin modified tungstosilicates: synthesis, catalytic activity and photoelectrochemical property, *Dalton Trans.*, 2020, **49**, 7234–7244.





- 13 S.-S. Wang and G.-Y. Yang, Recent advances in polyoxometalate-catalyzed reactions, *Chem. Rev.*, 2015, **115**, 4893–4962.
- 14 L. Guo, L. He, Q. Zhuang, B. Li, C. Wang, Y. Lv, J. Chu and Y. F. Song, Recent Advances in Confining Polyoxometalates and the Applications, *Small*, 2023, 2207315.
- 15 Y. Zhang, J. Liu, S.-L. Li, Z.-M. Su and Y.-Q. Lan, Polyoxometalate-based materials for sustainable and clean energy conversion and storage, *EnergyChem*, 2019, **1**, 100021.
- 16 N. Li, J. Liu, B. X. Dong and Y. Q. Lan, Polyoxometalate-based compounds for photo-and electrocatalytic applications, *Angew. Chem., Int. Ed.*, 2020, **59**, 20779–20793.
- 17 Z. Zeb, Y. Huang, L. Chen, W. Zhou, M. Liao, Y. Jiang, H. Li, L. Wang, L. Wang, H. Wang, T. Wei, D. Zang, Z. Fan and Y. Wei, Comprehensive overview of polyoxometalates for electrocatalytic hydrogen evolution reaction, *Coord. Chem. Rev.*, 2023, **482**, 215058.
- 18 Z.-H. Wang, X.-F. Wang, Z. Tan and X.-Z. Song, Polyoxometalate/metal-organic framework hybrids and their derivatives for hydrogen and oxygen evolution electrocatalysis, *Mater. Today Energy*, 2021, **19**, 100618.
- 19 J. Du, Y.-Y. Ma, H. Tan, Z.-H. Kang and Y. Li, Progress of electrochemical CO<sub>2</sub> reduction reactions over polyoxometalate-based materials, *Chin. J. Catal.*, 2021, **42**, 920–937.
- 20 D. Zang and H. Wang, Polyoxometalate-based nanostructures for electrocatalytic and photocatalytic CO<sub>2</sub> reduction, *Polyoxometalates*, 2022, **1**, 9140006.
- 21 R. Liu and C. Streb, Polyoxometalate-single atom catalysts (POM-SACs) in energy research and catalysis, *Adv. Energy Mater.*, 2021, **11**, 2101120.
- 22 Y. Ji, L. Huang, J. Hu, C. Streb and Y.-F. Song, Polyoxometalate-functionalized nanocarbon materials for energy conversion, energy storage and sensor systems, *Energy Environ. Sci.*, 2015, **8**, 776–789.
- 23 Q. Li, L. Zhang, J. Dai, H. Tang, Q. Li, H. Xue and H. Pang, Polyoxometalate-based materials for advanced electrochemical energy conversion and storage, *Chem. Eng. J.*, 2018, **351**, 441–461.
- 24 B. Huang, D.-H. Yang and B.-H. Han, Application of polyoxometalate derivatives in rechargeable batteries, *J. Mater. Chem. A*, 2020, **8**, 4593–4628.
- 25 D. Wang, L. Liu, J. Jiang, L. Chen and J. Zhao, Polyoxometalate-based composite materials in electrochemistry: state-of-the-art progress and future outlook, *Nanoscale*, 2020, **12**, 5705–5718.
- 26 M. R. Horn, A. Singh, S. Alomari, S. Goberna-Ferrón, R. Benages-Vilau, N. Chodankar, N. Motta, K. K. Ostrikov, J. MacLeod, P. Sonar, P. Gomez-Romero and D. Dubal, Polyoxometalates (POMs): from electroactive clusters to energy materials, *Energy Environ. Sci.*, 2021, **14**, 1652–1700.
- 27 B. Fabre, C. Falaise and E. Cadot, Polyoxometalates-Functionalized Electrodes for (Photo) Electrocatalytic Applications: Recent Advances and Prospects, *ACS Catal.*, 2022, **12**, 12055–12091.
- 28 Q. Zhang, F. Li and L. Xu, Application of polyoxometalates in third-generation solar cells, *Polyoxometalates*, 2023, **2**, 9140018.
- 29 J. F. Keggin, Structure of the molecule of 12-phosphotungstic acid, *Nature*, 1933, **131**, 908–909.
- 30 D. Cheng, K. Li, H. Zang and J. Chen, Recent Advances on Polyoxometalate-Based Ion-Conducting Electrolytes for Energy-Related Devices, *Energy Environ. Mater.*, 2023, **6**, e12341.
- 31 X. Huang, Z. Wang, T. Wang, W. Wang and P. He, Fe-substituted Polyoxometalate-based Spherical Assemblies as Catalysts for Olefin Epoxidation, *Chem. Res. Chin. Univ.*, 2023, **39**, 660–665.
- 32 P. He, B. Xu, X. Xu, L. Song and X. Wang, Surfactant encapsulated palladium-polyoxometalates: controlled assembly and their application as single-atom catalysts, *Chem. Sci.*, 2016, **7**, 1011–1015.
- 33 S. Roy, D. C. Crans and T. N. Parac-Vogt, Polyoxometalates in catalysis, biology, energy and materials science, *Front. Chem.*, 2019, **7**, 646.
- 34 J. Liu, S. Nie, L. Wu and X. Wang, High-entropy Metal Oxide-polyoxometalate-palladium Sub-1 nm Nanowires for Semi-hydrogenation Reaction of Alkynes, *Chem. Res. Chin. Univ.*, 2023, **39**, 624–629.
- 35 J. H. Kruse, M. Langer, I. Romanenko, I. Trentin, D. Hernández-Castillo, L. González, F. H. Schacher and C. Streb, Polyoxometalate-Soft Matter Composite Materials: Design Strategies, Applications, and Future Directions, *Adv. Funct. Mater.*, 2022, **32**, 2208428.
- 36 J. Liu, Y. Li, Z. Chen, N. Liu, L. Zheng, W. Shi and X. Wang, Polyoxometalate Cluster-Incorporated High Entropy Oxide Sub-1 nm Nanowires, *J. Am. Chem. Soc.*, 2022, **144**, 23191–23197.
- 37 M. I. S. Verissimo, D. V. Evtuguin and M. T. S. R. Gomes, Polyoxometalate Functionalized Sensors: A Review, *Front. Chem.*, 2022, **10**, 840657.
- 38 P. Song and T. Wang, Application of Polyoxometalates in Chemiresistive Gas Sensors: A Review, *ACS Sens.*, 2022, **7**, 3634–3643.
- 39 H. Li, S. Pang, S. Wu, X. Feng, K. Müllen and C. Bubeck, Layer-by-Layer Assembly and UV Photoreduction of Graphene-Polyoxometalate Composite Films for Electronics, *J. Am. Chem. Soc.*, 2011, **133**, 9423–9429.
- 40 L. Cheng, C. Liang, W. Liu, Y. Wang, B. Chen, H. Zhang, Y. Wang, Z. Chai and S. Wang, Three-Dimensional Polycatenation of a Uranium-Based Metal-Organic Cage: Structural Complexity and Radiation Detection, *J. Am. Chem. Soc.*, 2020, **142**, 16218–16222.
- 41 H. Zhang, A. Li, K. Li, Z. Wang, X. Xu, Y. Wang, M. V. Sheridan, H.-S. Hu, C. Xu, E. V. Alekseev, Z. Zhang, P. Yan, K. Cao, Z. Chai, T. E. Albrecht-Schönzart and S. Wang, Ultrafiltration separation of Am(VI)-polyoxometalate from lanthanides, *Nature*, 2023, **616**, 482–487.
- 42 J. Gautam, Y. Liu, J. Gu, Z. Ma, B. Dahal, A. Nabi Chishti, L. Ni, G. Diao and Y. Wei, Three-dimensional nano assembly of nickel cobalt sulphide/polyaniline@polyoxometalate/



- reduced graphene oxide hybrid with superior lithium storage and electrocatalytic properties for hydrogen evolution reaction, *J. Colloid Interface Sci.*, 2022, **614**, 642–654.
- 43 Y. Lu, C. Yue, Y. Li, W. Bao, X. Guo, W. Yang, Z. Liu, P. Jiang, W. Yan, S. Liu, Y. Pan and Y. Liu, Atomically dispersed Ni on Mo<sub>2</sub>C embedded in N, P co-doped carbon derived from polyoxometalate supramolecule for high-efficiency hydrogen evolution electrocatalysis, *Appl. Catal., B*, 2021, **296**, 120336.
- 44 Q.-Q. Pan, C.-Y. Xu, X. Li, J.-F. Zhang, X.-L. Hu, Y. Geng and Z.-M. Su, Porous Ni-Mo bimetallic hybrid electrocatalyst by intermolecular forces in precursors for enhanced hydrogen generation, *Chem. Eng. J.*, 2021, **405**, 126962.
- 45 Z. Wei, J. Pang, Y. Ji, X. Yang, Y. Liu, L. Ren and Y. Zhang, Ultrafine multi-metallic carbide nanocrystals encased in a carbon matrix as durable electrocatalysts towards effective alkaline hydrogen evolution reaction, *Mater. Adv.*, 2021, **2**, 336–344.
- 46 L. Zhang, S. Li, C. J. Gómez-García, H. Ma, C. Zhang, H. Pang and B. Li, Two Novel Polyoxometalate-Encapsulated Metal-Organic Nanotube Frameworks as Stable and Highly Efficient Electrocatalysts for Hydrogen Evolution Reaction, *ACS Appl. Mater. Interfaces*, 2018, **10**, 31498–31504.
- 47 C. Wang, L. Li, H. Wang, T. Qu, J. Tian, D. Wang and Z. Kang, Tunable Ni/Fe-Mo carbide catalyst with high activity toward hydrogen evolution reaction, *Can. J. Chem. Eng.*, 2020, **98**, 1784–1793.
- 48 C. Huang, X. Miao, C. Pi, B. Gao, X. Zhang, P. Qin, K. Huo, X. Peng and P. K. Chu, Mo<sub>2</sub>C/VC heterojunction embedded in graphitic carbon network: An advanced electrocatalyst for hydrogen evolution, *Nano Energy*, 2019, **60**, 520–526.
- 49 Y. Zhang, H. Guo, P. Yuan, K. Pang, B. Cao, X. Wu, L. Zheng and R. Song, Structural evolution of CoMoO<sub>4</sub> to CoOOH by ion electrochemical etching for boosting oxygen evolution reaction, *J. Power Sources*, 2019, **442**, 227252.
- 50 X. Wang, G. Zhang, W. Yin, S. Zheng, Q. Kong, J. Tian and H. Pang, Metal-organic framework-derived phosphide nanomaterials for electrochemical applications, *Carbon Energy*, 2022, **4**, 246–281.
- 51 Y.-J. Tang, Y. Chen, H.-J. Zhu, A. M. Zhang, X.-L. Wang, L.-Z. Dong, S.-L. Li, Q. Xu and Y.-Q. Lan, Solid-phase hot-pressing synthesis of POMOFs on carbon cloth and derived phosphides for all pH value hydrogen evolution, *J. Mater. Chem. A*, 2018, **6**, 21969–21977.
- 52 J. Xiao, Z. Zhang, Y. Zhang, Q. Lv, F. Jing, K. Chi and S. Wang, Large-scale printing synthesis of transition metal phosphides encapsulated in N, P co-doped carbon as highly efficient hydrogen evolution cathodes, *Nano Energy*, 2018, **51**, 223–230.
- 53 Y. Zhang, H. Guo, X. Li, J. Du, W. Ren and R. Song, A 3D multi-interface structure of coral-like Fe-Mo-S/Ni<sub>3</sub>S<sub>2</sub>@NF using for high-efficiency and stable overall water splitting, *Chem. Eng. J.*, 2021, **404**, 126483.
- 54 S. Yang, M. Wang, Y. Zhang, P. He, W. Cong, C. Wang, Q. Yang, X. Liu, T. Wang, X. Zhang and J. Zhou, Single-Molecule Confinement Induced Intrinsic Multi-Electron Redox-Activity to Enhance Supercapacitor Performance, *Energy Environ. Mater.*, 2023, **6**, e12396.
- 55 F. Sun, C. Yue, J. Wang, Y. Liu, W. Bao, N. Liu, Y. Tuo and Y. Lu, Lacunary polyoxometalate oriented construction of dispersed Ni<sub>3</sub>S<sub>2</sub> confined in WO<sub>3</sub> for electrocatalytic water splitting, *J. Colloid Interface Sci.*, 2023, **645**, 188–199.
- 56 C. Freire, D. M. Fernandes, M. Nunes and M. Araújo, Polyoxometalate-based modified electrodes for electrocatalysis: from molecule sensing to renewable energy-related applications, *Adv. Electrode Mater.*, 2017, 149–212.
- 57 M. Yang, X. Wang, C. J. Gómez-García, Z. Jin, J. Xin, X. Cao, H. Ma, H. Pang, L. Tan and G. Yang, Efficient Electron Transfer from an Electron-Reservoir Polyoxometalate to Dual-Metal-Site Metal-Organic Frameworks for Highly Efficient Electroreduction of Nitrogen, *Adv. Funct. Mater.*, 2023, **33**, 2214495.
- 58 X. Hui, L. Wang, Z. Yao, L. Hao and Z. Sun, Recent progress of photocatalysts based on tungsten and related metals for nitrogen reduction to ammonia, *Front. Chem.*, 2022, **10**, 978078.
- 59 G. M. Bosch, A. Sarapulova and S. Dsoke, Study of Polyoxometalates as Electrode Materials for Lithium-Ion Batteries: Thermal Stability Paves the Way to Improved Cycle Stability, *ChemElectroChem*, 2020, **8**, 656–664.
- 60 Y.-Q. Jiao, H.-J. Yan, C.-G. Tian and H.-G. Fu, Structure engineering and electronic modulation of transition metal interstitial compounds for electrocatalytic water splitting, *Acc. Mater. Res.*, 2022, **4**, 42–56.
- 61 Y. Zhang, H. Guo, J. Ren, X. Li, W. Ren and R. Song, MoO<sub>3</sub> crystal facets modulation by doping heteroatom Fe from polyoxometalate for quasi-industrial oxygen evolution reaction, *Appl. Catal., B*, 2021, **298**, 120582.
- 62 J. Liu, W. Shi, B. Ni, Y. Yang, S. Li, J. Zhuang and X. Wang, Incorporation of clusters within inorganic materials through their addition during nucleation steps, *Nat. Chem.*, 2019, **11**, 839–845.
- 63 M. Dresselhaus and I. Thomas, Alternative energy technologies, *Nature*, 2001, **414**, 332–337.
- 64 S. Chu and A. Majumdar, Opportunities and challenges for a sustainable energy future, *Nature*, 2012, **488**, 294–303.
- 65 G. Zhao, K. Rui, S. X. Dou and W. Sun, Heterostructures for Electrochemical Hydrogen Evolution Reaction: A Review, *Adv. Funct. Mater.*, 2018, **28**, 1803291.
- 66 X. Li, L. L. Zhao, J. Y. Yu, X. Y. Liu, X. L. Zhang, H. Liu and W. J. Zhou, Water Splitting: From Electrode to Green Energy System, *Nano-Micro Lett.*, 2020, **12**, 131.
- 67 Z. Zhang, Y. Qin, M. Dou, J. Ji and F. Wang, One-step conversion from Ni/Fe polyphthalocyanine to N-doped carbon supported Ni-Fe nanoparticles for highly efficient water splitting, *Nano Energy*, 2016, **30**, 426–433.
- 68 T. Sun, W. Zang, J. Sun, C. Li, J. Fan, E. Liu and J. Wang, SACs on Non-Carbon Substrates: Can They Outperform for Water Splitting?, *Adv. Funct. Mater.*, 2023, 2301526.
- 69 S. S. Wang and G. Y. Yang, Recent advances in polyoxometalate-catalyzed reactions, *Chem. Rev.*, 2015, **115**, 4893–4962.



- 70 B. Keita, U. Kortz, L. R. B. Holzle, S. Brown and L. Nadjo, Efficient hydrogen-evolving cathodes based on proton and electron reservoir behaviors of the phosphotungstate  $[H_7P_8W_{48}O_{184}]_{33}$ -and the Co (II)-containing silicotungstates  $[Co_6(H_2O)_{30}\{Co_9C_{12}(OH)_3(H_2O)_9(\beta-SiW_8O_{31})_3\}]_5$ -and  $[Co_3(B-\beta-SiW_9O_{33}(OH))(B-\beta-SiW_8O_{29}OH)_2]_{22}$ , *Langmuir*, 2007, **23**, 9531–9534.
- 71 M. D. Symes and L. Cronin, Decoupling hydrogen and oxygen evolution during electrolytic water splitting using an electron-coupled-proton buffer, *Nat. Chem.*, 2013, **5**, 403–409.
- 72 C. Wang, M. Zhou, Y. Ma, H. Tan, Y. Wang and Y. Li, Hybridized Polyoxometalate-Based Metal–Organic Framework with Ketjenblack for the Nonenzymatic Detection of H<sub>2</sub>O<sub>2</sub>, *Chem.–Asian J.*, 2018, **13**, 2054–2059.
- 73 Y. Zhang, Y. Liu, D. Wang, J. Liu, J. Zhao and L. Chen, State-of-the-art advances in the syntheses, structures, and applications of polyoxometalate-based metal–organic frameworks, *Polyoxometalates*, 2023, **2**, 9140017.
- 74 M. I. Verissimo, D. V. Evtuguin and M. Gomes, Polyoxometalate functionalized sensors: a review, *Front. Chem.*, 2022, **10**, 840657.
- 75 N. Kawasaki, H. Wang, R. Nakanishi, S. Hamanaka, R. Kitaura, H. Shinohara, T. Yokoyama, H. Yoshikawa and K. Awaga, Nanohybridization of polyoxometalate clusters and single-wall carbon nanotubes: applications in molecular cluster batteries, *Angew. Chem., Int. Ed.*, 2011, **123**, 3533–3536.
- 76 D. Pakulski, A. Gorczyński, D. Brykczynska, V. Montes-García, W. Czepa, I. Janica, M. Bielejewski, M. Kubicki, V. Patroniak and P. Samori, New Anderson-Based Polyoxometalate Covalent Organic Frameworks as Electrodes for Energy Storage Boosted Through Keto-Enol Tautomerization, *Angew. Chem., Int. Ed.*, 2023, e202305239.
- 77 B. Nohra, H. El Moll, L. M. Rodriguez Albelo, P. Mialane, J. Marrot, C. Mellot-Draznieks, M. O’Keeffe, R. Ngo Biboum, J. Lemaire, B. Keita, L. Nadjo and A. Dolbecq, Polyoxometalate-based metal organic frameworks (POMOFs): structural trends, energetics, and high electrocatalytic efficiency for hydrogen evolution reaction, *J. Am. Chem. Soc.*, 2011, **133**, 13363–13374.
- 78 J. S. Qin, D. Y. Du, W. Guan, X. J. Bo, Y. F. Li, L. P. Guo, Z. M. Su, Y. Y. Wang, Y. Q. Lan and H. C. Zhou, Ultrastable Polymolybdate-Based Metal–Organic Frameworks as Highly Active Electrocatalysts for Hydrogen Generation from Water, *J. Am. Chem. Soc.*, 2015, **137**, 7169–7177.
- 79 R. Liu, G. Zhang, H. Cao, S. Zhang, Y. Xie, A. Haider, U. Kortz, B. Chen, N. S. Dalal, Y. Zhao, L. Zhi, C.-X. Wu, L.-K. Yan, Z. Su and B. Keitag, Enhanced proton and electron reservoir abilities of polyoxometalate grafted on graphene for high-performance hydrogen evolution, *Energy Environ. Sci.*, 2016, **9**, 1012–1023.
- 80 D. M. Fernandes, M. P. Araujo, A. Haider, A. S. Mougharbel, A. J. Fernandes, U. Kortz and C. Freire, Polyoxometalate-graphene Electrocatalysts for the Hydrogen Evolution Reaction, *ChemElectroChem*, 2018, **5**, 273–283.
- 81 D. Zang, Y. Huang, Q. Li, Y. Tang and Y. Wei, Cu dendrites induced by the Anderson-type polyoxometalate NiMo<sub>6</sub>O<sub>24</sub> as a promising electrocatalyst for enhanced hydrogen evolution, *Appl. Catal., B*, 2019, **249**, 163–171.
- 82 M. Blasco-Ahicart, J. Soriano-López and J. R. Galán-Mascarós, Conducting organic polymer electrodes with embedded polyoxometalate catalysts for water splitting, *ChemElectroChem*, 2017, **4**, 3296–3301.
- 83 G. Y. Lee, I. Kim, J. Lim, M. Y. Yang, D. S. Choi, Y. Gu, Y. Oh, S. H. Kang, Y. S. Nam and S. O. Kim, Spontaneous linker-free binding of polyoxometalates on nitrogen-doped carbon nanotubes for efficient water oxidation, *J. Mater. Chem. A*, 2017, **5**, 1941–1947.
- 84 Y. Zhang, J. Liu, S. Li, Z. Su and Y. Lan, Polyoxometalate-based materials for sustainable and clean energy conversion and storage, *EnergyChem*, 2019, **1**, 100021.
- 85 A. R. Howells, A. Sankarraj and C. Shannon, A diruthenium-substituted polyoxometalate as an electrocatalyst for oxygen generation, *J. Am. Chem. Soc.*, 2004, **126**, 12258–12259.
- 86 F. M. Toma, A. Sartorel, M. Iurlo, M. Carraro, P. Parisse, C. Maccato, S. Rapino, B. R. Gonzalez, H. Amenitsch and T. Da Ros, Efficient water oxidation at carbon nanotube-polyoxometalate electrocatalytic interfaces, *Nat. Chem.*, 2010, **2**, 826–831.
- 87 W. Luo, J. Hu, H. Diao, B. Schwarz, C. Streb and Y. Song, Stabile Polyoxometallat-Nickelschaum-Elektroden für elektrochemische Sauerstoffentwicklung im alkalischen Milieu, *Angew. Chem., Int. Ed.*, 2017, **129**, 5023–5026.
- 88 M. Blasco-Ahicart, J. Soriano-López, J. J. Carbó, J. M. Poblet and J.-R. Galan-Mascaros, Polyoxometalate electrocatalysts based on earth-abundant metals for efficient water oxidation in acidic media, *Nat. Chem.*, 2018, **10**, 24–30.
- 89 M. Martin-Sabi, J. Soriano-Lopez, R. S. Winter, J. J. Chen, L. Vila-Nadal, D. L. Long, J. R. Galan-Mascaros and L. Cronin, Redox tuning the Weakley-type polyoxometalate archetype for the oxygen evolution reaction, *Nat. Catal.*, 2018, **1**, 208–213.
- 90 J. Gautam, Y. Liu, J. Gu, Z. Y. Ma, J. J. Zha, B. Dahal, L. N. Zhang, A. N. Chishti, L. B. Ni, G. W. Diao and Y. G. Wei, Fabrication of Polyoxometalate Anchored Zinc Cobalt Sulfide Nanowires as a Remarkable Bifunctional Electrocatalyst for Overall Water Splitting, *Adv. Funct. Mater.*, 2021, **31**, 2106147.
- 91 S. H. Talib, Z. Lu, X. Yu, K. Ahmad, B. Bashir, Z. Yang and J. Li, Theoretical Inspection of M<sub>1</sub>/PMA Single-Atom Electrocatalyst: Ultra-High Performance for Water Splitting (HER/OER) and Oxygen Reduction Reactions (OER), *ACS Catal.*, 2021, **11**, 8929–8941.
- 92 J. Wang, F. Xu, H. Jin, Y. Chen and Y. Wang, Non-noble metal-based carbon composites in hydrogen evolution reaction: fundamentals to applications, *Adv. Mater.*, 2017, **29**, 1605838.
- 93 J. Deng, P. Ren, D. Deng and X. Bao, Enhanced electron penetration through an ultrathin graphene layer for highly efficient catalysis of the hydrogen evolution reaction, *Angew. Chem. Int. Ed.*, 2015, **54**, 2100–2104.
- 94 Y. Liu, G. Yu, G. D. Li, Y. Sun, T. Asefa, W. Chen and X. Zou, Coupling Mo<sub>2</sub>C with nitrogen-rich nanocarbon





- leads to efficient hydrogen-evolution electrocatalytic sites, *Angew. Chem., Int. Ed.*, 2015, **127**, 10902–10907.
- 95 G. Yan, C. Wu, H. Tan, X. Feng, L. Yan, H. Zang and Y. Li, N-Carbon coated P-W<sub>2</sub>C composite as efficient electrocatalyst for hydrogen evolution reactions over the whole pH range, *J. Mater. Chem. A*, 2017, **5**, 765–772.
- 96 L. N. Zhang, S. H. Li, H. Q. Tan, S. U. Khan, Y. Y. Ma, H. Y. Zang, Y. H. Wang and Y. G. Li, MoP/Mo<sub>2</sub>C@C: A New Combination of Electrocatalysts for Highly Efficient Hydrogen Evolution over the Entire pH Range, *ACS Appl. Mater. Interfaces*, 2017, **9**, 16270–16279.
- 97 Y. Ma, C. Wu, X. Feng, H. Tan, L. Yan, Y. Liu, Z. Kang, E. Wang and Y. Li, Highly efficient hydrogen evolution from seawater by a low-cost and stable CoMoP@C electrocatalyst superior to Pt/C, *Energy Environ. Sci.*, 2017, **10**, 788–798.
- 98 F. Y. Yu, Y. Gao, Z. L. Lang, Y. Y. Ma, L. Y. Yin, J. Du, H. Q. Tan, Y. H. Wang and Y. G. Li, Electrocatalytic performance of ultrasmall Mo<sub>2</sub>C affected by different transition metal dopants in hydrogen evolution reaction, *Nanoscale*, 2018, **10**, 6080–6087.
- 99 Y. Gao, Z. L. Lang, F. Y. Yu, H. Q. Tan, G. Yan, Y. H. Wang, Y. Y. Ma and Y. G. Li, A Co<sub>2</sub>P/WC Nano-Heterojunction Covered with N-Doped Carbon as Highly Efficient Electrocatalyst for Hydrogen Evolution Reaction, *ChemSusChem*, 2018, **11**, 1082–1091.
- 100 X. Yang, X. Feng, H. Tan, H. Zang, X. Wang, Y. Wang, E. Wang and Y. Li, N-Doped graphene-coated molybdenum carbide nanoparticles as highly efficient electrocatalysts for the hydrogen evolution reaction, *J. Mater. Chem. A*, 2016, **4**, 3947–3954.
- 101 Y.-Y. Ma, Z.-L. Lang, L.-K. Yan, Y.-H. Wang, H.-Q. Tan, K. Feng, Y.-J. Xia, J. Zhong, Y. Liu, Z.-H. Kang and Y.-G. Li, Highly efficient hydrogen evolution triggered by a multi-interfacial Ni/WC hybrid electrocatalyst, *Energy Environ. Sci.*, 2018, **11**, 2114–2123.
- 102 G. Yan, X. J. Feng, S. U. Khan, L. G. Xiao, W. G. Xi, H. Q. Tan, Y. Y. Ma, L. N. Zhang and Y. G. Li, Polyoxometalate and Resin-Derived P-Doped Mo<sub>2</sub>C@N-Doped Carbon as a Highly Efficient Hydrogen-Evolution Reaction Catalyst at All pH Values, *Chem. – Asian J.*, 2018, **13**, 158–163.
- 103 Y. Huang, X. Song, J. Deng, C. Zha, W. Huang, Y. Wu and Y. Li, Ultra-dispersed molybdenum phosphide and phosphosulfide nanoparticles on hierarchical carbonaceous scaffolds for hydrogen evolution electrocatalysis, *Appl. Catal., B*, 2019, **245**, 656–661.
- 104 J. S. Li, Y. Wang, C. H. Liu, S. L. Li, Y. G. Wang, L. Z. Dong, Z. H. Dai, Y. F. Li and Y. Q. Lan, Coupled molybdenum carbide and reduced graphene oxide electrocatalysts for efficient hydrogen evolution, *Nat. Commun.*, 2016, **7**, 11204.
- 105 X. L. Wang, Y. J. Tang, W. Huang, C. H. Liu, L. Z. Dong, S. L. Li and Y. Q. Lan, Efficient Electrocatalyst for the Hydrogen Evolution Reaction Derived from Polyoxotungstate/Polypyrrole/Graphene, *ChemSusChem*, 2017, **10**, 2402–2407.
- 106 Y. Huang, J. Ge, J. Hu, J. Zhang, J. Hao and Y. Wei, Nitrogen-Doped Porous Molybdenum Carbide and Phosphide Hybrids on a Carbon Matrix as Highly Effective Electrocatalysts for the Hydrogen Evolution Reaction, *Adv. Energy Mater.*, 2018, **8**, 1701601.
- 107 Y. Huang, J. Hu, H. Xu, W. Bian, J. Ge, D. Zang, D. Cheng, Y. Lv, C. Zhang, J. Gu and Y. Wei, Fine Tuning Electronic Structure of Catalysts through Atomic Engineering for Enhanced Hydrogen Evolution, *Adv. Energy Mater.*, 2018, **8**, 1800789.
- 108 C. Y. Xu, J. Li, D. Sun, X. Li, X. L. Wang and Z. M. Su, Co/WC@NC electrocatalysts derived from polyoxometalates (POM) for efficient hydrogen evolution, *Nanotechnology*, 2021, **32**, 375602.
- 109 H. J. Yan, C. G. Tian, L. Wang, A. P. Wu, M. C. Meng, L. Zhao and H. G. Fu, Phosphorus-modified tungsten nitride/reduced graphene oxide as a high-performance, non-noble-metal electrocatalyst for the hydrogen evolution reaction, *Angew. Chem., Int. Ed.*, 2015, **54**, 6325–6329.
- 110 X. B. Han, X. Y. Tang, Y. Lin, E. Gracia-Espino, S. G. Liu, H. W. Liang, G. Z. Hu, X. J. Zhao, H. G. Liao, Y. Z. Tan, T. Wagberg, S. Y. Xie and L. S. Zheng, Ultrasmall Abundant Metal-Based Clusters as Oxygen-Evolving Catalysts, *J. Am. Chem. Soc.*, 2019, **141**, 232–239.
- 111 N. C. S. Selvam, L. Du, B. Y. Xia, P. J. Yoo and B. You, Reconstructed Water Oxidation Electrocatalysts: The Impact of Surface Dynamics on Intrinsic Activities, *Adv. Funct. Mater.*, 2020, **31**, 2008190.
- 112 F. C. Shen, S. Sun, Z. Xin, S. Li, L. Dong, Q. Huang, Y. Wang, J. Liu and Y. Lan, Hierarchically phosphorus doped bimetallic nitrides arrays with unique interfaces for efficient water splitting, *Appl. Catal., B*, 2019, **243**, 470–480.
- 113 Z. Kou, Y. Yu, X. Liu, X. Gao, L. Zheng, H. Zou, Y. Pang, Z. Wang, Z. Pan, J. He, S. J. Pennycook and J. Wang, Potential-Dependent Phase Transition and Mo-Enriched Surface Reconstruction of  $\gamma$ -CoOOH in a Heterostructured Co-Mo<sub>2</sub>C Precatalyst Enable Water Oxidation, *ACS Catal.*, 2020, **10**, 4411–4419.
- 114 J. Zhang, Q. Y. Zhang and X. L. Feng, Support and Interface Effects in Water-Splitting Electrocatalysts, *Adv. Mater.*, 2019, **31**, 1808167.
- 115 R. Subbaraman, D. Tripkovic, D. Strmcnik, K.-C. Chang, M. Uchimura, A. P. Paulikas, V. Stamenkovic and N. M. Markovic, Enhancing hydrogen evolution activity in water splitting by tailoring Li<sup>+</sup>-Ni(OH)<sub>2</sub>-Pt interfaces, *Science*, 2011, **334**, 1256–1260.
- 116 N. Danilovic, R. Subbaraman, D. Strmcnik, K. C. Chang, A. Paulikas, V. Stamenkovic and N. M. Markovic, Enhancing the alkaline hydrogen evolution reaction activity through the bifunctionality of Ni(OH)<sub>2</sub>/metal catalysts, *Angew. Chem., Int. Ed.*, 2012, **124**, 12663–12666.
- 117 Z. Zhuang, S. A. Giles, J. Zheng, G. R. Jenness, S. Caratzoulas, D. G. Vlachos and Y. Yan, Nickel supported on nitrogen-doped carbon nanotubes as hydrogen oxidation reaction catalyst in alkaline electrolyte, *Nat. Commun.*, 2016, **7**, 1–8.
- 118 F. Yu, Z. Lang, L. Yin, K. Feng, Y. Xia, H. Tan, H. Zhu, J. Zhong, Z. Kang and Y. Li, Pt-O bond as an active site



- superior to Pt<sup>0</sup> in hydrogen evolution reaction, *Nat. Commun.*, 2020, **11**, 1–7.
- 119 L. An, J. Feng, Y. Zhang, R. Wang, H. Liu, G. Wang, F. Cheng and P. Xi, Epitaxial Heterogeneous Interfaces on N-NiMoO<sub>4</sub>/NiS<sub>2</sub> Nanowires/Nanosheets to Boost Hydrogen and Oxygen Production for Overall Water Splitting, *Adv. Funct. Mater.*, 2019, **29**, 1805298.
- 120 G. Zhao, Y. Jiang, S.-X. Dou, W. Sun and H. Pan, Interface engineering of heterostructured electrocatalysts towards efficient alkaline hydrogen electrocatalysis, *Sci. Bull.*, 2021, **66**, 85–96.
- 121 J. G. Hou, B. Zhang, Z. W. Li, S. Y. Cao, Y. Q. Sun, Y. Z. Wu, Z. M. Gao and L. C. Sun, Vertically aligned oxygenated-CoS<sub>2</sub>-MoS<sub>2</sub> heteronanosheet architecture from polyoxometalate for efficient and stable overall water splitting, *ACS Catal.*, 2018, **8**, 4612–4621.
- 122 Y. Lu, X. Guo, L. Yang, W. Yang, W. Sun, Y. Tuo, Y. Zhou, S. Wang, Y. Pan, W. Yan, D. Sun and Y. Liu, Highly efficient CoMoS heterostructure derived from vertically anchored Co<sub>5</sub>Mo<sub>10</sub> polyoxometalate for electrocatalytic overall water splitting, *Chem. Eng. J.*, 2020, **394**, 124849.
- 123 Y. Hou, H. Pang, J. Xin, H. Ma, B. Li, X. Wang and L. Tan, Multi-Interface-Modulated CoS<sub>2</sub>@MoS<sub>2</sub> Nanoarrays Derived by Predesigned Germanomolybdate Polymer Showing Ultrahighly Electrocatalytic Activity for Hydrogen Evolution Reaction in Wide pH Range, *Adv. Mater. Interfaces*, 2020, **7**, 2000780.
- 124 G. Huang, Z. Xiao, R. Chen and S. Wang, Defect Engineering of Cobalt-Based Materials for Electrocatalytic Water Splitting, *ACS Sustainable Chem. Eng.*, 2018, **6**, 15954–15969.
- 125 D. Yan, Y. Li, J. Huo, R. Chen, L. Dai and S. Wang, Defect chemistry of nonprecious-metal electrocatalysts for oxygen reactions, *Adv. Mater.*, 2017, **29**, 1606459.
- 126 J. Xie, H. Zhang, S. Li, R. Wang, X. Sun, M. Zhou, J. Zhou, X. W. Lou and Y. Xie, Defect-rich MoS<sub>2</sub> ultrathin nanosheets with additional active edge sites for enhanced electrocatalytic hydrogen evolution, *Adv. Mater.*, 2013, **25**, 5807–5813.
- 127 Y. Tang, Y. Wang, X. Wang, S. Li, W. Huang, L. Dong, C. Liu, Y. Li and Y. Lan, Molybdenum Disulfide/Nitrogen-Doped Reduced Graphene Oxide Nanocomposite with Enlarged Interlayer Spacing for Electrocatalytic Hydrogen Evolution, *Adv. Energy Mater.*, 2016, **6**, 1600116.
- 128 J. Tang, Y. Chu, K. Wang, B. Deng, Y. Li and X. Tan, Facile In Situ Synthesis of an Ultrafine and Defect-Rich Co-doped MoS<sub>2</sub> Nanocluster Catalyst for Efficient Hydrogen Evolution Reaction in Alkaline Medium, *ACS Appl. Energy Mater.*, 2021, **4**, 2300–2306.
- 129 S. R. Ede and Z. Luo, Tuning the intrinsic catalytic activities of oxygen-evolution catalysts by doping: a comprehensive review, *J. Mater. Chem. A*, 2021, **9**, 20131–20163.
- 130 Z. F. Huang, J. Wang, Y. Peng, C. Y. Jung, A. Fisher and X. Wang, Design of efficient bifunctional oxygen reduction/evolution electrocatalyst: recent advances and perspectives, *Adv. Energy Mater.*, 2017, **7**, 1700544.
- 131 H. Lin, N. Liu, Z. Shi, Y. Guo, Y. Tang and Q. Gao, Cobalt-Doping in Molybdenum-Carbide Nanowires Toward Efficient Electrocatalytic Hydrogen Evolution, *Adv. Funct. Mater.*, 2016, **26**, 5590–5598.
- 132 B. Huang, D. Yang and B. Han, Application of polyoxometalate derivatives in rechargeable batteries, *J. Mater. Chem. A*, 2020, **8**, 4593–4628.
- 133 Y. C. Huang, Y. H. Sun, X. L. Zheng, T. Aoki, B. Pattengale, J. Huang, X. He, W. Bian, S. Younan, N. Williams, J. Hu, J. X. Ge, N. Pu, X. X. Yan, X. Q. Pan, L. J. Zhang, Y. G. Wei and J. Gu, Atomically engineering activation sites onto metallic 1T-MoS<sub>2</sub> catalysts for enhanced electrochemical hydrogen evolution, *Nat. Commun.*, 2019, **10**, 982.
- 134 G. Eda, T. Fujita, H. Yamaguchi, D. Voiry, M. Chen and M. Chhowalla, Coherent atomic and electronic heterostructures of single-layer MoS<sub>2</sub>, *ACS Nano*, 2012, **6**, 7311–7317.
- 135 Y. Zhang, H. Guo, M. Song, L. Sun and R. Song, Modulation of the morphology and electronic structure of Ni<sub>3</sub>S<sub>2</sub> nano-forests via P and Mo co-doping in polyoxometalates to promote the urea oxidation reaction, *J. Mater. Chem. A*, 2023, **11**, 3584–3593.
- 136 Y. Shi, Y. Zhou, Y. Lou, Z. Chen, H. Xiong and Y. Zhu, Homogeneity of Supported Single-Atom Active Sites Boosting the Selective Catalytic Transformations, *Adv. Sci.*, 2022, **9**, 2201520.
- 137 F.-Y. Yu, Z.-L. Lang, Y.-J. Zhou, K. Feng, H.-Q. Tan, J. Zhong, S.-T. Lee, Z.-H. Kang and Y.-G. Li, Revealing hydrogen evolution performance of single-atom platinum electrocatalyst with polyoxometalate molecular models, *ACS Energy Lett.*, 2021, **6**, 4055–4062.
- 138 S. Niu, J. Yang, H. Qi, Y. Su, Z. Wang, J. Qiu, A. Wang and T. Zhang, Single-atom Pt promoted Mo<sub>2</sub>C for electrochemical hydrogen evolution reaction, *J. Energy Chem.*, 2021, **57**, 371–377.
- 139 S. H. Talib, B. Ali, S. Mohamed, X.-L. Jiang, K. Ahmad, A. Qurashi and J. Li, Computational screening of M<sub>1</sub>/PW<sub>12</sub>O<sub>40</sub> single-atom electrocatalysts for water splitting and oxygen reduction reactions, *J. Mater. Chem. A*, 2023, **11**, 16334–16348.
- 140 P. M. Vitousek, H. A. Mooney, J. Lubchenco and J. M. Melillo, Human domination of Earth's ecosystems, *Science*, 1997, **277**, 494–499.
- 141 X. Wang, X. Lv, G. Zheng and Y. Fu, Room-temperature Electrochemical C1-to-fuel Conversion: Perspectives from Material Engineering and Device Design, *EnergyChem*, 2022, **4**, 100086.
- 142 C. I. Ezugwu, S. Liu, C. Li, S. Zhuiykov, S. Roy and F. Verpoort, Engineering metal-organic frameworks for efficient photocatalytic conversion of CO<sub>2</sub> into solar fuels, *Coord. Chem. Rev.*, 2022, **450**, 214245.
- 143 Z. Sun, N. Talreja, H. Tao, J. Texter, M. Muhler, J. Strunk and J. Chen, Catalysis of carbon dioxide photoreduction on nanosheets: fundamentals and challenges, *Angew. Chem., Int. Ed.*, 2018, **57**, 7610–7627.
- 144 Y. Zhao, L. Zheng, D. Jiang, W. Xia, X. Xu, Y. Yamauchi, J. Ge and J. Tang, Nanoengineering metal-organic framework-based materials for use in electrochemical CO<sub>2</sub> reduction reactions, *Small*, 2021, **17**, 2006590.



- 145 J. Du, Z.-L. Lang, Y.-Y. Ma, H.-Q. Tan, B.-L. Liu, Y.-H. Wang, Z.-H. Kang and Y.-G. Li, Polyoxometalate-based electron transfer modulation for efficient electrocatalytic carbon dioxide reduction, *Chem. Sci.*, 2020, **11**, 3007–3015.
- 146 X. Duan, J. Xu, Z. Wei, J. Ma, S. Guo, S. Wang, H. Liu and S. Dou, Metal-free carbon materials for CO<sub>2</sub> electrochemical reduction, *Adv. Mater.*, 2017, **29**, 1701784.
- 147 Z.-Z. Wu, F.-Y. Gao and M.-R. Gao, Regulating the oxidation state of nanomaterials for electrocatalytic CO<sub>2</sub> reduction, *Energy Environ. Sci.*, 2021, **14**, 1121–1139.
- 148 D. Gao, T. Liu, G. Wang and X. Bao, Structure sensitivity in single-atom catalysis toward CO<sub>2</sub> electroreduction, *ACS Energy Lett.*, 2021, **6**, 713–727.
- 149 J. Gu, W. Chen, G.-G. Shan, G. Li, C. Sun, X.-L. Wang and Z. Su, The roles of polyoxometalates in photocatalytic reduction of carbon dioxide, *Mater. Today, Energy*, 2021, **21**, 100760.
- 150 G. Gao, F. Li, L. Xu, X. Liu and Y. Yang, CO<sub>2</sub> coordination by inorganic polyoxoanion in water, *J. Am. Chem. Soc.*, 2008, **130**, 10838–10839.
- 151 S. H. Szczepankiewicz, C. M. Ippolito, B. P. Santora, T. J. Van de Ven, G. A. Ippolito, L. Fronckowiak, F. Wiatrowski, T. Power and M. Kozik, Interaction of carbon dioxide with transition-metal-substituted heteropolyanions in nonpolar solvents. Spectroscopic evidence for complex formation, *Inorg. Chem.*, 1998, **37**, 4344–4352.
- 152 J. Paul, P. Page, P. Sauers, K. Ertel, C. Pasternak, W. Lin and M. Kozik, *Transition-Metal-Substituted Heteropoly Anions in Nonpolar Solvents—Structures and Interaction with Carbon Dioxide*, Springer US, Boston, MA, 2002, pp. 205–215.
- 153 H. Yang, D. Yang, Y. Zhou and X. Wang, Polyoxometalate Interlayered Zinc–Metallophthalocyanine Molecular Layer Sandwich as Photocoupled Electrocatalytic CO<sub>2</sub> Reduction Catalyst, *J. Am. Chem. Soc.*, 2021, **143**, 13721–13730.
- 154 Y.-R. Wang, Q. Huang, C.-T. He, Y. Chen, J. Liu, F.-C. Shen and Y.-Q. Lan, Oriented electron transmission in polyoxometalate-metalloporphyrin organic framework for highly selective electroreduction of CO<sub>2</sub>, *Nat. Commun.*, 2018, **9**, 4466.
- 155 M. L. Sun, Y. R. Wang, W. W. He, R. L. Zhong, Q. Z. Liu, S. Xu, J. M. Xu, X. L. Han, X. Ge, S. L. Li, Y.-Q. Lan, A. M. Al-Enizi, A. Nafady and S. Ma, Efficient electron transfer from electron-sponge polyoxometalate to single-metal site metal–organic frameworks for highly selective electroreduction of carbon dioxide, *Small*, 2021, **17**, 2100762.
- 156 Q. Huang, Q. Niu, X.-F. Li, J. Liu, S.-N. Sun, L.-Z. Dong, S.-L. Li, Y.-P. Cai and Y.-Q. Lan, Demystifying the roles of single metal site and cluster in CO<sub>2</sub> reduction *via* light and electric dual-responsive polyoxometalate-based metal–organic frameworks, *Sci. Adv.*, 2022, **8**, eadd5598.
- 157 S.-X. Guo, F. Li, L. Chen, D. R. MacFarlane and J. Zhang, Polyoxometalate-promoted electrocatalytic CO<sub>2</sub> reduction at nanostructured silver in dimethylformamide, *ACS Appl. Mater. Interfaces*, 2018, **10**, 12690–12697.
- 158 S. X. Guo, D. R. MacFarlane and J. Zhang, Bioinspired Electrocatalytic CO<sub>2</sub> Reduction by Bovine Serum Albumin-Capped Silver Nanoclusters Mediated by [α-SiW<sub>12</sub>O<sub>40</sub>]<sup>4-</sup>, *ChemSusChem*, 2016, **9**, 80–87.
- 159 D. Zang, Q. Li, G. Dai, M. Zeng, Y. Huang and Y. Wei, Interface engineering of Mo<sub>8</sub>/Cu heterostructures toward highly selective electrochemical reduction of carbon dioxide into acetate, *Appl. Catal., B*, 2021, **281**, 119426.
- 160 M. H. Hasan, T. M. I. Mahlia, M. Mofijur, I. Rizwanul Fattah, F. Handayani, H. C. Ong and A. Silitonga, A comprehensive review on the recent development of ammonia as a renewable energy carrier, *Energies*, 2021, **14**, 3732.
- 161 M. Kitano, Y. Inoue, Y. Yamazaki, F. Hayashi, S. Kanbara, S. Matsuishi, T. Yokoyama, S.-W. Kim, M. Hara and H. Hosono, Ammonia synthesis using a stable electride as an electron donor and reversible hydrogen store, *Nat. Chem.*, 2012, **4**, 934–940.
- 162 G. Qing, R. Ghazfar, S. T. Jackowski, F. Habibzadeh, M. M. Ashtiani, C.-P. Chen, M. R. Smith III and T. W. Hamann, Recent advances and challenges of electrocatalytic N<sub>2</sub> reduction to ammonia, *Chem. Rev.*, 2020, **120**, 5437–5516.
- 163 X. Cui, C. Tang and Q. Zhang, A review of electrocatalytic reduction of dinitrogen to ammonia under ambient conditions, *Adv. Energy Mater.*, 2018, **8**, 1800369.
- 164 N. Cao and G. Zheng, Aqueous electrocatalytic N<sub>2</sub> reduction under ambient conditions, *Nano Res.*, 2018, **11**, 2992–3008.
- 165 G. Lin, Q. Ju, X. Guo, W. Zhao, S. Adimi, J. Ye, Q. Bi, J. Wang, M. Yang and F. Huang, Intrinsic electron localization of metastable MoS<sub>2</sub> boosts electrocatalytic nitrogen reduction to ammonia, *Adv. Mater.*, 2021, **33**, 2007509.
- 166 C. Liu, X. Guo, Z.-F. Huang, J. Li, L. Gan, L. Pan, C. Shi, X. Zhang, G. Yang and J.-J. Zou, Surface defect-regulated PdCu/TiO<sub>2-x</sub> promoting efficient electrocatalytic nitrogen reduction, *Mater. Chem. Front.*, 2022, **6**, 2190–2200.
- 167 Y. Ren, C. Yu, X. Tan, Q. Wei, Z. Wang, L. Ni, L. Wang and J. Qiu, Strategies to activate inert nitrogen molecules for efficient ammonia electrosynthesis: current status, challenges, and perspectives, *Energy Environ. Sci.*, 2022, **15**, 2776–2805.
- 168 Y. Sun, Y. Wang, H. Li, W. Zhang, X.-M. Song, D.-M. Feng, X. Sun, B. Jia, H. Mao and T. Ma, Main group metal elements for ambient-condition electrochemical nitrogen reduction, *J. Energy Chem.*, 2021, **62**, 51–70.
- 169 W. Liao, L. Qi, Y. Wang, J. Qin, G. Liu, S. Liang, H. He and L. Jiang, Interfacial engineering promoting electrosynthesis of ammonia over Mo/phosphotungstic acid with high performance, *Adv. Funct. Mater.*, 2021, **31**, 2009151.
- 170 C. Feng, J. Liu, Q. Li, L. Ji, P. Wu, X. Yuan, H. Hu, H. Y. Jiang and G. Xue, Fabricating Ag/PW<sub>12</sub>/Zr-mTiO<sub>2</sub> Composite via Doping and Interface Engineering: An Efficient Catalyst with Bifunctionality in Photo- and Electro-Driven Nitrogen Reduction Reactions, *Adv. Sustainable Syst.*, 2022, **6**, 2100307.
- 171 L. Gao, F. Wang, M. Yu, F. Wei, J. Qi, S. Lin and D. Xie, A novel phosphotungstic acid-supported single metal atom catalyst with high activity and selectivity for the synthesis





- of  $\text{NH}_3$  from electrochemical  $\text{N}_2$  reduction: a DFT prediction, *J. Mater. Chem. A*, 2019, 7, 19838–19845.
- 172 L. Lin, L. Gao, K. Xie, R. Jiang and S. Lin, Ru–polyoxometalate as a single-atom electrocatalyst for  $\text{N}_2$  reduction to  $\text{NH}_3$  with high selectivity at applied voltage: a perspective from DFT studies, *Phys. Chem. Chem. Phys.*, 2020, 22, 7234–7240.
- 173 S. H. Talib, X. Yu, Z. Lu, K. Ahmad, T. Yang, H. Xiao and J. Li, A polyoxometalate cluster-based single-atom catalyst for  $\text{NH}_3$  synthesis via an enzymatic mechanism, *J. Mater. Chem. A*, 2022, 10, 6165–6177.
- 174 Y. Wang, R.-C. Qin, D. Wang and C.-G. Liu, Reduction of  $\text{N}_2$  to  $\text{NH}_3$  catalyzed by a Keggin-type polyoxometalate-supported dual-atom catalyst, *Inorg. Chem. Front.*, 2022, 9, 845–858.
- 175 L. Lin, F. Wei, R. Jiang, Y. Huang and S. Lin, The role of central heteroatom in electrochemical nitrogen reduction catalyzed by polyoxometalate-supported single-atom catalyst, *Nano Res.*, 2023, 16, 309–317.
- 176 L. Zeng, Z. Qiao, X. Peng, Z. Liu, Z. Li, B. Yang, L. Lei, G. Wu and Y. Hou, Progress in Mo/W-based electrocatalysts for nitrogen reduction to ammonia under ambient conditions, *Chem. Commun.*, 2022, 58, 2096–2111.
- 177 H.-Q. Yin, L.-L. Yang, H. Sun, H. Wang, Y.-J. Wang, M. Zhang, T.-B. Lu and Z.-M. Zhang, W/Mo-polyoxometalate-derived electrocatalyst for high-efficiency nitrogen fixation, *Chin. Chem. Lett.*, 2023, 34, 107337.
- 178 X. Wang, Z. Feng, B. Xiao, J. Zhao, H. Ma, Y. Tian, H. Pang and L. Tan, Polyoxometalate-based metal–organic framework-derived bimetallic hybrid materials for upgraded electrochemical reduction of nitrogen, *Green Chem.*, 2020, 22, 6157–6169.
- 179 C. Wang, M. Yang, X. Wang, H. Ma, Y. Tian, H. Pang, L. Tan and K. Gao, Hierarchical  $\text{CoS}_2/\text{MoS}_2$  flower-like heterostructured arrays derived from polyoxometalates for efficient electrocatalytic nitrogen reduction under ambient conditions, *J. Colloid Interface Sci.*, 2022, 609, 815–824.
- 180 M.-L. Yang, Z.-X. Jin, X.-X. Cao, X.-M. Wang, H.-Y. Ma, H.-J. Pang and G.-X. Yang, Polyoxometalates-derived ternary metal oxides electrocatalyst for  $\text{N}_2$  reduction under ambient conditions, *Tungsten*, 2023, DOI: [10.1007/s42864-023-00206-4](https://doi.org/10.1007/s42864-023-00206-4).
- 181 L. G. H. Staaf, P. Lundgren and P. Enoksson, Present and future supercapacitor carbon electrode materials for improved energy storage used in intelligent wireless sensor systems, *Nano Energy*, 2014, 9, 128–141.
- 182 S. Peng, L. Li, H. B. Wu, S. Madhavi and X. W. D. Lou, Controlled Growth of  $\text{NiMoO}_4$  Nanosheet and Nanorod Arrays on Various Conductive Substrates as Advanced Electrodes for Asymmetric Supercapacitors, *Adv. Energy Mater.*, 2015, 5, 1401172.
- 183 S. Zhang and N. Pan, Supercapacitors performance evaluation, *Adv. Energy Mater.*, 2015, 5, 1401401.
- 184 P. Á. Szilágyi and A. J. Sobrido, Performance and potential of porous carbons derived of electrospun metal–organic frameworks for supercapacitor applications, *J. Energy Chem.*, 2022, 73, 348–353.
- 185 M. Genovese and K. Lian, Polyoxometalate modified pine cone biochar carbon for supercapacitor electrodes, *J. Mater. Chem. A*, 2017, 5, 3939–3947.
- 186 D. Cheng, K. Li, H. Zang and J. Chen, Recent Advances on Polyoxometalate-Based Ion-Conducting Electrolytes for Energy-Related Devices, *Energy Environ. Mater.*, 2022, 6, e12341.
- 187 M. A. Garakani, S. Bellani, V. Pellegrini, R. Oropesa-Nuñez, A. E. D. R. Castillo, S. Abouali, L. Najafi, B. Martín-García, A. Ansaldo, P. Bondavalli, C. Demirci, V. Romano, E. Mantero, L. Marasco, M. Prato, G. Bracciale and F. Bonaccorso, Scalable spray-coated graphene-based electrodes for high-power electrochemical double-layer capacitors operating over a wide range of temperature, *Energy Storage Mater.*, 2021, 34, 1–11.
- 188 Y. Yusran, H. Li, X. Guan, D. Li, L. Tang, M. Xue, Z. Zhuang, Y. Yan, V. Valtchev, S. Qiu and Q. Fang, Exfoliated Mesoporous 2D Covalent Organic Frameworks for High-Rate Electrochemical Double-Layer Capacitors, *Adv. Mater.*, 2020, 32, 1907289.
- 189 L. Wei and G. Yushin, Nanostructured activated carbons from natural precursors for electrical double layer capacitors, *Nano Energy*, 2012, 1, 552–565.
- 190 H.-Y. Chen, R. Al-Oweini, J. Friedl, C. Y. Lee, L. Li, U. Kortz, U. Stimming and M. Srinivasan, A novel SWCNT-polyoxometalate nanohybrid material as an electrode for electrochemical supercapacitors, *Nanoscale*, 2015, 7, 7934–7941.
- 191 M. Wang, Y. Zhang, T. Zhang, Y. Li, M. Cui, X. Cao, Y. Lu, D. Peng, W. Liu, X. Liu, T. Wang and Y. Huang, Confinement of single polyoxometalate clusters in molecular-scale cages for improved flexible solid-state supercapacitors, *Nanoscale*, 2020, 12, 11887–11898.
- 192 P. Yang, J. Xie, L. Wang, X. Chen, F. Wu and Y. Huang, Coaxial Cable-Like Carbon Nanotubes-Based Active Fibers for Highly Capacitive and Stable Supercapacitor, *Adv. Mater. Interfaces*, 2020, 7, 2000949.
- 193 D. Zhou and B.-H. Han, Graphene-Based Nanoporous Materials Assembled by Mediation of Polyoxometalate Nanoparticles, *Adv. Funct. Mater.*, 2010, 20, 2717–2722.
- 194 J. Suárez-Guevara, V. Ruiz and P. Gomez-Romero, Hybrid energy storage: high voltage aqueous supercapacitors based on activated carbon–phosphotungstate hybrid materials, *J. Mater. Chem. A*, 2014, 2, 1014–1021.
- 195 P. Palomino, J. Suarez-Guevara, M. Olivares-Marín, V. Ruiz, D. P. Dubal, P. Gómez-Romero, D. Tonti and E. Enciso, Influence of texture in hybrid carbon-phosphomolybdic acid materials on their performance as electrodes in supercapacitors, *Carbon*, 2017, 111, 74–82.
- 196 C. Hu, E. Zhao, N. Nitta, A. Magasinski, G. Bardichevsky and G. Yushin, Aqueous solutions of acidic ionic liquids for enhanced stability of polyoxometalate-carbon supercapacitor electrodes, *J. Power Sources*, 2016, 326, 569–574.
- 197 S. Maity, A. A. Vannathan, T. Kella, D. Shee, P. P. Das and S. S. Mal, Electrochemical performance of activated



- carbon-supported vanadomolybdates electrodes for energy conversion, *Ceram. Int.*, 2021, **47**, 27132–27141.
- 198 M. Yang, B. G. Choi, S. C. Jung, Y.-K. Han, Y. S. Huh and S. B. Lee, Polyoxometalate-coupled Graphene via Polymeric Ionic Liquid Linker for Supercapacitors, *Adv. Funct. Mater.*, 2014, **24**, 7301–7309.
- 199 Y. Hou, D. Chai, B. Li, H. Pang, H. Ma, X. Wang and L. Tan, Polyoxometalate-Incorporated Metallacalixarene@Graphene Composite Electrodes for High-Performance Supercapacitors, *ACS Appl. Mater. Interfaces*, 2019, **11**, 20845–20853.
- 200 D. Pakulski, A. Gorczyński, W. Czepa, Z. Liu, L. Ortolani, V. Morandi, V. Patroniak, A. Ciesielski and P. Samorì, Novel Keplerate type polyoxometalate-surfactant-graphene hybrids as advanced electrode materials for supercapacitors, *Energy Storage Mater.*, 2019, **17**, 186–193.
- 201 S. Yu, M. Yang, Y. Liu and M. Liu, Recent advances in separation membranes based on porous organic molecular materials, *Mater. Chem. Front.*, 2023, **7**, 3560–3575.
- 202 S. Zeb, G. Sun, Y. Nie, H. Xu, Y. Cui and X. Jiang, Advanced developments in nonstoichiometric tungsten oxides for electrochromic applications, *Mater. Adv.*, 2021, **2**, 6839–6884.
- 203 M. Wang, Y. Yu, M. Cui, X. Cao, W. Liu, C. Wu, X. Liu, T. Zhang and Y. Huang, Development of polyoxometalate-anchored 3D hybrid hydrogel for high-performance flexible pseudo-solid-state supercapacitor, *Electrochim. Acta*, 2020, **329**, 135181.
- 204 J. Kim, Y. Kim, J. Yoo, G. Kwon, Y. Ko and K. Kang, Organic batteries for a greener rechargeable world, *Nat. Rev. Mater.*, 2023, **8**, 54–70.
- 205 Y. Zhang, L. Tao, C. Xie, D. Wang, Y. Zou, R. Chen, Y. Wang, C. Jia and S. Wang, Defect engineering on electrode materials for rechargeable batteries, *Adv. Mater.*, 2020, **32**, 1905923.
- 206 F. Cheng, J. Liang, Z. Tao and J. Chen, Functional materials for rechargeable batteries, *Adv. Mater.*, 2011, **23**, 1695–1715.
- 207 R. Raccichini, A. Varzi, S. Passerini and B. Scrosati, The role of graphene for electrochemical energy storage, *Nat. Mater.*, 2015, **14**, 271–279.
- 208 M. M. Rahman, J.-Z. Wang, M. F. Hassan, S. Chou, Z. Chen and H. K. Liu, Nanocrystalline porous  $\alpha$ -LiFeO<sub>2</sub>-C composite—an environmentally friendly cathode for the lithium-ion battery, *Energy Environ. Sci.*, 2011, **4**, 952–957.
- 209 K. Jia, J. Ma, J. Wang, Z. Liang, G. Ji, Z. Piao, R. Gao, Y. Zhu, Z. Zhuang, G. Zhou and H. M. Cheng, Long-Life Regenerated LiFePO<sub>4</sub> from Spent Cathode by Elevating the d-Band Center of Fe, *Adv. Mater.*, 2022, **35**, 2208034.
- 210 D. Liu, Z. J. Liu, X. Li, W. Xie, Q. Wang, Q. Liu, Y. Fu and D. He, Group IVA Element (Si, Ge, Sn)-Based Alloying/Dealloying Anodes as Negative Electrodes for Full-Cell Lithium-Ion Batteries, *Small*, 2017, **13**, 1702000.
- 211 M. Zheng, H. Tang, L. Li, Q. Hu, L. Zhang, H. Xue and H. Pang, Hierarchically Nanostructured Transition Metal Oxides for Lithium-Ion Batteries, *Adv. Sci.*, 2018, **5**, 1700592.
- 212 S. Liang, Y. J. Cheng, J. Zhu, Y. Xia and P. Müller-Buschbaum, A Chronicle Review of Nonsilicon (Sn, Sb, Ge)-Based Lithium/Sodium-Ion Battery Alloying Anodes, *Small Methods*, 2020, **4**, 2000218.
- 213 H. Hou, X. Qiu, W. Wei, Y. Zhang and X. Ji, Carbon Anode Materials for Advanced Sodium-Ion Batteries, *Adv. Energy Mater.*, 2017, **7**, 1602898.
- 214 H. Wang, S. Hamanaka, Y. Nishimoto, S. Irle, T. Yokoyama, H. Yoshikawa and K. Awaga, In Operando X-ray Absorption Fine Structure Studies of Polyoxometalate Molecular Cluster Batteries: Polyoxometalates as Electron Sponges, *J. Am. Chem. Soc.*, 2012, **134**, 4918–4924.
- 215 E. Ni, S. Uematsu and N. Sonoyama, Anderson type polyoxomolybdate as cathode material of lithium battery and its reaction mechanism, *J. Power Sources*, 2014, **267**, 673–681.
- 216 J.-J. Chen, M. D. Symes, S.-C. Fan, M.-S. Zheng, H. N. Miras, Q.-F. Dong and L. Cronin, High-Performance Polyoxometalate-Based Cathode Materials for Rechargeable Lithium-Ion Batteries, *Adv. Mater.*, 2015, **27**, 4649–4654.
- 217 J. Wang, L. Wang, C. Liu, Y. Wang, F. Ye, W. Yan and B. Liu, Polyoxovanadate ionic crystals with open tunnels stabilized by macrocations for lithium-ion storage, *Nano Res.*, 2023, **16**, 9267–9272.
- 218 J. Wang, Y. Liu, Q. Sha, D. Cao, H. Hu, T. Shen, L. He and Y.-F. Song, Electronic Structure Reconfiguration of Self-Supported Polyoxometalate-Based Lithium-Ion Battery Anodes for Efficient Lithium Storage, *ACS Appl. Mater. Interfaces*, 2021, **14**, 1169–1176.
- 219 J. Hu, Y. Ji, W. Chen, C. Streb and Y.-F. Song, “Wiring” redox-active polyoxometalates to carbon nanotubes using a sonication-driven periodic functionalization strategy, *Energy Environ. Sci.*, 2016, **9**, 1095–1101.
- 220 L. Huang, J. Hu, Y. Ji, C. Streb and Y.-F. Song, Pyrene-Anderson-Modified CNTs as Anode Materials for Lithium-Ion Batteries, *Chem. Eur. J.*, 2015, **21**, 18799–18804.
- 221 W. Chen, L. Huang, J. Hu, T. Li, F. Jia and Y.-F. Song, Connecting carbon nanotubes to polyoxometalate clusters for engineering high-performance anode materials, *Phys. Chem. Chem. Phys.*, 2014, **16**, 19668–19673.
- 222 K. Kume, N. Kawasaki, H. Wang, T. Yamada, H. Yoshikawa and K. Awaga, Enhanced capacitor effects in polyoxometalate/graphene nanohybrid materials: a synergetic approach to high performance energy storage, *J. Mater. Chem. A*, 2014, **2**, 3801–3807.
- 223 J. Xie, Y. Zhang, Y. Han and C. Li, High-Capacity Molecular Scale Conversion Anode Enabled by Hybridizing Cluster-Type Framework of High Loading with Amino-Functionalized Graphene, *ACS Nano*, 2016, **10**, 5304–5313.
- 224 F.-C. Shen, Y.-R. Wang, S.-L. Li, J. Liu, L.-Z. Dong, T. Wei, Y.-C. Cui, X. L. Wu, Y. Xu and Y.-Q. Lan, Self-assembly of polyoxometalate/reduced graphene oxide composites induced by ionic liquids as a high-rate cathode for batteries: “killing two birds with one stone”, *J. Mater. Chem. A*, 2018, **6**, 1743–1750.
- 225 J.-H. Liu, M.-Y. Yu, J. Yang, Y.-Y. Liu and J.-F. Ma, Polyoxometalate-based complex/graphene for high-rate lithium-ion batteries, *Microporous Mesoporous Mater.*, 2021, **310**, 110666.



- 226 H. Chao, H. Qin, M. Zhang, Y. Huang, L. Cao, H. Guo, K. Wang, X. Teng, J. Cheng, Y. Lu, H. Hu and M. Wu, Boosting the Pseudocapacitive and High Mass-Loaded Lithium/Sodium Storage through Bonding Polyoxometalate Nanoparticles on MXene Nanosheets, *Adv. Funct. Mater.*, 2021, **31**, 2007636.
- 227 H. Chao, Y. Li, Y. Lu, Y. Yao, Y. Zhu, H. Yang, K. Wang, Y. Wan, Q. Xu, L. Guan, H. Hu and M. Wu, MXene-mediated regulation of local electric field surrounding polyoxometalate nanoparticles for improved lithium storage, *Sci. China Mater.*, 2022, **65**, 2958–2966.
- 228 Y. Yue, Y. Li, Z. Bi, G. M. Veith, C. A. Bridges, B. Guo, J. Chen, D. R. Mullins, S. P. Surwade and S. M. Mahurin, A POM-organic framework anode for Li-ion battery, *J. Mater. Chem. A*, 2015, **3**, 22989–22995.
- 229 Q. Huang, T. Wei, M. Zhang, L.-Z. Dong, A. M. Zhang, S.-L. Li, W.-J. Liu, J. Liu and Y.-Q. Lan, A highly stable polyoxometalate-based metal-organic framework with  $\pi$ - $\pi$  stacking for enhancing lithium ion battery performance, *J. Mater. Chem. A*, 2017, **5**, 8477–8483.
- 230 Z. Wang, R. Bi, J. Liu, K. Wang, F. Mao, H. Wu, Y. Bu and N. Song, Polyoxometalate-based Cu/Zn-MOFs with diverse stereo dimensions as anode materials in lithium ion batteries, *Chem. Eng. J.*, 2021, **404**, 127117.
- 231 T. Wei, M. Zhang, P. Wu, Y.-J. Tang, S.-L. Li, F.-C. Shen, X.-L. Wang, X.-P. Zhou and Y.-Q. Lan, POM-based metal-organic framework/reduced graphene oxide nanocomposites with hybrid behavior of battery-supercapacitor for superior lithium storage, *Nano Energy*, 2017, **34**, 205–214.
- 232 M. Zhang, A.-M. Zhang, X.-X. Wang, Q. Huang, X. Zhu, X.-L. Wang, L.-Z. Dong, S.-L. Li and Y.-Q. Lan, Encapsulating ionic liquids into POM-based MOFs to improve their conductivity for superior lithium storage, *J. Mater. Chem. A*, 2018, **6**, 8735–8741.
- 233 L. Ni, G. Yang, Y. Liu, Z. Wu, Z. Ma, C. Shen, Z. Lv, Q. Wang, X. Gong and J. Xie, Self-assembled polyoxometalate nanodots as bidirectional cluster catalysts for polysulfide/sulfide redox conversion in lithium-sulfur batteries, *ACS Nano*, 2021, **15**, 12222–12236.
- 234 J. Lei, X.-X. Fan, T. Liu, P. Xu, Q. Hou, K. Li, R.-M. Yuan, M.-S. Zheng, Q.-F. Dong and J.-J. Chen, Single-dispersed polyoxometalate clusters embedded on multilayer graphene as a bifunctional electrocatalyst for efficient Li-S batteries, *Nat. Commun.*, 2022, **13**, 202.
- 235 K. Liang, H. Zhao, J. Li, X. Huang, S. Jia, W. Chen and Y. Ren, Engineering Crystal Growth and Surface Modification of  $\text{Na}_3\text{V}_2(\text{PO}_4)_2\text{F}_3$  Cathode for High-Energy-Density Sodium-Ion Batteries, *Small*, 2023, **19**, 2207562.
- 236 J. Liu, Z. Chen, S. Chen, B. Zhang, J. Wang, H. Wang, B. Tian, M. Chen, X. Fan and Y. Huang, “Electron/ion sponge”-like V-based polyoxometalate: toward high-performance cathode for rechargeable sodium ion batteries, *ACS Nano*, 2017, **11**, 6911–6920.
- 237 T. C. Nagaiah, D. Gupta, S. D. Adhikary, A. Kafle and D. Mandal, Tuning polyoxometalate composites with carbonaceous materials towards oxygen bifunctional activity, *J. Mater. Chem. A*, 2021, **9**, 9228–9237.

